Implications of Spike-glycoprotein processing at S1/S2 by Furin, at S2' by Furin and/or TMPRSS2 and shedding of ACE2: cell-to-cell fusion, cell entry and infectivity of SARS-CoV-2

Rachid Essalmani[1], Jaspreet Jain[2,7], Delia Susan-Resiga[1,7], Ursula Andréo[1,2,7], Alexandra Evagelidis[1], Rabeb Mouna Derbali[1], David N. Huynh[1], Frédéric Dallaire[2], Mélanie Laporte[2], Adrien Delpal[3], Priscila Sutto-Ortiz[3], Bruno Coutard[4], Claudine Mapa[5], Keith Wilcoxen[5], Etienne Decroly[3], Tram NQ Pham[2], Éric A. Cohen[2,6] & Nabil G. Seidah[1*]

[1] **Laboratory of Biochemical Neuroendocrinology Montreal Clinical Research Institute** (IRCM, affiliated to the University of Montreal) 110 Pine Ave west, Montreal, QC, H2W1R7, Canada

[2] **Laboratory of Human Retrovirology Montreal Clinical Research Institute** (IRCM, affiliated to the University of Montreal) 110 Pine Ave west, Montreal, QC, H2W1R7, Canada

[3] **AFMB, CNRS**, Université Aix-Marseille, CNRS, UMR 7257, Case 925, 163 Avenue de Luminy, 13288 Marseille Cedex 09, France, Marseille, France

[4] **Unité des Virus Émergents** (UVE: Aix-Marseille Univ - IRD 190 - **Inserm** 1207 - IHU Méditerranée Infection), Marseille, France

[5] **Boston Pharmaceuticals,** Translational Research, 55 Cambridge Parkway, Suite 400, Cambridge, MA 02142, USA

[6] **Department of Microbiology, Infectiology and Immunology**, Université de Montréal, Montréal, Québec, Canada

[7] Each of these authors contributed equally: Jaspreet Jain, Delia Susan-Resiga and Ursula Andreo

[*]Corresponding author: seidahn@ircm.qc.ca

Short title: **Furin and TMPRSS2 are the major processing enzymes of spike protein regulating SARS-CoV-2 infection**

Abstract

The Spike (S)-protein of SARS-CoV-2 binds host-cell receptor ACE2 and requires proteolytic "priming" at P**R**RA**R**$_{685}$↓ into S1 and S2 (cleavage at S1/S2), and "fusion-activation" at KPS**KR**$_{815}$↓ (cleavage at S2') for viral entry. Both cleavages occur at Furin-like motifs suggesting that proprotein convertases might promote virus entry. *In vitro* Furin cleaved peptides mimicking the S1/S2 cleavage site more efficiently than S2', whereas TMPRSS2 cleaved at both sites. In HeLa cells endogenous Furin-like enzymes cleave mainly at S1/S2 during intracellular protein trafficking, as confirmed by mutagenesis. We also mapped the S2' cleavage site by proteomics and further showed that S2'-processing by Furin, while limited, was strongly enhanced in the presence of ACE2. In contrast, the S2' KRRKR$_{815}$↓ mutant (μS2') was considerably better cleaved by Furin, whereas individual/double KR815AA mutants are retained in the endoplasmic reticulum (ER). Pharmacological inhibitors of convertases (Boston Pharmaceuticals - BOS-inhibitors) effectively blocked endogenous S-protein processing in HeLa cells. However, under co-expression the S-protein was prematurely cleaved by TMPRSS2 into ER-retained, non-O-glycosylated S2 and S2' products. Quantitative analysis of cell-to-cell fusion and Spike processing using Hela cells revealed the key importance of the Furin sites for syncytia formation and unveiled the enhanced fusogenic potential of the α- and δ-variants of the S-protein of SARS-CoV-2. Our fusion assay indicated that TMPRSS2 enhances S2' formation, especially in the absence of Furin cleavage, as well as ACE2 shedding. Furthermore, we provide evidence using pseudoparticles that while entry by a "pH-dependent" endocytosis pathway in HEK293 cells did not require Furin processing at S1/S2, a "pH-independent" viral entry in lung-derived Calu-3 cells was sensitive to inhibitors of Furin and TMPRSS2. Consistently, in Calu-3 cells BOS-inhibitors or Camostat potently reduce infectious viral titer and cytopathic effects and this outcome was enhanced when both compounds were combined. Overall, our results show that Furin and TMPRSS2 play synergistic roles in generating fusion-competent S-protein, and promote viral entry, supporting the combination of Furin and TMPRSS2 inhibitors as potent antivirals against SARS-CoV-2.

Author Summary

SARS-CoV-2 is the etiological agent of the COVID-19 pandemic that spread around the world in 2020 resulting in ~4 million deaths. The surface spike protein (S) of the virus directs infection of the lungs and other tissues by binding the angiotensin-converting enzyme 2 (ACE2) receptor. For effective infection, the S-protein needs to be cleaved at two sites: S1/S2 and S2'. Cleavage at S1/S2 induces a conformational change in the spike protein favouring the recognition of the ACE2 receptor. The S2' cleavage is critical for the exposure of the fusion domain of the S-protein needed for virus entry into host cells. Several new S-variants contain mutations in the S1/S2 cleavage site possibly enhancing the S-protein processing, especially for the δ-variant, which may explain the higher transmissibility of this virus worldwide. Our study contributes to a better understanding of the dynamics of interaction between Furin and TMPRSS2 in SARS-CoV-2 entry and suggest that the combination of a non-toxic Furin inhibitor with that of TMPRSS2 could significantly reduce viral entry in lung cells, as evidenced by our results showing an average synergistic ~95% reduction of viral infection. This represents a powerful novel antiviral approach to reduce viral spread in individuals infected by SARS-CoV-2 or future related coronaviruses.

Introduction

Epidemics date from prehistoric times but are exacerbated by overcrowding and human impact on the ecosystem [1]. The RNA coronaviruses (CoV) are zoonotic pathogens that spread in the human population, causing respiratory, enteric, renal and neurological diseases [2]. Electron microscopy of CoV revealed that the lipid envelope of each virion is surrounded by a "crown"-like structure [3], composed of multiple copies of a viral surface glycoprotein known as "spike" (S), which is essential for receptor binding and virus entry. Severe Acute Respiratory Syndrome coronavirus (SARS-CoV-1) and Middle East Respiratory Syndrome coronavirus (MERS-CoV) are infectious pathogenic viruses that appeared in humans at the beginning of

75 the 21st century [2, 4]. At the end of 2019, a third CoV, namely SARS-CoV-2, emerged causing widespread
76 pandemic respiratory and vascular illnesses [5], coined COVID-19 [6].

77 Like envelope glycoproteins of many infectious viruses [7-9] the secretory type-I membrane-bound S of
78 SARS-CoV-2 is synthesized as a precursor (proS) that undergoes cleavages by host cell proteases at specific
79 sites to enhance viral entry. During infection, the trimetric proS (monomer, 1,272 residues) is first processed
80 at an S1/S2 cleavage site by host cell proteases (Fig. 1A). Unlike SARS-CoV-1, the S-protein of SARS-
81 CoV-2 exhibits an insertion of four critical amino acids (PRRA) at the S1/S2 junction [10-12], forming a
82 P**R**RA**R**$_{685}$↓ Furin-like cleavage site (FCS). Such "priming" step divides the protein into two subunits S1
83 and S2 held together by non-covalent interactions. Following S-protein priming, the N-terminal S1-
84 ectodomain undergoes a conformational change that exposes its receptor-binding-domain (RBD) [13],
85 which recognizes the ACE2 entry receptor [11]. The trimeric C-terminal membrane-anchored S2-subunit
86 is involved in host-cell fusion and viral entry [11]. The S2-subunit contains an additional "fusion-
87 activation" proteolytic site (S2') whose precise location remains poorly defined, followed by an α-helical
88 fusion peptide (FP) and two heptad-repeat domains preceding the transmembrane domain (TM) and
89 cytosolic tail (CT) (Fig. 1A). It is thought that cleavage at S2' triggers large-scale rearrangements, including
90 a refolding step that is associated with the separation of S1- and S2-subunits and exposure of a
91 hydrophobic α-helix C-terminal to S2', favoring fusion of viral and host cell membranes leading to virus
92 entry [14]. Fusion with host cells can occur either at the cell surface (pH-independent) or following
93 endocytosis of the virus (pH-dependent) [15]. However, the cognate host-cell proteases responsible for
94 the S1/S2 and S2' cleavages vary between each coronavirus and cell-type infected [11, 12, 16-19].

95 The proprotein convertases (PCs; genes *PCSKs*) constitute a family of nine secretory serine proteases
96 that regulate various processes in both health and disease states [20]. Through proteolysis, PCs are
97 responsible for the activation and/or inactivation of many secretory precursor proteins, including
98 virus/pathogen surface glycoproteins [9, 20]. Seven PCs, including the widely expressed Furin, PC5A,
99 PACE4 and PC7 cleave secretory substrates at specific single/paired basic amino acids (aa) within the

100 motif (K/R)-X_n-(K/R)↓, where Xn= 0, 2, 4 or 6 spacer X residues [20]. Because of their critical
101 functions, PCs, especially the ubiquitously expressed Furin [21], are implicated in many viral
102 infections *via* specific cleavages of envelope glycoproteins, a condition that allows not only the fusion
103 of the viral lipid envelope with host cell membranes [9, 20], but also cell-to-cell fusion (syncytia) for
104 certain viral infections leading to important cytopathogenic effects [22, 23].

105 As the S1/S2 cleavage is thought to play a critical role for cellular receptor recognition and virus
106 entry, the efficacy and extent of this activation step by host proteases might be a key determinant
107 regulating cellular tropism, viral pathogenesis, and human-to-human transmission. In contrast to
108 SARS-CoV-1, the proS of SARS-CoV-2 contains a structurally exposed P**R**RA**R**$_{685}$↓S**V** motif [10, 11]
109 (Fig. 1A), which corresponds to a canonical FCS [9, 10, 20]. This Furin-like motif is presumably
110 cleaved during *de novo* virus egress [23] for S-protein priming and may provide a key role for the
111 efficient spread of SARS-CoV-2 to various human tissues compared to the more limited tropism of
112 other lineage B β-coronaviruses [10, 24]. Furthermore, based on the predicted S2' sequence of SARS-
113 CoV-2, we proposed [10] that Furin-like enzymes could also cleave the latter site at KPS**KR**$_{815}$↓S**F**
114 (Fig. 1A). Indeed, various reports have since supported the implication of Furin in the S1/S2 priming
115 of the S-protein in human cell culture models [12, 25, 26] and *in vivo* in mice, hamsters and ferrets [27,
116 28]. In addition, it was also suggested that the cell surface type-II transmembrane serine protease 2
117 (TMPRSS2) enhances fusion by cleavage at S2', but that S1/S2 cleavage is mostly Furin-dependent
118 [18]. The ability of the Arg/Lys-specific TMPRSS2 [29, 30] to directly cleave at S2' was suggested
119 based on the viral entry blockade by the TMPRSS2 inhibitor Camostat [31-33], and through silencing
120 of TMPRSS2 expression using a morpholino oligomer [18]. Thus, it is likely that one or more proteases
121 can regulate SARS-CoV-2 entry into human airway epithelial cells [18, 24]. Furthermore, since the
122 tissue-expression of TMPRSS2 is restricted to a limited set of cell types compared to that of the
123 ubiquitously expressed Furin, the activity of the latter may widen viral tropism [34].

124 The major goals of the present study were to precisely define the respective roles of Furin and TMPRSS2
125 in the fusion activation and infectivity of SARS-CoV-2, and to test the consequences of their inhibition.
126 The convertases Furin and PC5A were shown to induce effective priming of proS at S1/S2 generating
127 membrane anchored S2 and a soluble S1 subunit, and a less efficient cleavage at S2', even in the presence
128 of ACE2. Unexpectedly, when TMPRSS2 was co-expressed with the S-protein, cleavage occurred early in
129 the ER, generating non-O-glycosylated products S2a and S2b and a secreted S1' by a non-conventional
130 pathway [35]. In contrast, co-cultures of HeLa cells expressing S or its Furin-resistant S1/S2 mutant
131 $ARAA_{685}$ (μS1/S2) with cells expressing ACE2 and TRMPSS2, revealed that TMPRSS2 on the cell surface
132 of acceptor cells can generate an S2' product, especially in absence of Furin cleavage. TMPRSS2 also
133 cleaved ACE2 into a soluble form (sACE2) [36], which possibly binds the secreted S1 subunit.
134 We present for the first time the effectiveness of three non-toxic, cell-permeable small molecule Furin-
135 like inhibitors (Boston Pharmaceuticals, BOS-inhibitors) that resulted in sustained intracellular inhibition
136 of proS processing at S1/S2 and S2' by endogenous cellular Furin-like proteases. Cell-to-cell fusion assays
137 using modified HeLa cells emphasized the functional importance of the S1/S2 and S2' sites in the fusion
138 process. This fusion assay also enabled the assessment of the potentiating effects of some worldwide-
139 spreading S-protein variants of SARS-CoV-2 [37]. While BOS-inhibitors did not affect HEK293/ACE2
140 cell entry of S-pseudovirions that occurs by "pH-dependent" endocytosis, they blocked cell-to-cell fusion
141 in HeLa cells and impaired the infection of the lung-derived epithelial cell line Calu-3 by S-pseudovirions
142 or by replication-competent SARS-CoV-2, an antiviral effect potentiated by Camostat. The data support
143 Furin-inhibitors in combination with TMRPSS2-blocking agents as potent antivirals against acute SARS-
144 CoV-2 infection.
145
146
147
148

149 # Results

150

151 ***In vitro* cleavage of peptides mimicking S1/S2 and S2' sites.** The susceptibility of S-glycoprotein of
152 SARS-CoV-2 to Furin-cleavage was first assessed *in vitro*. Incubation of quenched fluorogenic peptides
153 encompassing S1/S2 and S2' sites (Supporting Information SI-Table 1), demonstrated that the S1/S2 site
154 of SARS-CoV-2 was efficiently cleaved by 2 nM Furin at pH 7.5 (Fig. 1B) and less so at pH 6 (*not shown*),
155 whereas the S1/S2 site of SARS-CoV-1, which lacks an FCS, was barely cleaved (Fig. 1B). Furin less
156 efficiently cleaved the SARS-CoV-2-mimic peptide at S2', requiring 50-fold higher enzyme concentrations
157 (100 nM) to detect cleavage (inset Fig. 1B). The high specificity of the SARS-CoV-2 for processing at
158 Furin-like motifs was next confirmed by demonstrating that substitutions of basic residues at the S1/S2
159 cleavage site (RRA**A**$_{685}$↓S, **A**RA**A**$_{685}$↓S, **A**RAR$_{685}$↓S) dramatically impaired S1/S2 cleavage (Fig. 1B). In
160 addition, the δ-variant P681R (RRRAR$_{685}$), which was similarly cleaved by Furin at 2 nM, showed a modest
161 increased cleavage at 0.2 nM of Furin (~130%), whereas the α-variant P681H (HRRAR$_{685}$) was ~50% less
162 cleaved *in vitro* by Furin than the wild type (WT) S1/S2. We also showed that an S2' mutant enriched in
163 basic amino acids (RRKR$_{815}$) was ~56-fold better cleaved by 2 nM Furin (Fig. 1B). Altogether these data
164 demonstrated that Furin best cleaves at S1/S2 and less efficiently at S2'. TMPRSS2 was also proposed to
165 participate in SARS-CoV-2 entry in some cells [18, 24]. Accordingly, we tested whether TMPRSS2 can
166 cleave peptides encompassing S1/S2 or S2' cleavage sites *in vitro*. The data showed that while TMPRSS2
167 did not efficiently cleave a peptide mimicking SARS-CoV-1 at S1/S2, at 50 nM it was able to process
168 SARS-CoV-2 at S1/S2 and ~2-fold less at S2' (Fig. 1C). Furthermore, the S1/S2 Ala-mutants RRAA,
169 ARAA and ARAR were all cleaved by TMPRSS2 (Fig. 1C). These data emphasize the critical importance
170 of the P1 and P4 Arg for Furin-mediated cleavage and suggest that the likely motif recognized by
171 TMPRSS2 is either Arg↓Ala or Arg↓Ser with a preference for Ala at P2 over Arg (Fig. 1C). As expected,

172 the S2' mutant RRKR$_{815}$↓S is strikingly better cleaved by Furin (Fig. 1B) but similarly processed by
173 TMPRSS2 as the WT peptide (Fig. 1C).
174
175 **ProS processing by Furin-like convertases and TMPRSS2.** To further decipher the cellular implication
176 of Furin-like enzymes, we expressed the S-protein in several cell lines and selected human HeLa cells as a
177 model since they showed efficient endogenous processing of the S-protein. Using qPCR we demonstrated
178 that our HeLa cells endogenously express Furin but not TMPRSS2 or ACE2 mRNAs (*not shown*), as also
179 reported earlier [38]. Thus, we co-transfected HeLa cells with a plasmid containing a codon-optimized
180 cDNA coding for V5-tagged proS (Fig. 1A) and cDNAs encoding the four plausible secretory proprotein
181 convertases PC5A, Furin, PC7 and PACE4 that cleave precursors at the *trans* Golgi network (TGN), cell
182 surface and/or recycling endosomes [20, 39]. Cell lysates were analyzed by Western blot (WB) after SDS-
183 PAGE separation and probed with a V5-mAb [40]. We observed that an endogenous protease(s) expressed
184 in HeLa cells can process proS, likely at S1/S2, into a ~100 kDa S2-like product (Fig. 2A). Furthermore,
185 only overexpression of Furin and PC5A enhanced the production of the less abundant ~75 kDa S2'-like
186 fragment (Fig. 2A). The remaining ~200 kDa proS$_{im}$ corresponds to an immature precursor form that has
187 not exited the ER, as attested by its sensitivity to endoglycosidase-F and endoglycosidase-H (SI-Fig. 1A),
188 and insensitivity to Furin-like convertases, which are only active in the TGN and/or cell surface/endosomes
189 [20, 39].
190 The double Ala-mutant [R682A + R685A] (denoted μS1/S2) of the S1/S2 site **R**RA**R**$_{685}$↓S eliminated
191 the P4 and P1 Arg critical for recognition by Furin-like enzymes [20], and completely abrogated processing
192 of proS at S1/S2 and putative S2' by endogenous enzymes or by overexpressed Furin (Fig. 2B; SI-Fig. 1A).
193 These data support a role for Furin in the S1/S2 cleavage. The loss of Furin-like cleavage at S1/S2 resulted
194 in the accumulation of a higher molecular sized proS$_{m}$ (~230 kDa), which represents a mature form of this
195 precursor that exited the ER and became endoglycosidase-H-resistant but remained endoglycosidase-F-
196 sensitive (SI-Fig. 1A) [20, 40]. The cell-permeable PC-inhibitor decanoyl-RVKR-cmk (RVKR) [41]

197 effectively prevented the endogenous formation of S2, but not the D6R inhibitor [42] that mostly inhibits
198 Furin at the cell surface but does not significantly affect Furin processing in the TGN [40] (Iris Lindberg,
199 *personal communication*) (SI-Fig. 1B). This suggests that in HeLa cells proS cleavage by endogenous
200 Furin into S1 and S2 primarily occurs during intracellular trafficking and not at the cell surface.

201 In HeLa cells expressing S-protein we performed a knockdown of Furin mRNA (SI-Fig. 1C) using
202 an optimized mixture of 4-siRNAs (siFur) compared to a scrambled control (siCTL). Under these
203 conditions, reduction of Furin protein levels was associated with >60% lower S2 levels (SI-Fig. 1C),
204 clearly emphasizing the key role of endogenous Furin in the S1/S2 processing.

205 To better define the Arg-residues critical for processing at S1/S2, we expressed in HeLa cells proS
206 constructs carrying single residue mutations: R682A, R685A and S686A in the absence or presence of
207 overexpressed Furin (SI-Fig. 1D). The results confirmed the critical importance of P1-Arg_{685} or P4-Arg_{682}
208 for the generation of S2 by endogenous Furin. In contrast to μS1/S2 (Fig. 2B), these single mutants were
209 partially cleaved by overexpressed Furin (SI-Fig. 1D). This reflects the multi-basic nature of the S1/S2
210 recognition sequence **R**RA**R**$_{685}$↓S, whereby **RR**AA$_{685}$ and A**R**A**R**$_{685}$ are cleavable, but not ARAA$_{685}$
211 (μS1/S2), suggesting the importance of the P3 Arg_{683} [43]. The S686A mutant was based on the
212 prediction that Ser_{686} could be O-glycosylated [44], which may hamper processing at S1/S2 [45]. However,
213 like the WT, the S686A mutant was efficiently processed by Furin into S2 and S2' (SI-Fig. 1D).

214 We next proceeded to identify the exact S2' site cleaved by Furin using site-directed mutagenesis.
215 Compared to a control R995A mutant, all the K814A, R815A and KR815AA and S816E mutants of
216 the P1, P2 and P1' residues [20] of the predicted S2' site (KPSKR$_{815}$↓SF) resulted in an ER-retained
217 $proS_{im}$ protein (SI-Figs. 2A, B). Therefore, we resorted to mass spectrometry analysis of proteins
218 migrating at the S2' position to identify this site. The peptides generated by a Lys-specific protease
219 (K_{814}↓) allowed the discrimination between SFIEDLLFNK_{825} that would be generated if cleavage by
220 Furin at S2' occurred at Arg_{815}, and R_{815}SFIEDLLFNK_{825} that would be derived from N-terminally
221 extended proteins, e.g., S2. The proteomic data revealed a >50-fold higher ratio of SFIEDLLFNK_{825}

222 to RSFIEDLLFNK$_{825}$ for the S2' product (and not S2) (Fig. 2C). This demonstrates that the N-terminus
223 of S2' starts at Ser$_{816}$ and that Furin cleavage at S2' occurs after Arg$_{815}$↓ in the sequence
224 KPSK**R**$_{815}$↓SFIEDLLFNKVT (Fig. 1A). To further demonstrate the role of Furin in S2' cleavage we
225 generated a Furin-optimized S2' site (called μS2'; *see* Fig. 1B) with a polybasic sequence
226 KRRKR$_{815}$↓SF and evaluated its cleavage by endogenous enzymes in HeLa cells and by overexpressed
227 Furin. This optimized S2' mutant folds well and can be extensively processed endogenously and
228 especially by overexpressed Furin, generating much higher levels of S2' migrating on SDS/PAGE at
229 the expected molecular size compared to WT (Fig. 2D). Altogether these data demonstrate the S2'
230 cleavage occurs at Arg$_{815}$↓ and can be efficiently processed by Furin.
231 We then examined the processing of proS when co-expressed with TMPRSS2 in HeLa cells (Fig. 2B).
232 Unexpectedly, under these conditions, TMPRSS2 did not yield the *bona fide* proS products S2 or S2'
233 generated by Furin, but rather, two minor seemingly smaller-sized C-terminal V5-tagged products, herein
234 called S2a (~85 kDa) and S2b (~70 kDa). These fragments were observed with both wild-type (WT)-S and
235 its μS1/S2 mutant (Fig. 2B). Note that the ~100 kDa S2 product generated by endogenous Furin-like
236 enzymes was absent when TMPRSS2 was co-expressed with WT proS (Fig. 2B), suggesting that
237 TMPRSS2 generates S2a and S2b before proS encounters endogenous Furin, which is autoactivated in the
238 TGN [39]. Indeed, like proS$_{im}$ (SI-Fig. 1A), both S2a and S2b were endoglycosidase-H-sensitive (SI-Fig.
239 3A), indicating that they were generated in the ER and no longer exited this compartment. Thus, exogenous
240 TMPRSS2 co-expressed with proS would effectively process/inactivate S2 in the ER, preventing its exit to
241 reach the cell surface. Altogether, our data show that overexpression of TMPRSS2 in the same cells as S-
242 protein would result in its premature processing and inactivation.
243
244 **Processing at S2' is enhanced in the presence of ACE2.** The implication of ACE2 in the processing of
245 proS in HeLa cells was next assessed by co-expression of proS with Furin or TMPRSS2 in the absence or
246 presence of ACE2 (Fig. 3A). While not significantly affecting the relative S1/S2 cleavage, the expression

247 of ACE2 strongly enhanced the generation of S2' by endogenous and overexpressed Furin (without a
248 significant change in S2 levels), and S2b by TMPRSS2 (Fig. 3A), likely reflecting a change in the proS
249 conformation upon ACE2-binding [13, 46], which could start as early as the ER in the secretory pathway.
250 Endogenous Furin processing of proS to generate S2 was accompanied by the secretion of the N-terminal
251 ~130 kDa S1 subunit (aa 14-685; Fig. 1A; SI-Fig. 3B). Amazingly, in the presence of ACE2, the mutant
252 μS1/S2 that is resistant to endogenous Furin cleavage at S1/S2 (Fig. 2B), can be partially cleaved directly
253 into S2' by overexpressed Furin (Fig. 3B). We conclude that binding of S-protein to ACE2 enhances Furin
254 processing at S2', likely facilitating exposure of the S2' site [47], and increases the secretion of S1.

255 Interestingly, single (SI-Fig. 1D) or double (μS1/S2; SI-Fig. 2A) Arg mutations in the S1/S2 site did not
256 affect the ability of TMPRSS2 to generate S2a and S2b, suggesting that these cleavages (**i**) occur at other
257 sites in proS, or (**ii**) that the remaining single Arg in all the studied S1/S2-mutants while preventing Furin-
258 cleavage could still allow TMPRSS2 to cleave proS, as suggested from *in vitro* data on the ARAA-peptide
259 (Fig. 1C). To discriminate between these two possibilities, we generated a poly-A mutant μAS1/S2
260 ($AAAA_{685}$) where all the Arg in S1/S2 were mutated to Ala. The data showed that in presence of ACE2,
261 neither endogenous Furin or overexpressed TMPRSS2 could cleave the co-expressed μAS1/S2 into S2 or
262 S2a, respectively, but that TMPRSS2 still cleaved μAS1/S2 into S2b (SI-Fig. 3B).

263 To prove that the protease activity of TMPRSS2 is critical, we co-expressed an active site Ser* mutant of
264 TMPRSS2 (S441A; μTMPR; *see later*) with ACE2 and S-protein, which eliminated the generation of S2a
265 and S2b and the shedding of ACE2 into the medium (SI-Fig. 3B). In addition, this inactive μTMPRSS2
266 seemingly stabilized the S2 generated from WT-S and enhanced the processing of proS into S2', likely by
267 endogenous Furin, especially for the μS1/S2 and μAS1/S2 mutants (SI-Fig. 3B). These data emphasized
268 the implication of Furin in the generation of S2' when TMPRSS2 protease activity was absent. Befittingly,
269 S1 generated by Furin cleavage at S1/S2 was secreted from WT-S, whereas TMPRSS2 co-expression with
270 WT-S or μS1/S2 resulted in the secretion of S1' (SI-Fig. 3B).

271 To better gauge the effect of TMPRSS2 on the production of the N-terminal segment of proS following
272 formation of S2a and/or S2b we generated a doubly tagged construct consisting of [signal peptide of
273 PCSK9]-HA-[Q_{14}CVNLT….]-V5 [48], where Gln_{14} is the N-terminus of proS after its own signal peptide
274 cleavage. In the partial (μS1/S2) or complete absence (μAS1/S2) of S1/S2 cleavage the generation of S2'
275 likely results in the formation of a long $S1_L$ (aa 14-815; Fig. 1A). Indeed, $S1_L$ (~175 kDa) was detected in
276 the media of μS1/S2 and more so of μAS1/S2 in the presence of active TMPRSS2, but not of its inactive
277 Ser* mutant (μTMPRSS2; SI-Fig. 3B).
278 Expression of the above doubly tagged WT-S-protein construct in stable HeLa-ACE2 cells revealed the
279 secretion of an N-glycosylated (endoH-resistant but endoF-sensitive) HA-tagged N-terminal subunit S1
280 (~130 kDa) (Fig. 4A). In contrast, when TMPRSS2 was also expressed we observed the secretion of an
281 endoH and endo F sensitive S1' (~110 kDa) and a ~52 kDa product S1'' (Fig. 4A). In conclusion,
282 overexpression of TMPRSS2 with the WT-S-protein generates the ER-retained S2a and S2b and a secreted
283 S1', all of which are endoH sensitive.
284
285 **S2a and S2b are ER-retained non-O-glycosylated forms of S2 and S2', respectively.** Because
286 processing of proS by co-expressed TMPRSS2 likely occurs in the ER, we hypothesized that the S2a and
287 S2b products may be blocked in this compartment and hence may lack O-glycosylation, as this post-
288 translational modification occurs in the *cis/medial* Golgi [49]. Accordingly, we compared the processing
289 of proS by Furin and TMPRSS2 in CHO-ldlD cells, which are defective in UDP-Gal/UDP-GalNAc 4-
290 epimerase [50] and therefore cannot O-glycosylate proteins, to that in their parental CHO-K1 cells (Figs.
291 4B, C). The data showed that like in HeLa-ACE2 cells, proS was cleaved by endogenous Furin-like
292 enzymes in CHO-K1-ACE2 cells into S2-V5, S2'-V5 and secreted HA-S1. Also, TMPRSSS2 generated
293 S2a and S2b, resulting in the secretion of S1' (~100 kDa) and a smaller S1'' (~58 kDa) (Fig. 4B). In
294 contrast, in CHO-ldlD cells the similar apparent molecular weights of the products generated by

295 endogenous enzymes and TMPRSS2 suggest that Furin and TMPRSS2 cleave the S-protein at the same
296 sites.

297 The above data suggested that S2a and S2b lack O-glycosylation, and hence are likely ER-retained S2-
298 like and S2'-like products, respectively. Their identity was finally confirmed by proteomic analysis of the
299 S2a and S2b products (SI-Fig. 4). Analysis of S2a was performed using chymotrypsin digestion of various
300 proteins on the silver-stained SDS-PAGE gel (slices 1-9; SI-Fig. 4; left panel), which could generate the
301 proS derived peptides QTQTNSPRRA**R**SVASQSIIAY$_{695}$ (un-cleaved proS) or SVASQSIIAY$_{695}$ (cleaved
302 at Arg$_{685}$↓). The data showed that only the peptide SVASQSIIAY$_{695}$ was detected in proteins migrating at
303 the position of S2a (slices 5-7; SI-Fig. 4; left panel), confirming that S2a was generated by TMPRSS2
304 following cleavage at Arg$_{685}$↓, which is identical to that generated by Furin *via* cleavage at S2. For S2b, the
305 same Lys-C protease digestion used for the identification of the S2' site generated by Furin (Fig. 2C),
306 revealed that in slices 13-15 (corresponding to the migration position of S2b) the peptide SFIEDLLFNK$_{824}$
307 was at least 25-fold more abundant than its Arg-extended form RSFIEDLLFNK$_{824}$ (SI-Fig. 4; right panel).
308 This also confirms that overexpressed TMPRSS2 cleaves the S-protein at the sequence
309 KPSK**R**$_{815}$↓SFIEDLLFNK to generate S2b, as did Furin for S2'. In summary, our data support the
310 identification of S2a and S2b as ER-retained non-O-glycosylated S2 and S2', respectively.

311 To verify that S2a and S2b are products of TMPRSS2 activity, we incubated stable HeLa-ACE2 cells
312 with 120 μM Camostat, known to inhibit TMPRSS2 [31]. The data showed that Camostat prevented the
313 formation of both S2a and S2b with increasing concentrations of TMPRSS2, and gradually allowed the
314 resumption of the Furin-like cleavage at S1/S2 generating a higher molecular sized O-glycosylated S2 (SI-
315 Fig. 5A). As evidenced by the loss of the mature TMPRSS2$_m$ ~25 kDa form in the media (SI-Fig. 5A), we
316 also surmise that this cell-permeable inhibitor can reach the ER and block the autocatalytic activation of
317 TMPRSS2 at RQS**R**$_{255}$↓ [29]. In agreement, in the presence of ACE2, the mutant S441A of the active site
318 Ser* of TMPRSS2 (μTMPR) was no longer able to process proS into S2a and S2b (SI-Fig. 3B). Altogether
319 these data indicate that overexpressed TMPRSS2 is autoactivated early in the ER where it cleaves proS at

320 S1/S2 and S2', generating non-O-glycosylated products that differ in molecular weight from the ones
321 produced by Furin in the TGN/cell surface. Caution should therefore be exercised when defining processing
322 fragment of S under conditions of TMPRSS2 overexpression.

323 We next sought to explore other functions that TMPRSS2 may exert to explain its reported enhancement
324 of viral entry [17, 18, 24]. Hence, we expressed increasing amounts of TMPRSS2 in HeLa-ACE2 cells and
325 followed processing and/or levels of the S1-subunit in the media by WB-analysis using an anti-S1 antibody.
326 We showed that in a dose-dependent manner TMPRSS2 cleaved proS in the ER at S1/S2 generating a non-
327 O-glycosylated endoH sensitive (Fig. 4A) S1-like product (S1'; ~115 kDa) that was secreted into the
328 medium (SI-Fig. 5A).

329 The coat protein complex II (COP-II) catalyzes transport vesicle formation from the ER and segregates
330 export secretory cargo from ER-resident proteins *via* the formation of membrane vesicles translocating
331 cargo proteins towards the *cis* Golgi [51]. Accordingly, we assessed the level of secreted S1' upon
332 expression of a dominant negative Sar1p (H79G) mutant that would disrupt the COP-II complex [52, 53].
333 This resulted in a significant decrease in the secretion of the TMPRSS2-generated S1' (SI-Fig. 5B),
334 suggesting that in HeLa cells secretion of S1' from the ER (as it remains endoH sensitive) primarily occurs
335 *via* a COP-II-dependent unconventional pathway that bypasses the Golgi stacks [54], an unusual trafficking
336 pathway used by some coronaviruses [55].

337

338 **TMPRSS2 can shed ACE2.**

339 It was previously reported that TMPRSS2 sheds ACE2 into a soluble form (sACE2) [36], and the latter
340 activity was associated with enhanced kinetics of cell-to-cell fusion (syncytia) and SARS-CoV-1 uptake
341 [33]. In agreement, overexpression of TMPRSS2 in HeLa-ACE2 cells enhanced the shedding of ACE2,
342 and the generation of sACE2 and in large part S1' was inhibited by 120 μM Camostat (SI-Fig. 5A). Note
343 that the small background shedding of ACE2 was not sensitive to Camostat, suggesting that another
344 endogenous protease, possibly ADAM17 [36], might be implicated in ACE2 shedding, as also observed in

345 CHO-K1 cells (Fig. 4B). While in agreement with other reports on ACE2 shedding by TMPRSS2 [36], our
346 data further showed that such cleavage/shedding can occur as early as in the ER.
347
348 **Furin-inhibitors block S1/S2 and S2' cleavages without affecting TMPRSS2 processing.** We next
349 evaluated three novel non-toxic, cell-permeable Furin-inhibitors developed by Boston Pharmaceuticals
350 available as oral (BOS-981, BOS-318) or inhalable (BOS-857) formulations (chemical motif and a
351 representative structure of BOS-318 are shown in Figs. 5A, B). Accordingly, we first tested *in vitro*
352 the efficacy and selectivity of these inhibitors on purified soluble forms of Furin, PC5A, PACE4 and
353 PC7. The enzymatic activity was determined using a quenched fluorogenic substrate FAM-
354 Q**R**V**RR**AVGIDK-TAMRA, and compared to those obtained with the known PC-inhibitor RVKR-
355 cmk [40]. The data showed that all three inhibitors effectively blocked the processing of the above
356 dibasic substrate by all convertases with an IC_{50} of ~7-9 nM compared to ~9-10 nM for RVKR-cmk
357 (Fig. 5C). The Furin S1/S2 cleavage was also validated *in vitro* using a 12-residue quenched
358 fluorogenic substrate DABSYL/Glu-TNSP**RR**A**R**↓SVAS-EDANS. The inhibition deduced after hill-
359 plot curve fitting (Fig. 5D) gave an estimated IC_{50} of 4 ± 0.7 nM (BOS-981), 32 ± 4 nM (BOS-857)
360 and 35 ± 5 nM (BOS-318).
361 The inhibition of PC-activities by BOS-compounds was next assessed intracellularly using a cell-
362 based Golgi imaging assay of U2OS cells (*see methods*). The data demonstrated that BOS-compounds
363 inhibited endogenous Furin-like processing of a dibasic BMP10-mimic [40] with an IC_{50} of ~8 nM
364 *versus* 5 nM for RVKR-cmk (Fig. 5C). The above enzymatic assays showed that all 3 inhibitors can
365 inhibit Furin, but may also inhibit other members of the PC-family such as PC5A, PACE4 and PC7
366 [20].
367 The effect of BOS-inhibitors was then evaluated on the processing of proS in HeLa cells stably
368 expressing ACE2 (HeLa-ACE2; Fig. 5E). In agreement with the *in vitro* data (Fig. 5D), BOS-inhibitors
369 blocked the S1/S2 and S2' processing by endogenous Furin-like enzymes, with all three compounds

370 showing almost complete inhibition at 300 nM (Fig. 5E), comparable to that obtained with a control
371 50 μM decanoyl-RVKR-cmk. In contrast, in HeLa cells none of the BOS-inhibitors affected the
372 generation of S2a and S2b by TMPRSS2 (SI-Fig. 6), attesting to their specificity for Furin-like
373 enzymes.
374
375 **Effect of BOS-981 on S-protein trafficking and syncytia formation.** We next performed
376 immunocytochemical analyses of HeLa cells co-expressing the WT-S-protein or its μS1/S2 mutant with
377 ACE2 in the absence or presence of 1 μM BOS-981 under non-permeabilized (NP; S2 and ACE2
378 antibodies) and permeabilized (P; V5 and ACE2 antibodies) conditions (SI-Fig. 7). In the absence of BOS-
379 981, the S-protein and ACE2 co-localized abundantly at the cell surface (SI-Fig. 7A-a). HeLa cells
380 expressing both S-protein and ACE2 formed many syncytia, associated with reduced cell surface
381 expression of the S-protein, and an even greater reduction of ACE2 (SI-Fig. 7A-b). Cells expressing both
382 μS1/S2 and ACE2 showed an accumulation of both proS and ACE2 inside the cells and at the cell surface
383 (SI-Fig. 7A-c). However, they barely induced the formation of syncytia, and when they did, the cell surface
384 expression of S-protein and to a lesser extent ACE2 was decreased (SI-Fig. 7A-d). In the presence of 1 μM
385 BOS-981, S-expressing HeLa cells (SI-Figs. 7B-a,b) phenocopied those expressing μS1/S2 (SI Figs. 7B-
386 c,d).
387 Having established that S-protein and ACE2 co-localize at the cell surface and can induce syncytia
388 formation if the S-protein was processed at S1/S2 by Furin, we next analyzed further the impact of Furin-
389 cleavage at S1/S2 on the ability of S-protein to induce cell-to-cell fusion. Thus, we developed a
390 luminescence-based assay using HeLa TZM-bl reporter cells stably transfected with an HIV-1-based vector
391 expressing luciferase under the control of the HIV-1 long terminal repeat (LTR), which can be activated by
392 HIV Tat protein. These cells endogenously express the HIV receptor CD4 and its co-receptors CCR5 and
393 CXCR4 [56]. We postulated that cell-to-cell fusion of donor WT HeLa cells (expressing Tat and the
394 fusogenic S-protein) with acceptor TZM-bl cells expressing ACE2 would result in the transactivation of

395 the luciferase expression mediated by Tat and hence in accrued luciferase activity (Fig. 6A). Indeed, as a
396 proof-of-principle, when donor cells expressing HIV gp160 and Tat fused with acceptor cells, luciferase
397 activity increased compared to that observed in TZM-bl control cells co-cultured with donor Hela cells
398 expressing only Tat (SI-Fig. 8C). The expression of S-protein in HeLa cells did not induce fusion with
399 TZM-bl control cells (SI-Figs. 8A, C). However, ACE2 expression in TZM-bl allowed fusion with HeLa-
400 expressing S-protein in a dose-dependent manner (SI-Fig. 8B). The linearity of our assay (correlation
401 coefficient of 0.87) validated the use of luminescence as an indicator of cell-to-cell fusion (SI-Fig. 8B).
402 Conversely, expression of μS1/S2 in donor cells did not enhance fusion with TZM-bl expressing ACE2
403 and >60% fusion-inhibition was observed upon incubation of cells with 300 nM of BOS-inhibitors or 10
404 μM of the PC-inhibitor dec-RVKR-cmk (RVKR; Fig. 6B), indicating that Furin-cleavage promotes ACE2-
405 dependent cell-to-cell fusion.
406
407 **Respective roles of Furin, TMPRSS2 and ACE2 in cell-to-cell fusion.** To assess the role of
408 overexpressed TMPRSS2 in cell-to-cell fusion, we first co-expressed TMPRSS2 with S-protein or with
409 μS1/S2 in HeLa-donor cells co-cultured with acceptor TZM-bl cells expressing ACE2. In agreement with
410 our cell biology data (Fig. 2), TMPRSS2 expression in donor cells (expressing the S-protein) abolished the
411 fusogenic activity of S, providing evidence that TMPRSS2-mediated retention of S-protein in the ER by
412 the generation of S2a and S2b impaired the cell-to-cell fusion activity of S-protein at the plasma membrane
413 (Fig. 6C).
414 We next analyzed the fusion of donor cells expressing WT-S, μS1/S2 or the Furin-optimized μS2' with
415 acceptor cells expressing ACE2 or ACE2 + TMPRSS2 (Fig. 6D). The data showed that TMPRSS2
416 expression reduced by ~2.2-fold the fusion of donor cells expressing WT-S but increased by ~3-fold that
417 of cells expressing μS1/S2 (Fig. 6D). While TMPRSS2 did not affect fusion of donor cells expressing μS2',
418 the latter displayed a nearly 2-fold less fusion than WT-S, suggesting that a more efficient Furin cleavage
419 (Fig. 2D) would not necessarily lead to enhanced fusion.

420 To determine the contribution of cell surface TMPRSS2 in the processing of S-protein and ACE2 and
421 their potential effects on cell-to-cell fusion we co-cultured donor cells expressing a double tagged S-protein
422 (HA at the N-terminus and V5 at the C-terminus) or its mutants, with acceptor cells expressing ACE2 or
423 ACE2+TMPRSS2. The fusion trends using double tagged WT-S (HA-S) or μS1/S2 (HA-μS1/S2) (Fig.
424 7A) were like those observed with the single V5-tagged S-proteins (Fig. 6D). As previously demonstrated
425 (Fig. 3A), ACE2 alone enhanced the production of S2' from WT-S by endogenous Furin (Fig. 7B).
426 However, the reduction of S-induced fusion of WT-S by TMPRSS2 (Fig. 7A) was associated with a
427 substantial ~4-fold decrease in S2 levels normalized to β-actin and ~1.5-fold increase in S2' levels (Fig.
428 7B). Unlike WT-S, μS1/S2-induced fusion was optimal when ACE2 and TMPRSS2 were co-expressed on
429 acceptor cells, albeit at ~2.5-fold lower levels than fusion of WT-S in the absence of TMPRSS2 (Fig. 7A)
430 and was associated with ~5-fold higher levels of S2' normalized to β-actin (Fig. 7B). In this assay, we
431 confirmed that co-expression of TMPRSS2 with ACE2: (**i**) modestly enhanced S2'; but (**ii**) did not affect
432 the secretion of S1 from WT-S or μS1/S2 (Fig. 7B; Media). In this co-culture system, TMPRSS2 expression
433 in acceptor cells did not generate S2a, S2b or S1', unlike what we observed previously (Figs. 2D,4A, SI-
434 Fig. 5) when TMPRSS2 and S-protein were co-expressed.
435 Since the mutant μS1/S2 (A<u>R</u>AA$_{685}$) can still be processed by TMPRSS2 at Arg$_{683}$↓ *in vitro* (Fig. 1C)
436 and in co-expression experiments (S2a in Fig. 2B), we next used the μAS1/S2 mutant (AAAA$_{685}$), which
437 was not cleaved at S1/S2 by either Furin or TMPRSS2 (SI-Fig. 3B). WT-S and μAS1/S2 mutant were
438 compared for their ability to induce cell-to-cell fusion with acceptor cells co-expressing ACE2 and
439 TMPRSS2 in the presence or absence of Camostat. As already observed, TMPRSS2 reduced the fusion of
440 WT-S (Figs. 6D; 7A), and 120 μM Camostat restored it (Fig. 8A). In contrast, TMPRSS2 enhanced the
441 fusion of μAS1/S2 by ~4-fold (Fig. 8A), a higher value than the ~2.5 to 3-fold observed with μS1/S2 (Figs.
442 6D; 7A). Befittingly, Camostat significantly reduced TMPRSS2-induced fusion of μAS1/S2 (Fig. 8A). WB
443 analyses of cells expressing WT-S (Fig. 8B) or μAS1/S2 (Fig. 8C) revealed that: (**i**) Camostat reduced the

444 shedding of ACE2; (**ii**) Camostat did not decrease the levels of S2' (Figs. 8B, C); (**iii**) with μAS1/S2,
445 TMPRSS2 did not enhance the levels of S2', but rather generated a smaller ~67 kDa product and released
446 a larger ~175 kDa fragment $S1_L$ into the media, both of which disappeared in the presence of Camostat
447 (Fig. 8C). These results suggest that cell surface TMPRSS2 might require a prior "priming" cleavage at
448 S1/S2 for the generation of *bona fide* S2'. This agrees with the notion that under our co-culture conditions
449 Furin-like enzymes are primarily involved in the priming of the WT-S-protein at the S1/S2 junction, and
450 TMPRSS2 and/or Furin can cleave S2 into S2'. However, the absolute levels of S2' detected by WB do
451 not seem to strictly correlate with fusion efficiency of WT-S, μS1/S2 and μAS1/S2 in absence or presence
452 of Camostat (Figs. 7, 8).

453 Based on the above observations, we explored the possibility that shedding of ACE2 [36] by TMPRSS2
454 into sACE2 (SI-Fig. 3B) may also be critical for fusion. To tease out the contribution of ACE2 cleavage by
455 TMPRSS2 and its seemingly opposite effects on fusion activity with WT-S or μAS1/S2 (and μS1/S2), we
456 tested the effect of a multiple Arg/Lys to Ala mutants in segments close to the transmembrane domain of
457 ACE2, namely ACE2 (C0), ACE2 (C4) *versus* ACE2 (C0+C4) (Fig. 9A), which have been described to
458 modify ACE2 cleavage by TMPRSS2 [36]. Accordingly, WB analyses (Fig. 9B) revealed that TMPRSS2,
459 but not its Ser* active site S441A mutant (μTMPR), can shed the membrane-bound ~120 kDa WT ACE2,
460 releasing major ~95 kDa and minor ~80 kDa forms. In contrast, TMPRSS2 primarily generated the ~80
461 kDa fragment from ACE2 (C0+C4) and ACE2 (C4), whereas ACE2 (C0) behaved as the WT.

462 In the presence of TMPRSS2 the extent of fusion would depend on a combination of reduced levels of
463 full-length cell surface ACE2 and increased levels of sACE2 that could act as a decoy to inhibit fusion [57].
464 Cell-to-cell fusion tested in co-culture revealed that ACE2 (C0+ C4) was no longer sensitive to TMPRSS2
465 impairment of WT-S-induced fusion. Thus, in the latter case the ~80 kDa form of sACE2 primarily
466 produced by TMPRSS2 cleavage of ACE2 (C0+C4) may no longer be able to inhibit WT-S-fusion
467 compared to the ~95 kDa form produced by TMPRSS2 cleavage of WT ACE2, effectively abrogating the
468 inhibitory effect of sACE2. This suggests that the C-terminal collectrin-like domain [58] that includes aa

469 697 and 716 of ACE2 (Fig. 9A), which is lost in the ~80 kDa form, may be critical for the ability sACE2
470 to inhibit cell-to-cell fusion of WT-S. Since Arg_{710} and Arg_{716} within the collectrin-like domain (Fig. 9A)
471 have been reported to be implicated in ACE2 dimerization [59], their Ala mutation in the ACE2 (C0+C4)
472 mutant likely would significantly reduce ACE2 dimerization. Whether dimerization of ACE2 and the ~95
473 kDa sACE2 are needed for efficient inhibition of WT-S-induced fusion [57] is yet to be confirmed. In that
474 context, a human recombinant sACE2 that includes the collectrin domain (hrsACE2, aa 1-740) effectively
475 blocked SARS-CoV-2 infection of Vero E6 cells [60].

476 To understand the distinct impact of the two TMPRSS2-induced shed forms of sACE2 on μAS1/S2-
477 induced fusion, we analyzed fusion of donor μAS1/S2 expressing cells with acceptor cells expressing
478 ACE2 (C0+C4). We observed that in this case fusion was lower than that measured with WT ACE2 (Fig.
479 9C), indicating a less favorable interaction of μAS1/S2-protein with ACE2 (C0+C4) than with WT ACE2.
480 Interestingly, in this case TMPRSS2 no longer enhanced fusion significantly (Fig. 9C), supporting the
481 notion the ~80 kDa form of sACE2 cannot enhance fusion of the μAS1/S2-protein. In the absence of S1/S2
482 processing (μAS1/S2), TMPRSS2 cleavage at S2' resulted in the formation of $S1_L$ (~175 kDa in Fig. 8C),
483 which was no longer detected in the media when ACE2 (C0+C4) was expressed on acceptor cells (Fig.
484 9D).

485 Altogether, these results suggest that the ~95 kDa sACE2 generated by TMPRSS2 (Figs. 6D; 7A; 8A),
486 might allow for a more efficient displacement of the inhibitory $S1_L$ cap, thereby facilitating cleavage at S2',
487 compared to membrane-bound ACE2 and the ~80 kDa form of sACE2 [57]. Altogether, our data indicate
488 that under overexpression conditions, the TMPRSS2-generated shedding of ACE2 has an opposite impact
489 on the S-induced fusion at the plasma membrane of WT-S *versus* μS1/S2 and μAS1/S2, highlighting the
490 functional importance of the acquisition of the Furin cleavage site at S1/S2 [10] for SAR-CoV-2 infection.
491

492 **Furin processing of SARS-CoV-2 variants.** Over the last 18 months a number of SARS-CoV-2 variants
493 have emerged (UK B.1.1.7, α-variant; South African B.1.351, β-variant; Brazil/Japan P.1, γ-variant; and
494 Indian B.1.617.2, δ-variant), exhibiting specific amino acid modifications of the S-protein [9]. A subset of
495 these variants seems to affect viral traits such as transmissibility, pathogenicity, host range, and antigenicity
496 of the virus [61]. The first D614G variant of the S-protein identified is now prevalent in most SARS-CoV-
497 2 strains [62]. It has been reported to affect virus stability [63], and infectivity especially in the presence of
498 ACE2 [64], and to possibly influence processing at S1/S2 [65], though this is controversial as it may be
499 cell-type dependent [66]. In HeLa cells we tested in the presence of ACE2 the effect of various S-variants
500 single (D614G; P681H; P681R) or combined mutants (D614G + P681H; N501Y + D614G + P681H;
501 E484K + N501Y + D614G). Our data showed that none of these variants significantly enhanced the
502 endogenous S1/S2 processing (except being slightly higher for P681H and P681R) and S2' processing in
503 HeLa-ACE2 cells or affected S1 secretion (SI-Fig. 9A). We surmise that the reported increased infectivity
504 and spread of SARS-CoV-2 carrying most of these variants may be more related to enhanced stability of
505 the S-protein, increased ACE2 receptor binding affinity or other factors for these combined variants, rather
506 than grossly affecting the S-protein cleavages by Furin, except maybe for P681R and P681H as observed
507 in HeLa-ACE2 cells.

508 Accordingly, we evaluated the cell-to-cell fusion activity of some of these variants (SI-Fig. 9B). The data
509 showed that compared to WT-S, the presence of the single D164G did not significantly affect fusion, but
510 that a ~2.4-fold higher fusogenic activity was observed for the double D164-N501Y variant. The only two
511 single variants that significantly enhanced by ~2-fold the cell-to-cell fusion were those affecting the P5
512 position at the S1/S2 site, slightly favoring its Furin processing (Fig. 9A), namely P681H (in the α-variant)
513 and P681R (in the δ-variant) (SI-Fig. 9B). However, the combination of the D164G and P681H mutations
514 with those of N501Y or E484K occurring within the RBD of S, did not have a significant influence on
515 fusion above that of the single N501Y mutant (SI-Fig. 9B). Interestingly the μS2' mutant with an optimized
516 Furin-like site exhibited partially reduced fusion, as previously observed (Fig. 6D), possibly reflecting that

517 for cell-to-cell fusion an efficient S2' processing by Furin that occurs early along the secretory pathway
518 may be a disadvantage.
519
520 **Effects of Furin inhibitors on entry of pseudoviruses.** To assess the relative importance of spike
521 processing at the S1/S2 and S2' sites in SARS-CoV-2 entry, we pseudotyped luciferase reporter gp160-
522 defective HIV particles with WT, μS1/S2 or μS2' S-protein and tested their ability to transduce human
523 lung-derived Calu-3 and kidney-derived HEK293T-ACE2 cells. Herein, we found that for cell-entry of
524 pseudoviruses (pp) expressing μS1/S2 the S-protein was defective in Calu-3 but enhanced by at least 10-
525 fold in HEK293T-ACE2 (Fig. 10A), suggesting that S processing at the S1/S2 site is required for optimal
526 viral entry in Calu-3 cells, but dispensable, or perhaps even less desirable in HEK293T-ACE2 cells. Since
527 these findings were similar to those in Vero E6 cells [67], we asked whether viral entry in KEK293T-ACE2
528 was through the same pH-dependent, endocytic route as reported for Vero cells [68]. Indeed, we observed
529 that chloroquine [69], which prevents endosomal acidification, efficiently blocked entry of ppSARS-CoV-
530 2 (SI-Fig. 10), indicating that in HEK293T-ACE2 the S-protein that mediates viral entry is activated by
531 endosomal pH-dependent proteases. This agrees with the fact that HEK293 cells allow endocytosis of
532 SARS-CoV-2 pseudovirions *via* clathrin-coated vesicles [70].
533 In the case of μS2'-S-expressing viral particles, entry was more efficient in both cell types (compare the
534 same-colored dots between WT-S and μS2'-S, Fig. 10A), implying that S cleavage at the optimized Furin-
535 like site could enhance viral entry. To further assess the role of Furin-like enzymes in this process, we used
536 the PC-inhibitor BOS-318 to block S-processing during biosynthesis of ppSARS-CoV-2 (Fig. 10B) and
537 asked whether this would affect viral entry in HEK293T-ACE2 and Calu-3 (Fig. 10C). To this end, we
538 found that treating viral particle-producing cells with BOS-318 blocked processing of WT-S and μS2'-S
539 while not affecting the overall expression profile of μS1/S2-S (Fig. 10B). However, not only did the
540 treatment not impact viral entry in HEK293T-ACE2, but it also enhanced pseudovirions-cell fusion by ~10-
541 fold for WT-S and ~2-fold for μS2'-S (Fig. 10C). In contrast, in Calu-3 cells inhibiting S-protein processing

542 by BOS-inhibitors during viral packaging resulted in a mean decrease of ~3.6- to ~12.5-fold in nano-
543 luciferase signal for WT-S or μS2'-S, respectively (Fig. 10C). Overall, BOS-318 treatment phenocopied
544 the effect of the μS1/S2 in both cell types

545 Having observed the effect of BOS-inhibitors on S processing during biosynthesis, we asked whether
546 pre-treating target cells with BOS-318 would affect ppSARS-CoV-2 entry. Using Calu-3, a model epithelial
547 cell line where viral entry occurs primarily through fusion at the plasma membrane [71], we observed
548 reduced viral entry by ~3.8-fold for WT-S and ~14-fold for μS2'-S (Fig. 10D), emphasizing a significant
549 contribution of Furin to the processing and priming of S at the plasma membrane. The fact that BOS-318
550 had a more pronounced effect on entry by μS2'-S-containing viral particles was not surprising because of
551 the presence of an optimized Furin-like S2' site. Furthermore, when comparing the effect of BOS-318 to
552 that of the TMPRSS2 inhibitor Camostat, we noticed a reverse trend, i.e., entry by WT-S ppSARS-CoV-2
553 was more affected by Camostat than that by μS2'-S viral particles. Here, the average reduction of ppSARS-
554 CoV-2 entry was by ~8.6-fold for WT-S and ~3.2-fold for μS2'-S (Fig. 10D), suggesting that Furin plays
555 a more prominent role in the entry of μS2'-S *versus* WT-S viral particles. Lastly, the combined pre-
556 treatment of both BOS-318 and Camostat led to a complete block of viral entry, highlighting the importance
557 of both Furin and TMPRSS2 in this process. Collectively, our data clearly demonstrate the importance of
558 S-processing by Furin and TMPRSS2 for efficient viral entry in target cells where the virus enters through
559 a fusion process at the plasma membrane.

560

561 **Furin-like inhibitors reduce virus production in SARS-CoV-2-infected cells.** The possible antiviral
562 effects of Furin-like inhibitors on SARS-CoV-2 replication were initially evaluated in Calu-3 cells
563 pretreated with 1 μM BOS-inhibitors for 24h before infection. A plaque assay showed that BOS-
564 inhibitors significantly decreased viral titers at 12, 24 and 48h post-infection (Fig. 11A). We further
565 evaluated whether the inhibitory effect was dose-dependent and found that the titer of progeny viruses
566 was reduced by >30-fold with 1 μM BOS-318, although the inhibition could be observed starting at

567 0.25 μM (Fig. 11B; left panel). As well, the IC_{50} and selectivity index [72] of BOS-318 were found to
568 be 0.2 μM and 475, respectively, underlining the inhibitor's *bona fide* efficacy (Fig. 11B; right panel).
569 A similar analysis with BOS-857 and BOS-981 revealed comparable antiviral effects and selectivity
570 index (SI-Figs. 12A, B). Importantly, the levels of viral spike (full length and cleaved S) and
571 nucleocapsid proteins in Calu-3 cells treated with different doses of BOS-318 and the corresponding
572 progeny virus levels were similarly decreased (Fig. 11C), underscoring the crucial role played by
573 Furin-like convertases in the production of infectious SARS-CoV-2 during infection of lung epithelial
574 cells. In addition, the antiviral effect of these inhibitors on SARS-CoV-2 infection was also evaluated
575 in Vero E6, a cell target that is reported to be primarily infected *via* the endocytic pathway [11, 24]. In
576 this system, the best inhibitory effect with 1 μM BOS-318 demonstrated a modest ~5.7-fold decrease
577 in virus production sustained over a 12-48h infection period (SI-Fig. 13), possibly reflecting some
578 Furin-activity in endosomes [39].
579 Based on the selectivity index of BOS-inhibitors in Vero E6 and Calu-3 cells, BOS-318 and BOS-
580 981 were further used in combination with Camostat to explore a potential synergistic effect of these
581 inhibitors on viral replication in Calu-3 cells. To this end, we observed that the two inhibitors could
582 individually and meaningfully reduce viral replication, but their co-treatment (1 μM BOS-inhibitor +
583 100 μM Camostat) inhibited ~95 ± 2.5% of progeny viruses (Fig. 11D and SI-Fig. 13). This highlights
584 a synergistic effect of these drugs and the importance of endogenous Furin-like proteases and
585 TMPRSS2 in promoting efficient infection of Calu-3 cells by SARS-CoV-2. Accordingly, we
586 schematized these results in a model of infectious SARS-CoV-2 and the effect of Furin ± Camostat on
587 viral entry in Calu-3 *versus* HEK293 or Vero E6 cells (Fig. 12).

588

589

590

591 ## Discussion

592 Herein, we analyzed the implication of Furin [10, 12, 18, 24] and TMPRSS2 [18, 24] in proS-processing,
593 S-induced cell-to-cell fusion, SARS-CoV-2 entry and infectivity of various cell lines. Our study teased out
594 the independent and complementary roles of Furin and TMPRSS2 in promoting SARS-CoV-2 entry. *In*
595 *vitro* Furin cleaved mainly at S1/S2, but S2'was also cleaved at 50-fold higher Furin concentrations (Fig.
596 1B). The Furin-mediated S1/S2-cleavage activity was blocked by BOS-inhibitors (Fig. 5D). Conversely,
597 TMPRSS2 cleaves synthetic peptides encompassing both S1/S2 and S2' cleavage sites (Fig. 1B). In cells,
598 the endogenously expressed Furin-like enzymes induce efficient intracellular priming of the S-protein at or
599 beyond the TGN. Conversely overexpression of active TRMPSS2 in cells producing the S-protein induces
600 an early S-processing in the ER. Furin and less so PC5A can also induce an additional cleavage at S2',
601 which is essential to expose the fusion peptide (Fig. 1A). The S2'-processing was strongly enhanced in the
602 presence of ACE2 (Fig. 3A). It is thus likely that *via* the RBD the interaction of the S1-subunit with the
603 ACE2 receptor induces a conformational change favoring S2'-processing by cognate convertases [46]. We
604 propose that Furin-like enzymes first process proS at S1/S2, generating the cleaved S1- and S2-subunits
605 that remain non-covalently bound [12, 73]. This priming process is known to induce an initial
606 conformational change that exposes the RBD domain [74]. The subsequent interaction of S1-protein with
607 the ACE2 receptor would then induce a second conformational change leading to the exposure of the S2'
608 cleavage site, which can be cleaved by Furin or cell surface TMPRSS2. Interestingly, while Furin is mostly
609 found in the TGN, in polarized cells such as those of the lung, small intestine and kidney, it also
610 localized in endosomes and over apical and basolateral plasma membranes [75]. In contrast, TMPRSS2
611 seems to be localized mostly at the apical membrane of secretory epithelia [76]. Therefore, the relative
612 levels of active Furin and TMPRSS2 may vary between the apical and basolateral sides of SARS-CoV-
613 2 infected cells, with TMPRSS2 levels being highest on the apical side. Given that lung epithelial cells
614 are physiologically-polarized, the relative abundance of these enzymes at the apical membrane facing the
615 lumen of the respiratory airways may be an important factor governing which of the two enzymes might

616 cleave S at the S2' cleavage site. In that context, SARS-CoV-2 exhibits a polarity of infection in human
617 airway epithelium only from the apical membrane as it infects ciliated and goblet cells, but not basal
618 and club cells [77]. Thus, on the apical side both TMPRSS2 and Furin would be poised to process the
619 S-protein.

620 The S2' cleavage liberates the N-terminal domain of the fusion peptide that promotes virus entry and/or
621 cell-to-cell fusion. Separation of these subunits in the presence of ACE2 would then favor Furin-cleavage
622 at S2' and cellular fusion. BOS-inhibitors effectively blocked the generation of S2 and S2' by endogenous
623 Furin-like enzymes in HeLa-ACE2 cells (Fig. 5E), and in turn limited the pH-independent virus entry and
624 cellular fusion. Immunocytochemical data confirmed that ACE2 co-localized at the cell surface of HeLa
625 cells with WT-S and its μS1/S2 mutant, suggesting that endogenous cleavage at S1/S2 does not affect the
626 trafficking of S-protein (SI-Fig. 7). Notably, expression of μS1/S2 or treatment with BOS-inhibitors
627 prevented cell-to-cell fusion (Fig. 7), which is known to induce cytopathic effects. These results indicated
628 that Furin-cleavage may favor fusion and therefore allow the pH-independent entry of the virus. Thus, S-
629 processing by Furin was also shown to be essential for optimal pseudoviral entry in Calu-3 cells, since
630 abrogating this process with BOS-inhibitors effectively rendered the pseudovirions largely defective.
631 Conversely, in Vero or HEK293 cells, where the virus is known to enter *via* a pH-dependent entry pathway,
632 viral entry was improved with BOS inhibitor or μS1/S2. This suggests that in these cells Furin processing
633 of WT-S is dispensable or even less favourable for fusion, likely because endosomal proteases (e.g.,
634 cathepsins) can substitute for Furin and induce S-protein processing [78, 79]. Thus, in human lung cells our
635 data support a critical role of Furin in the pH-independent fusion process, where BOS-inhibitors
636 meaningfully reduce viral infection and production of infectious progeny virus (Fig. 10). The inhibition of
637 such infection pathway could strongly impair SARS-CoV-2 pathogenicity. In that context, viruses lacking
638 the FCS (ΔPRRA), are poorly infectious in small animal models [27, 28].

639 The key role played by Furin-mediated S1/S2 cleavage was confirmed by mutagenesis analysis. Alanine
640 mutagenesis first revealed the importance of basic amino acid for *in vitro* S1/S2 cleavage by Furin.

641 Analyzing the S-protein processing by WB confirmed the effect of mutations on Furin-mediated cleavage
642 and resulted in a reduced infection of Calu-3 cells and decreased cell-to-cell fusion. We also determined
643 the impact of mutation observed in the FCS of emerging SARS-CoV-2 variants (UK B.1.1.7, α-variant
644 P681H; and Indian B.1.617.2, δ-variant P681R) were the P5 residue is substituted by His or Arg,
645 respectively. Here we showed that the δ-variant was more sensitive to Furin cleavage, whereas the cleavage
646 of the α-variant was not increased *in vitro.* In contrast, in the context of the full-length protein both mutants
647 (α and δ variant) are slightly better processed at the S1/S2 cleavage site and we demonstrated that these
648 mutations significantly enhanced by ~2-fold cell-to-cell fusion. Conversely, mutations in the FCS barely
649 impact, or slightly increase virus entry in Vero E6 cells that are infected by the pH-dependent entry pathway
650 [80, 81]. Nevertheless, our results, together with the dramatic effect of mutation of the FCS (ΔPRRA) in
651 infection of small animal models [27, 28], suggest that mutation in the FCS impacting the Furin cleavage
652 regulates the infectivity of certain variants, which may associate with viral pathogenicity.
653 TMPRSS2 has been shown to enhance the infectivity of SARS-CoV-1 and MERS-CoV *via* cleavages of
654 the S-protein (extensively reviewed in [4, 15, 23]). In the case of SARS-CoV-1 the S1/S2 site
655 VSLL**R**$_{667}$↓ST contains an Arg↓Ser cleavage motif that is propitious to cleavage by TMPRSS2 [82] but
656 not by Furin. Furthermore, the activation of the S-protein of SARS-CoV-1 and cell-to-cell fusion were only
657 seen when donor cells expressing the S-protein were co-cultured with acceptor cells expressing both ACE2
658 and TMPRSS2 [82]. This is like our observations with SARS-CoV-2. Accordingly, herein we evaluated in
659 detail the direct role of TMPRSS2 in the processing of S-protein of SARS-CoV-2. Unexpectedly, we
660 showed that in HeLa and HeLa-ACE2 cells overexpressed TMPRSS2 induces the cleavage of proS at
661 S1/S2 and S2' in cells expressing the WT-S-protein. Such proteolytic cleavage was shown to occur in the
662 ER and lead to the formation of non-O-glycosylated S2a and S2b products retained in the ER (Figs. 1C;
663 2D; 4). Accordingly, high levels of TMPRSS2 in cells expressing S-protein limit the cell surface expression
664 of the latter and abolish cell-to-cell fusion (Fig. 6C). In addition, overexpression of cell-surface localized
665 TMPRSS2 with ACE2 in acceptor cells decreases S-induced fusion of donor cells. This effect was

666 abolished when ACE2 was modified in the collectrin domain of ACE2 (C0+C4) so that TMPRSS2 no
667 longer sheds it into a long ~95 kDa form of sACE2 but rather generates a shorter C-terminally truncated
668 ~80 kDa form that lacks the Collectrin-like domain needed for dimerization (Fig. 9A). We believe that the
669 TMPRSS2 induced ACE2 shedding (Figs. 4, 8), and that sACE2 acted as a decoy to inhibit membrane
670 fusion. In contrast, fusion of donor cells synthesizing μS1/S2 (resistant to Furin cleavage) was enhanced
671 when acceptor cells express both TMPRSS2 and ACE2 (Fig. 4D). In this case, the secreted sACE2 may
672 help the exposure of S2' by removal of the longer N-terminal $S1_L$ produced by TMPRSS2. Indeed,
673 TMPRSS2 no longer significantly enhances fusion with ACE2 (C0+C4), likely because the short ~80 kDa
674 form of sACE2 can no longer facilitate cleavage at S2' and/or removal of $S1_L$.

675 Our data also show that virions emanating from Calu-3 cells that endogenously express both Furin and
676 TMPRSS2 are infectious. In this case, it is possible that the limiting endogenous levels of TMPRSS2 in
677 acceptor Calu-3 cells are insufficient to inactivate proS in the ER, and that at physiological levels this
678 enzyme exerts its effects primarily at the cell surface. In addition, the membrane (M)-protein and/or
679 envelope (E)-protein of SARS-CoV-2 may shield the proS-protein from early TMPRSS2-induced
680 inactivation in the ER [83]. We also hypothesize that in the context of endogenous expression of ACE2 and
681 TMPRSS2 (e.g., in human lung epithelium-derived Calu-3 cells) [84], the proper balance between the two
682 forms of sACE2 (~95 kDa and ~80 kDa) might facilitate fusion. In this context, low levels of TMPRSS2
683 might be insufficient to generate enough soluble ACE2 to act as a decoy and TMPRSS2 might then directly
684 facilitate the generation of S2'. Our study highlights a complex dynamic between Spike, ACE2, Furin and
685 TMPRSS2 and points to a potential role of TMPRSS2 in facilitating S1 detachment from S2 to enhance S2
686 cleavage and ultimately, viral entry.

687 The human airway epithelium is an important site of early SARS-CoV-2 infection [18, 24, 85]. The virus
688 can then disseminate to other tissues/cells such as gut, liver, endothelial cells and macrophages where
689 ACE2, Furin and TMPRSS2 are co-expressed [86] and cause multi-organ dysfunction in COVID-19
690 patients [87]. The complementarity and interchangeability of these different proteases, together with

691 proteases expressed in endosomes, e.g., cathepsin L [88], allow SARS-CoV-2 entry into various cells,
692 which might explain the wider tropism of this virus compared to SARS-CoV-1 [89], favoring systemic
693 infections. Our data support the notion that Furin cleavage is mainly involved in the S1/S2 processing of
694 SARS-CoV-2, which is absolutely required for the pH-independent entry pathways [68], and for syncytium
695 formation. The FCS is conserved in viruses infecting human population, suggesting that this entry pathway
696 favoured the inter-human transmission and the viral pathogenesis. Interestingly, the FCS is unstable
697 (negatively selected) in Vero cells and viruses lacking the PRRA residues were detected after few passages
698 in such cells [90]. This instability of the FCS may be related to the fact that viral entry into Vero cells
699 occurs by the pH-dependent pathway, which is inhibited by chloroquine and hydroxy-chloroquine [69, 91].
700 Thus, depending on the cell-type our data support the presence of two entry pathways of SARS-CoV-2 [68,
701 81]. The fact that hydroxy-chloroquine therapy failed to show significant improvement in COVID-19
702 patients [92, 93] or in two animal models [94], suggests that even if the pH-dependent entry participates in
703 virus propagation, this entry pathway is not sufficient to fully explain the systemic infection and
704 pathogenesis of SARS-CoV-2. This is also supported by the facts that the Furin-cleavage at S1/S2 is
705 conserved in SARS-CoV-2 isolated from human COVID-19 patients, and that ΔPRRA viruses, are poorly
706 infectious in hamster [92]. Thus, these observations suggest that the pH-independent pathway is an
707 important antiviral target and inhibiting the S1/S2 cleavage should impair virus dissemination.
708 Accordingly, we demonstrated that BOS-inhibitors inhibited the Furin-mediated cleavage at the
709 nanomolar range *in vitro*. In addition, BOS-inhibitors strongly impaired the S1/S2 processing, limited
710 cell-to-cell fusion and pH-independent virus entry and dramatically reduced virus propagation in Calu-
711 3 (Figs. 5, 6, 10, 11). BOS-inhibitors represent non-toxic, small molecule inhibitors, which can be
712 delivered orally or by inhalation, and thus deserve to be rapidly tested to assess their antiviral effect
713 against acute SARS-CoV-2 infection. As observed in adult animal models, short-term inhibition of
714 Furin would not cause severe side effects, despite the many physiological functions of Furin [20]. Our
715 data strongly support the notion that a combination of BOS- and selective TMPRSS2-inhibitors would

716 provide an effective blockade against SARS-CoV-2 entry/infection, and in this context, further studies
717 are required to validate this approach in small animal models. It would be interesting to validate *in vivo*
718 whether a combination of BOS-inhibitor, Camostat and hydroxy-chloroquine would maximize the
719 antiviral effect of these entry inhibitors.

720 The availability for worldwide distribution of various SARS-CoV-2 vaccines that inhibit the
721 accessibility of the RBD of S-protein to ACE2 (https://www.raps.org/news-and-articles/news-
722 articles/2020/3/covid-19-vaccine-tracker) represent a major therapy to block SARS-CoV-2 infections.
723 However, it is unknown whether they will be effective in patients with impaired immune systems, and
724 whether they will confer a persistent protection. While the protective effect of the vaccination on the
725 whole world population remains incomplete, additional effective antiviral drugs that block viral entry
726 in multiple organs are still needed and could help in early diagnosis of the disease. Ultimately, in case
727 of new emerging coronavirus pandemics [95], the availability of such treatments would constitute a
728 powerful anti-viral arsenal.

729

730 **Materials and Methods**

731 **Enzymatic PC-inhibition by BOS-inhibitors**

732 Biochemical assay: The proprotein convertases Furin (108-574-Tev-Flag-6His), PC5A (PCSK5; 115-
733 63-Tev-Flag-6His), PACE4 (PCSK6; 150-693-Tev-Flag-6His), and PC7 (PCSK7; 142-634-Tev-Flag-
734 6His) enzymes were purified from BacMam transduced CHO cells. Reactions were performed in black
735 384-well polystyrene low volume plates (Greiner) at a final volume of 10 µL. BOS-inhibitors (BOS-
736 318, BOS-857 and BOS-981) were dissolved in DMSO (1 mM) and serially diluted 1 to 3 with DMSO
737 through eleven dilutions to provide a final compound concentration range from 0.00017 to 10 µM.
738 0.05 µl of each concentration was transferred to the corresponding well of an assay plate, and then 5
739 µl of enzyme (Furin, PCSK5, PCSK6, and PCSK7) in assay buffer (100 mM HEPES pH7.5, 1 mM

740 $CaCl_2$ and 0.005% Triton X-100) was added using a Multidrop Combi (Thermo) to the compound
741 plates to give a final protein concentration of 0.02, 0.5, 2.5, and 1.0 nM respectively. The plates were
742 mixed by inversion and following a 30 min preincubation of enzyme with compound at room
743 temperature (~22ºC), the substrate FAM-QRVRRAVGIDK-TAMRA (AnaSpec # 808143, 5 µl of a 1,
744 0.25, 0.20, and 0.5 µM solution in assay buffer for Furin, PCSK5, PCSK6, and PCSK7 respectively)
745 was added using a Multidrop Combi to the entire assay plate. The plates were centrifuged at 500Xg
746 for 1 minute and incubated at room temperature for two hours. Enzyme inhibition was then quantified
747 using an Envision instrument (PerkinElmer). Data were normalized to maximal inhibition determined
748 by 1 µM Decanoyl-Arg-Val-Lys-Arg-Chloromethylketone (Calbiochem #344930). Golgi imaging
749 assay: This assay uses an image-based platform to evaluate the intracellular activity of Furin inhibitors.
750 Reactions were performed in black 384-well, tissue culture-treated, clear bottom plates (Greiner).
751 Compounds under analysis were dissolved in DMSO (1.0 mM) and serially diluted 1 to 3 with DMSO
752 through eleven dilutions. This creates a final compound concentration range from 0.00017 to 10 µM,
753 and 0.1 µL of each concentration was transferred to the corresponding well of the assay plate.

754 Cellular assay: Analyses were initiated by the addition of U2OS cells simultaneously transduced with
755 a BacMam-delivered construct containing a Golgi-targeting sequence followed by a 12-amino acid
756 Furin/PCSK cleavage site from Bone Morphogenic Protein 10 (BMP10) and then GFP at the C
757 terminus. The dibasic Furin cleavage site sequence was flanked by glycine rich linkers (GalNAc-T2-
758 GGGGS-DSTARIRRNAKG-GGGGS-GFP). Briefly, frozen cells are thawed in assay media
759 (Dulbecco's Modified Eagles Medium Nutritional Mixture F-12 (Ham) without phenol red containing
760 5% FBS) and diluted to deliver 6000 cells/well (50 µl) to the plate using a Multidrop Combi (Thermo).
761 After a 24-hour incubation period at 37ºC, the cells are stained with Cell Mask Deep Red, fixed in
762 paraformaldehyde and the nuclei stained using Ho33342. The Golgi-targeted GFP forms bright
763 punctate clusters within the cell. In the absence of a Furin/PCSK inhibitor, the endogenous protease

764 cleaves GFP from its N-acetylgalactosaminyltransferase-2 Golgi tether, releasing GFP into the Golgi
765 lumen where fluorescence was diluted below the threshold of assay sensitivity. In the presence of a
766 cell permeable Furin/PCSK inhibitor, GFP fluorescence increases as intra-Golgi protease activity was
767 reduced. Cellular GFP intensity was determined by image-based acquisition (Incell 2200, Perkin
768 Elmer) at 40x magnification with 4 fields measured per well. Multi-scale top hat segmentation was
769 used to identify the GFP-tagged puncta and to quantitate the average fluorescence of all puncta on a
770 per cell basis. Cellular toxicity was determined in parallel.

771 Furin and TMPRSS2 fluorogenic assays: Recombinant Furin was purchased from BioLegend
772 (#719406), human recombinant TRMPSS2 from Cliniscience (ref LS-G57269-100), and the
773 DABCYLGlu-EDANS labelled peptides encompassing the different cleavage sites (SI Table 1) were
774 purchased from Genscript. Reactions were performed at room temperature in black 384-well
775 polystyrene low volume plates (CELLSTAR-Greiner Bio-One # 784476) at a final volume of 15 µL.
776 The fluorescent peptides were used at 5 µM and the reactions were performed in 50 mM Tris buffer (pH
777 6.5 or 7.5), 0.2% Triton X-100, 1mM $CaCl_2$ and Furin was added at a final concentration of 0.2 to 100
778 nM. BOS-inhibitors (BOS-318, BOS-857 and BOS-981) were dissolved in DMSO (1 mM) and serially
779 diluted 1 to 2 with DMSO to provide a final compound concentration range from 50 µM to 0.01 nM
780 with 5% DMSO in the enzymatic assay. For TMPRSS2, the fluorescent peptides were used at 5 µM
781 and the reactions were performed in 50 mM Tris buffer (pH 8), 150 mM NaCl and TMPRSS2 was
782 added at final concentrations of 50 nM. Cleavage of the synthetic peptides was quantitated by
783 determining the increase of EDANS (493 nM) fluorescence following release of the DABCYL
784 quencher, which was excited at 335 nM using a Safire 2 Tecan fluorimeter. The fluorescence was
785 followed during 90 min, and the enzymatic activity was deduced by measurement of the increase of
786 fluorescence during the linear phase of the reaction. Each reaction was performed in triplicate and the
787 standard deviation was calculated using Excel-ecart type function ($\sqrt{\frac{\sum(x-\bar{x})^2}{(n-1)}}$).

788 **Plasmids**

789 Single tagged (C-terminal V5 tag) or double tagged (N-terminal HA tag and C-terminal V5 tag) Spike
790 glycoprotein of SARS-CoV-2 (optimized sequence) and its mutants were cloned into the pIRES2-
791 EGFP vector. Site-directed mutagenesis was achieved using a Quick-Change kit (Stratagene, CA)
792 according to the manufacturer's instructions. The plasmids pCI-NEO-hACE2 received from DW
793 Lambert (University of Leeds) and pIRES-NEO3-hTMPRSS2 from P Jolicoeur (IRCM). The ΔEnv
794 Vpr Luciferase Reporter Vector (pNL4-3.Luc.R-E-) was obtained from Dr. Nathaniel Landau through
795 the NIH AIDS Reagent Program whereas the pHIV-1NL4-3 ΔEnv-NanoLuc construct was a kind gift
796 from Dr. P Bieniasz. Plasmids encoding VSV-G, as HIV-1 Env and tat were previously described [96,
797 97].

798 **Cell culture and transfection**

799 Monolayers of HeLa, HEK293T, HEK293T17, Vero E6 and Calu-3 cells were cultured in 5% CO_2 at
800 37°C in Dulbecco's modified Eagle's medium (DMEM; Wisent) supplemented with 10% (v/v) fetal
801 bovine serum (FBS; Wisent). HEK293T-ACE2[98], a generous gift from Dr. Paul Bieniasz, were
802 maintained in DMEM containing 10% FBS, 1% nonessential amino acids (NEAA) and 50 µg/ml
803 blasticidin (Invivogen). CHO-ldlD cells, which are defective in UDP-Gal/UDP-GalNAc 4-epimerase [50]
804 and therefore cannot O-glycosylate proteins, and their parental CHO-K1 cells were cultured in DMEM/F12
805 medium (50/50) (Wisent) supplemented with 3% FBS and F12K medium (Wisent) containing 10% FBS,
806 respectively. The cells were transfected with JetPrime transfection reagent according to the
807 manufacturer's instructions (Polyplus transfection, New York, USA). At 24h post transfection the
808 culture media were changed to serum-free medium and incubated for an additional 24h. To establish
809 the stable HeLa cells over-expressing human ACE2, transfected cells were selected using media
810 containing 500 µg/ml of neomycin (G418, Wisent).

811 For knockdown of Furin in HeLa cells, an optimized set of 4 small interfering RNAs (siRNAs;
812 SMARTPool) targeted against human Furin were purchased from Horizon Discoveries (Perkin Elmer,

813 Lafayette, LA, USA) and transfections of HeLa cells were carried out using INTERFERin (PolyPlus)
814 as recommended by the manufacturer.

815 To generate HIV particles pseudotyped with SARS-CoV-2 S, 293T17 cells (600,000 cells plated in
816 a 6-well vessel) were transfected with 1 µg pNL4-3.Luc.R-E- (or pHIV-1NLΔEnv-NanoLuc) in the
817 presence or absence of 0.3 µg pIR-2019-nCoV-S V5 plasmids using Lipofectamine-3000 (Life
818 Technologies). In certain experiments, 293T17 cells were treated with BOS inhibitors at 6 h post
819 transfection. Pseudovirions expressing the nano- or firefly-luciferase were collected at 24 h or 48 h
820 post transfection, respectively. Viral supernatants were clarified by centrifugation at 300 x *g,* passed
821 through a 0.45-µm pore-size polyvinylidene fluoride (PVDF; Millipore) syringe filter (Millipore;
822 SLGVR33RS), and aliquots frozen at −80°C. For WB analysis of purified pseudovirions, viral
823 supernatants were concentrated by ultracentrifugation on a 20% sucrose cushion for 3h at 35,000 RPM;
824 Beckman Coulter OPTIMA XE; Ti70.1 rotor). HIV particles lacking the SARS-CoV-2 S glycoprotein
825 served as a negative control in all experiments.

826

827 **Cell viability assay using MTT**

828 Cells, seeded in a 96-well plate, the day before, at 10,000 (HEK-293T and Vero E6) or 50,000 (Calu-
829 3) cells, were treated with serial 10-fold dilutions of BOS inhibitors for up to 48h. Cells treated with
830 vehicle alone were used as negative control. MTT was subsequently added to the medium (final
831 concentration: 2.5 mg/ml) and cells were further incubated for 4h at 37 ^{0}C. After removal of the culture
832 media, DMSO was added and absorbance read at 595 nm using a microplate spectrophotometer. The
833 data from two independent experiments done in triplicates was used to calculate the CC50 by nonlinear
834 regression using GraphPad Prism V5.0 software.

835 **Western blots**

836 The cells were washed with PBS and then lysed using RIPA buffer (1% Triton X-100, 150 mM NaCl,
837 5 mM EDTA, and 50 mM Tris, pH 7.5) for 30 min at 4ºC. The cell lysates were collected after
838 centrifugation at 14,000 × g for 10 min. The proteins were separated on 7% tris-glycine or 8% tricine
839 gels by SDS-PAGE and transferred to a PVDF membrane (Perkin Elmer). When specified, media from
840 cultured and transfected cells were collected and concentrated 10x using Amicon Ultra 2 ml devices
841 with a 10 kDa cut-off (Millipore; UFC 201024), as specified by the manufacturer, and analyzed by
842 SDS-PAGE followed by Western blotting. The proteins were revealed using a V5-monoclonal
843 antibody (V5-mAb V2660; 1:5000; Invitrogen), ACE2 antibody (rabbit monoclonal ab108252;
844 1:3,000; Abcam), TMPRSS2 antibody (rabbit polyclonal; 14427-1-AP; 1:1,000; Proteintech), Actin
845 antibody (rabbit polyclonal A2066; 1:5,000; Sigma), HA-HRP antibody (12-013-819; 1:3,500; Roche),
846 or SARS-CoV-2 spike antibody (rabbit polyclonal GenTex GTX135356; 1:2,000; GenTex). The
847 antigen-antibody complexes were visualized using appropriate HRP conjugated secondary antibodies
848 and enhanced chemiluminescence kit (ECL; Amersham or Bio-Rad) and normalization was reported
849 to β-actin. The quantification of the bands was performed using Image Lab software (Bio-Rad).
850 For analysis of SARS-CoV-2 S virions or pseudovirions, protein extracts of purified viral particles
851 and corresponding producing cells (Calu-3 or 293T17, respectively) were resolved on 10% tris-glycine
852 gels and immunoblotted for spike, nucleocapsid, HIV-1 Gag p24 or actin using anti-V5 (for
853 pseudovirion detection; V2660)/anti-S2 (for virion detection; Sino Biologicals; 40590-T62), anti-N
854 (Sino Biologicals; 40143-MM05), anti-p24 (MBS Hybridoma line 31-90-25) or anti-actin (MP
855 Biomedicals, SKU 08691001), respectively.

856 **Glycosidase treatment**

857 30 to 50 μg proteins were digested for 90 min at 37ºC with endoglycosidase-H (Endo-H; P0702L) or
858 endoglycosidase-F (Endo-F; P0705S) as recommended by the manufacturer (New England Biolabs).

859 **Inhibitor treatment**

860 At 24h post transfection, cells were incubated for 6h with two pan-PC inhibitors: the cell permeable
861 decanoyl-RVKR-chloromethylketone (cmk; 50 mM; 4026850.001; Bachem) , or with the cell surface
862 PC-inhibitor hexa-D-arginine (D6R; 20 μM; 344931; EMD). Culture media were then replaced with
863 fresh ones containing the inhibitors for an additional 24h. For the selective cell-permeable Furin-like
864 inhibitors (BOS; Boston Pharmaceuticals), the cells were treated with the inhibitors at the specified
865 concentration starting at 5h pre-transfection and throughout the duration of the experiment.

866 **Cell-to-cell fusion assay**

867 HeLa or HeLa TZM-bl cells were plated at 200,000 cells in 12-well plates. HeLa cells were transiently
868 transfected with different constructs of SARS-CoV-2 Spike or NL4.3-HIV Env, or an empty vector
869 and 0.2 μg of CMV-Tat plasmid. HeLa TZM-bl cells were transfected with human ACE2, TMPRSS2
870 or a combination of both. At 6h post-transfection, media were replaced with fresh ones containing
871 Furin-inhibitors, and 24h later the cells were detached with PBS-EDTA (1 μM). Different
872 combinations of HeLa and HeLa-TZM-bl cells were placed in co-culture plate at a ratio of 1:1 for a
873 total of 60,000 cells/well of a 96 well place. After 18-24h the media were removed and 50 μl of cell
874 lysis reagent was added in each well. 20 μl of the cell lysate was used for luciferase reading using 50
875 μl of Renilla luciferase reagent (Promega, Madison, WI, USA). The relative light units (RLU) were
876 measured using a Promega GLOMAX plate reader (Promega, Madison, WI, USA) and values were
877 reported as fold increase over the RLU measured in co-culture of HeLa cells transfected EV with
878 respective TZM-bl cells.

879 **Protein immunoprecipitation from co-culture media**

880 When indicated, the secreted form of double tagged Spike glycoprotein of Sars-CoV-2 (N-terminal
881 HA tag and C-terminal V5 tag) and the TMPRSS2-shed forms of ACE2 receptor from the FBS
882 containing media of co-cultured HeLA and HeLa-TZM-bl cells were immunoprecipitated for WB
883 analyses. Namely, 0.3 ml of media were immunoprecipitated with either 25 μl EZ view Red anti-HA

884 affinity gel (E 6779; Sigma-Aldrich) or 1.2 µg ACE2 antibody (goat ployclonal AF 933; R&D) and 30
885 µl TrueBlot anti-Goat Ig IP beads (00-8844-25; Rockland Inc.), respectively, according to the
886 manufacturers' protocol. Upon SDS-PAGE separation and PVDF transfer, the immunoprecipitated
887 proteins were detected using an HA-HRP antibody (12-013-819; 1:3,500; Roche) or ACE2 antibody
888 (rabbit monoclonal ab108252; 1:3,000; Abcam) and TrueBlot anti-Goat IgG HRP (18-8814-31;
889 Rockland Inc.), respectively.

890 **Microscopy**

891 To establish the luciferase assay, cell co-cultures were plated on glass coverslips. After 18-24h, the
892 cells were incubated with 488 CellMask™ to stain the membrane and then fixed with 4% PFA for 15
893 min at 4ºC. The glass coverslips were mounted on glass slides using ProLong™ Gold Antifade
894 containing DAPI (Invitrogen). The number of syncytia were counted over 10 fields.

895 **Immunofluorescence**

896 Cell culture and transfection were performed on glass coverslips. Cells were washed twice with PBS
897 and fixed with fresh 4% paraformaldehyde for 10 min at room temperature. Following washes, cells
898 were either non-permeabilized or permeabilized with 0.2% Triton X-100 in PBS containing 2% BSA
899 for 5 min, washed, and then blocking was performed with PBS containing 2% BSA for 1h. Cells were
900 incubated with primary antibodies overnight at 4ºC using an antibody against V5 (mouse monoclonal
901 R960-25; 1:1000; Invitrogen), Spike (mouse monoclonal GTX632604; 1:500; GeneTex) and ACE2
902 (goat polyclonal AF933; 1:500; RnDsystems). Following wash, corresponding species-specific Alexa-
903 Fluor (488 or 555)-tagged antibodies (Molecular Probes) were incubated for 1h at room temperature.
904 Coverslips were mounted on a glass slide using ProLong Gold Reagent with DAPI (P36935, Life
905 Technologies). Samples were visualized using a confocal laser-scanning microscope (LSM710, Carl
906 Zeiss) with Plan-Apochromat 63x/1.40 Oil DIC M27 objective on ZEN software.

907 **Pseudovirus entry**

908 HEK293T-ACE2 or Calu-3 (10,000 cells/well plated in a 96-well dish 24 or 48h before, respectively)
909 were incubated with up to 200 µl filtered pseudovirions for overnight. In certain experiments, target
910 cells were pretreated with BOS-318 (1 µM) for 6h and/or Camostat (40 µM) for 2h before transduction.
911 The overnight incubation with pseudovirions was performed in the presence of the inhibitors. Viral
912 inoculum was removed, then fresh media were added, and the cells cultured for up to 72h. Upon
913 removal of spent media, 293T-ACE2 and Calu-3 cells were gently washed twice with PBS and
914 analyzed for firefly- or nano- luciferase activity, respectively using Promega luciferase assay (Cat #
915 E1501) or Nano-Glo luciferase system (Cat # N1110), respectively.

916 **Replication competent SARS-CoV-2 Viruses**

917 SARS-CoV-2, which served as the viral source, was originally isolated from a COVID-19 patient in
918 Quebec, Canada and was designated as LSPQ1. The clinical isolate was amplified, tittered in Vero E6
919 using a plaque assay as detailed below, and the integrity of the S-protein multi-basic protein convertase
920 site validated by sequencing. All experiments involving infectious SARS-CoV-2 virus were performed
921 in the designated areas of the Biosafety level 3 laboratory (IRCM) previously approved for SARS-
922 CoV-2 work.

923

924 **Plaque assay in Vero E6**

925 Vero E6 cells (1.2 x 10^5 cells/well) were seeded in quadruplicate in 24-well tissue culture plates in
926 DMEM supplemented with 10% FBS two days before infection. Cells were infected with up to six ten-
927 fold serial dilutions (10^{-2}-10^{-6}) of viral supernatant containing SARS-CoV-2 for 1h at 37ºC (200 µl
928 infection volume). The plates were manually rocked every 15 min during the 1-hour period.
929 Subsequently, virus was removed, cells were washed and overlaying media (containing 0.6% low melt
930 agarose in DMEM with 10% FBS) was added and incubated undisturbed for 60-65h at 37ºC. Post
931 incubation, cells were fixed with 4% formaldehyde and stained with 0.25% crystal violet (prepared in

932 30% methanol). High quality plaque pictures were taken using a high resolution DLSR camera (Nikon
933 model: D80, objective: "AF Micro-Nikkor 60mm f/2.8D"). Plaques were counted manually and in
934 parallel, imaged plaque plates were processed and plaques enumerated using an automated algorithm
935 based Matlab software. Virus titer is expressed as plaque-forming units per ml (PFU/ml): (number of
936 plaques x dilution factor of the virus) x 1000 / volume of virus dilution used for infection (in µl).
937 Multiplicity of infection (MOI) expressed as: MOI = PFU of virus used for infection / number of cells.

938 **Cell infections with fully replicative SARS-CoV-2**

939 Vero E.6 and Calu-3 cells were seeded in duplicates in 12-well plates (2.3 x 10^5 cells/well) the day
940 before. Cells were pre-treated with various concentrations (0.1-1µM) of BOS inhibitors and vehicle
941 alone (DMSO) for up to 24h. In certain experiments, Calu-3 were also pre-treated with Camostat for
942 1h. Thereafter, the cells were infected with SARS-CoV-2 virus at MOI of 0.001 for 1h (Vero E6) or
943 0.01 for 3h (Calu-3 cells) in 350 µl of serum-free DMEM at 37ºC with occasional manual rocking of
944 plates. Cells plus media only were used as a control. After incubation, virus was removed, and the cell
945 monolayer was washed twice successively with PBS and serum-free DMEM. New media (total 1ml)
946 containing the concentrations of BOS-inhibitors was subsequently added to cells. Cell-free supernatant
947 (250 µl) was removed at 12, 24 and 48h post infection. The drugs were replenished for 1 ml media at
948 24h post-infection. The virus supernatants were stored at -80°C until further use. Viral production in
949 the supernatant was quantified using a plaque assay on Vero E6.1 cells as described above. In certain
950 experiments, viral supernatants were harvested at the end of infection and purified on a 20% sucrose
951 cushion using ultracentrifugation as described above. The resulting concentrated virus and
952 corresponding infected cells were analyzed by Western blotting as appropriate.

953 Quantification and statistical analysis: Virus titers quantified by plaque assay in triplicate were shown
954 as mean ± standard deviation. The results from experiments done with two biological replicates and
955 two technical replicates in triplicates were used to calculate the IC_{50} by nonlinear regression using

956 GraphPad Prism V5.0 software. The difference between the control cells (virus with 0.001% DMSO)
957 and the cells treated with BOS-inhibitors were evaluated by Student's t test. The P values of 0.05 or
958 lower were considered statistically significant (*, $p < 0.05$; **, $p < 0.01$; ***, $p < 0.001$).

959

960 **Acknowledgments**

961 This work was supported in part by CIHR Foundation grants (NGS: # 148363) and (ÉAC: # 154324),
962 a Canada Research Chairs in Precursor Proteolysis (NGS: # 950-231335), a CIHR CHAMPS Team
963 Grant # HAL 157986 (NGS and ÉAC), Réseau SIDA maladies infectieuses COVID-19 initiative (ÉAC
964 and NGS), the European score project and ANR Reacting COVID-19 (ED and BC). The authors thank
965 the Quebec public health laboratory for providing the infectious isolate LSPQ1 SARS-CoV-2. We
966 thank Paul Bieniasz for the 293T-ACE2 cell line and the pHIV-1NL4-3ΔEnv-NanoLuc construct. The
967 following reagents were obtained from the NIH AIDS Reagent Program, Division of AIDS, NIAID,
968 NIH: TZM-bl cells, from John C. Kappes, Xiaoyun Wu, and Tranzyme, Inc. and HIV-1 pNL4-3 ΔEnv
969 Vpr Luciferase Reporter Vector (pNL4-3.Luc.R-E-) obtained from Nathaniel Landau. We are thankful
970 to Dominic Filion for developing the algorithm for image-assisted plaque quantification. JJ is
971 supported by the CIHR Postdoctoral Fellowship (HIV-435243-73284). We also thank Dr Annik Prat
972 (IRCM) for the design of the summary model shown in Fig. 7. Finally, we would like to thank Mrs.
973 Brigitte Mary for her excellent editorial help and organization of the manuscript.

974 **Data availability**

975 Source data are provided with this paper. The data that support the findings of this study are preserved
976 at repositories of the Montreal Clinical Research Institute (IRCM), Montreal, QC, Canada and
977 available from the corresponding authors upon reasonable request.

978

979 **Author contributions**

980 RE made all the original critical experiments revealing the role of the PCs in Spike processing and the
981 effect of their inhibitors. JJ performed all the cell assays with infectious SARS-CoV-2. DSR
982 participated in the biochemical characterizations of TMPRSS2 processing of ACE2 and S1. UA
983 performed all cell-to-cell fusion assays. AE made all the mutants used in the work. RMD generated

984 the HeLa-ACE2 cells and prepared all the cells for *ex vivo* analyses. DNH performed all the
985 immunocytochemical experiments. FD and ML performed experiments related to SARS-CoV-2
986 pseudovirions. AD and PSO performed all the Furin and TMPRSS2 *in vitro* kinetic cleavage analyses
987 of peptides mimicking the S1/S2 and S2' sites. CM and KW provided the BOS-inhibitors and their
988 characterization. ED made seminal contributions to the possible role of Furin-like enzymes in the
989 processing of the spike glycoprotein and actively contributed to the conceptualization and writing of
990 the manuscript. TNQP designed, performed, and analyzed experiments related to viral entry and
991 contributed to the writing of the manuscript. EAC (virology) and NGS (biochemistry and cell biology)
992 conceptualized the research program and provided the intellectual contributions and funding for the
993 whole project. All authors actively contributed to the final version of the manuscript.

994

995 References

996 1. Dobson AP, Carper ER. Infectious Diseases and Human Population History: Throughout
997 history the establishment of disease has been a side effect of the growth of civilization.
998 *Bioscience*. 1996;**46**:115-26.
999 2. Cui J, Li F, Shi ZL. Origin and evolution of pathogenic coronaviruses. *Nat Rev Microbiol*.
1000 2019;**17**:181-92.
1001 3. Almeida JD, Tyrrell DA. The morphology of three previously uncharacterized human
1002 respiratory viruses that grow in organ culture. *J Gen Virol*. 1967;**1**:175-8.
1003 4. Belouzard S, Millet JK, Licitra BN, Whittaker GR. Mechanisms of coronavirus cell entry
1004 mediated by the viral spike protein. *Viruses*. 2012;**4**:1011-33.
1005 5. Liu PP, Blet A, Smyth D, Li H. The Science Underlying COVID-19: Implications for the
1006 Cardiovascular System. *Circulation*. 2020;**142**:68-78.
1007 6. Usul Afsar C. 2019-nCoV-SARS-CoV-2 (COVID-19) infection: Crucıalıty of Furın and
1008 relevance wıth cancer. *Med Hypotheses*. 2020;**140**:109770.
1009 7. Braun E, Sauter D. Furin-mediated protein processing in infectious diseases and cancer. *Clin*
1010 *Transl Immunology*. 2019;**8**:e1073.
1011 8. Izaguirre G. The Proteolytic Regulation of Virus Cell Entry by Furin and Other Proprotein
1012 Convertases. *Viruses*. 2019;**11**.
1013 9. Seidah NG, Pasquato A, Andreo U. How Do Enveloped Viruses Exploit the Secretory
1014 Proprotein Convertases to Regulate Infectivity and Spread? *Viruses*. 2021;**13**:1229.
1015 10. Coutard B, Valle C, de Lamballerie X, Canard B, Seidah NG, Decroly E. The spike
1016 glycoprotein of the new coronavirus 2019-nCoV contains a furin-like cleavage site absent in
1017 CoV of the same clade. *Antiviral Res*. 2020;**176**:104742.

1018 11. Tang T, Bidon M, Jaimes JA, Whittaker GR, Daniel S. Coronavirus membrane fusion
1019 mechanism offers as a potential target for antiviral development. *Antiviral Res*. 2020:104792.
1020 12. Hoffmann M, Kleine-Weber H, Pöhlmann S. A Multibasic Cleavage Site in the Spike Protein
1021 of SARS-CoV-2 Is Essential for Infection of Human Lung Cells. *Mol Cell*. 2020;**78**:779-84.e5.
1022 13. Lan J, Ge J, Yu J, Shan S, Zhou H, Fan S, et al. Structure of the SARS-CoV-2 spike receptor-
1023 binding domain bound to the ACE2 receptor. *Nature*. 2020;**581**:215-20.
1024 14. Lu G, Wang Q, Gao GF. Bat-to-human: spike features determining 'host jump' of coronaviruses
1025 SARS-CoV, MERS-CoV, and beyond. *Trends Microbiol*. 2015;**23**:468-78.
1026 15. Millet JK, Whittaker GR. Physiological and molecular triggers for SARS-CoV membrane
1027 fusion and entry into host cells. *Virology*. 2018;**517**:3-8.
1028 16. Ou X, Liu Y, Lei X, Li P, Mi D, Ren L, et al. Characterization of spike glycoprotein of SARS-
1029 CoV-2 on virus entry and its immune cross-reactivity with SARS-CoV. *Nat Commun*.
1030 2020;**11**:1620.
1031 17. Shang J, Wan Y, Luo C, Ye G, Geng Q, Auerbach A, et al. Cell entry mechanisms of SARS-
1032 CoV-2. *Proc Natl Acad Sci U S A*. 2020;**117**:11727-34.
1033 18. Bestle D, Heindl MR, Limburg H, Van Lam van T, Pilgram O, Moulton H, et al. TMPRSS2
1034 and furin are both essential for proteolytic activation of SARS-CoV-2 in human airway cells.
1035 *Life Sci Alliance*. 2020;**3**.
1036 19. Mykytyn AZ, Breugem TI, Riesebosch S, Schipper D, van den Doel PB, Rottier RJ, et al.
1037 SARS-CoV-2 entry into human airway organoids is serine protease-mediated and facilitated
1038 by the multibasic cleavage site. *Elife*. 2021;**10**.
1039 20. Seidah NG, Prat A. The biology and therapeutic targeting of the proprotein convertases. *Nat*
1040 *Rev Drug Discov* 2012;**11**:367-83.

1041 21. Van de Ven WJ, Creemers JW, Roebroek AJ. Furin: the prototype mammalian subtilisin-like
1042 proprotein-processing enzyme. Endoproteolytic cleavage at paired basic residues of
1043 proproteins of the eukaryotic secretory pathway. *Enzyme*. 1991;**45**:257-70.
1044 22. Moulard M, Decroly E. Maturation of HIV envelope glycoprotein precursors by cellular
1045 endoproteases. *Biochim Biophys Acta*. 2000;**1469**:121-32.
1046 23. Millet JK, Whittaker GR. Host cell proteases: Critical determinants of coronavirus tropism and
1047 pathogenesis. *Virus Res*. 2015;**202**:120-34.
1048 24. Hoffmann M, Kleine-Weber H, Schroeder S, Kruger N, Herrler T, Erichsen S, et al. SARS-
1049 CoV-2 Cell Entry Depends on ACE2 and TMPRSS2 and Is Blocked by a Clinically Proven
1050 Protease Inhibitor. *Cell*. 2020;**181**:271-80.e8.
1051 25. Xia S, Lan Q, Su S, Wang X, Xu W, Liu Z, et al. The role of furin cleavage site in SARS-CoV-
1052 2 spike protein-mediated membrane fusion in the presence or absence of trypsin. *Signal*
1053 *Transduct Target Ther*. 2020;**5**:92.
1054 26. Johnson BA, Xie X, Bailey AL, Kalveram B, Lokugamage KG, Muruato A, et al. Loss of furin
1055 cleavage site attenuates SARS-CoV-2 pathogenesis. *Nature*. 2021.
1056 27. Peacock TP, Goldhill DH, Zhou J, Baillon L, Frise R, Swann OC, et al. The furin cleavage site
1057 in the SARS-CoV-2 spike protein is required for transmission in ferrets. *Nat Microbiol*. 2021.
1058 28. Johnson BA, Xie X, Bailey AL, Kalveram B, Lokugamage KG, Muruato A, et al. Loss of furin
1059 cleavage site attenuates SARS-CoV-2 pathogenesis. *Nature*. 2021;**591**:293-99.
1060 29. Afar DE, Vivanco I, Hubert RS, Kuo J, Chen E, Saffran DC, et al. Catalytic cleavage of the
1061 androgen-regulated TMPRSS2 protease results in its secretion by prostate and prostate cancer
1062 epithelia. *Cancer Res*. 2001;**61**:1686-92.
1063 30. Shrimp JH, Kales SC, Sanderson PE, Simeonov A, Shen M, Hall MD. An Enzymatic
1064 TMPRSS2 Assay for Assessment of Clinical Candidates and Discovery of Inhibitors as
1065 Potential Treatment of COVID-19. *bioRxiv*. 2020.

1066 31. Kawase M, Shirato K, van der Hoek L, Taguchi F, Matsuyama S. Simultaneous treatment of
1067 human bronchial epithelial cells with serine and cysteine protease inhibitors prevents severe
1068 acute respiratory syndrome coronavirus entry. *J Virol*. 2012;**86**:6537-45.
1069 32. Nimishakavi S, Raymond WW, Gruenert DC, Caughey GH. Divergent Inhibitor Susceptibility
1070 among Airway Lumen-Accessible Tryptic Proteases. *PLoS One*. 2015;**10**:e0141169.
1071 33. Hörnich BF, Großkopf AK, Schlagowski S, Tenbusch M, Kleine-Weber H, Neipel F, et al.
1072 SARS-CoV-2 and SARS-CoV spike-mediated cell-cell fusion differ in the requirements for
1073 receptor expression and proteolytic activation. *J Virol*. 2021.
1074 34. Cyranoski D. Profile of a killer: the complex biology powering the coronavirus pandemic.
1075 *Nature*. 2020;**581**:22-26.
1076 35. Nickel W, Seedorf M. Unconventional mechanisms of protein transport to the cell surface of
1077 eukaryotic cells. *Annu Rev Cell Dev Biol*. 2008;**24**:287-308.
1078 36. Heurich A, Hofmann-Winkler H, Gierer S, Liepold T, Jahn O, Pöhlmann S. TMPRSS2 and
1079 ADAM17 cleave ACE2 differentially and only proteolysis by TMPRSS2 augments entry
1080 driven by the severe acute respiratory syndrome coronavirus spike protein. *J Virol*.
1081 2014;**88**:1293-307.
1082 37. Plante JA, Mitchell BM, Plante KS, Debbink K, Weaver SC, Menachery VD. The variant
1083 gambit: COVID-19's next move. *Cell Host Microbe*. 2021;**29**:508-15.
1084 38. Matoba Y, Aoki Y, Tanaka S, Yahagi K, Katsushima Y, Katsushima F, et al. HeLa-ACE2-
1085 TMPRSS2 Cells Are Useful for the Isolation of Human Coronavirus 229E. *Jpn J Infect Dis*.
1086 2016;**69**:452-4.
1087 39. Thomas G. Furin at the cutting edge: from protein traffic to embryogenesis and disease. *Nature*
1088 *Reviews Molecular Cell Biology*. 2002;**3**:753-66.

1089 40. Susan-Resiga D, Essalmani R, Hamelin J, Asselin MC, Benjannet S, Chamberland A, et al.
1090 Furin Is the Major Processing Enzyme of the Cardiac-specific Growth Factor Bone
1091 Morphogenetic Protein 10. *J Biol Chem* 2011;**286**:22785-94.
1092 41. Hallenberger S, Bosch V, Angliker H, Shaw E, Klenk HD, Garten W. Inhibition of furin-
1093 mediated cleavage activation of HIV-1 glycoprotein gp160. *Nature*. 1992;**360**:358-61.
1094 42. Peinado JR, Kacprzak MM, Leppla SH, Lindberg I. Cross-inhibition between furin and lethal
1095 factor inhibitors. *Biochem Biophys Res Commun*. 2004;**321**:601-05.
1096 43. Örd M, Faustova I, Loog M. Biochemical evidence of furin specificity and potential for
1097 phospho-regulation at Spike protein S1/S2 cleavage site in SARS-CoV2 but not in SARS-
1098 CoV1 or MERS-CoV. *bioRxiv*. 2020:2020.06.23.166900.
1099 44. Andersen KG, Rambaut A, Lipkin WI, Holmes EC, Garry RF. The proximal origin of SARS-
1100 CoV-2. *Nat Med*. 2020;**26**:450-52.
1101 45. Schjoldager KT, Clausen H. Site-specific protein O-glycosylation modulates proprotein
1102 processing - deciphering specific functions of the large polypeptide GalNAc-transferase gene
1103 family. *Biochim Biophys Acta*. 2012;**1820**:2079-94.
1104 46. Benton DJ, Wrobel AG, Xu P, Roustan C, Martin SR, Rosenthal PB, et al. Receptor binding
1105 and priming of the spike protein of SARS-CoV-2 for membrane fusion. *Nature*. 2020;**588**:327-
1106 30.
1107 47. Belouzard S, Chu VC, Whittaker GR. Activation of the SARS coronavirus spike protein via
1108 sequential proteolytic cleavage at two distinct sites. *Proc Natl Acad Sci U S A*. 2009;**106**:5871-
1109 6.
1110 48. Seidah NG, Benjannet S, Wickham L, Marcinkiewicz J, Jasmin SB, Stifani S, et al. The
1111 secretory proprotein convertase neural apoptosis-regulated convertase 1 (NARC-1): liver
1112 regeneration and neuronal differentiation. *Proc Natl Acad Sci U S A*. 2003;**100**:928-33.

1113 49. Schjoldager KT, Narimatsu Y, Joshi HJ, Clausen H. Global view of human protein
1114 glycosylation pathways and functions. *Nat Rev Mol Cell Biol*. 2020;**21**:729-49.
1115 50. Kingsley DM, Kozarsky KF, Segal M, Krieger M. Three types of low density lipoprotein
1116 receptor-deficient mutant have pleiotropic defects in the synthesis of N-linked, O-linked, and
1117 lipid-linked carbohydrate chains. *J Cell Biol*. 1986;**102**:1576-85.
1118 51. Shomron O, Nevo-Yassaf I, Aviad T, Yaffe Y, Zahavi EE, Dukhovny A, et al. COPII collar
1119 defines the boundary between ER and ER exit site and does not coat cargo containers. *J Cell*
1120 *Biol*. 2021;**220**.
1121 52. Rousselet E, Benjannet S, Hamelin J, Canuel M, Seidah NG. The Proprotein Convertase PC7:
1122 unique zymogen activation and trafficking pathways. *J Biol Chem*. 2011;**286**:2728-38.
1123 53. Aridor M, Bannykh SI, Rowe T, Balch WE. Sequential coupling between COPII and COPI
1124 vesicle coats in endoplasmic reticulum to Golgi transport. *J Cell Biol* 1995;**131**:875-93.
1125 54. Nickel W, Rabouille C. Mechanisms of regulated unconventional protein secretion. *Nature*
1126 *Reviews Molecular Cell Biology*. 2009;**10**:148-55.
1127 55. Saraste J, Prydz K. Assembly and Cellular Exit of Coronaviruses: Hijacking an
1128 Unconventional Secretory Pathway from the Pre-Golgi Intermediate Compartment via the
1129 Golgi Ribbon to the Extracellular Space. *Cells*. 2021;**10**.
1130 56. Platt EJ, Wehrly K, Kuhmann SE, Chesebro B, Kabat D. Effects of CCR5 and CD4 cell surface
1131 concentrations on infections by macrophagetropic isolates of human immunodeficiency virus
1132 type 1. *J Virol*. 1998;**72**:2855-64.
1133 57. Raghuvamsi PV, Tulsian NK, Samsudin F, Qian X, Purushotorman K, Yue G, et al. SARS-
1134 CoV-2 S protein:ACE2 interaction reveals novel allosteric targets. *Elife*. 2021;**10**.
1135 58. Zhang H, Wada J, Hida K, Tsuchiyama Y, Hiragushi K, Shikata K, et al. Collectrin, a collecting
1136 duct-specific transmembrane glycoprotein, is a novel homolog of ACE2 and is
1137 developmentally regulated in embryonic kidneys. *J Biol Chem*. 2001;**276**:17132-9.

1138 59. Yan R, Zhang Y, Li Y, Xia L, Guo Y, Zhou Q. Structural basis for the recognition of SARS-
1139 CoV-2 by full-length human ACE2. *Science*. 2020;**367**:1444-48.
1140 60. Monteil V, Kwon H, Prado P, Hagelkrüys A, Wimmer RA, Stahl M, et al. Inhibition of SARS-
1141 CoV-2 Infections in Engineered Human Tissues Using Clinical-Grade Soluble Human ACE2.
1142 *Cell*. 2020;**181**:905-13.e7.
1143 61. Peacock TP, Penrice-Randal R, Hiscox JA, Barclay WS. SARS-CoV-2 one year on: evidence
1144 for ongoing viral adaptation. *J Gen Virol*. 2021;**102**.
1145 62. Isabel S, Graña-Miraglia L, Gutierrez JM, Bundalovic-Torma C, Groves HE, Isabel MR, et al.
1146 Evolutionary and structural analyses of SARS-CoV-2 D614G spike protein mutation now
1147 documented worldwide. *Sci Rep*. 2020;**10**:14031.
1148 63. Plante JA, Liu Y, Liu J, Xia H, Johnson BA, Lokugamage KG, et al. Spike mutation D614G
1149 alters SARS-CoV-2 fitness and neutralization susceptibility. *bioRxiv*. 2020.
1150 64. Ogawa J, Zhu W, Tonnu N, Singer O, Hunter T, Ryan AL, et al. The D614G mutation in the
1151 SARS-CoV2 Spike protein increases infectivity in an ACE2 receptor dependent manner.
1152 *bioRxiv*. 2020.
1153 65. Gobeil SM, Janowska K, McDowell S, Mansouri K, Parks R, Manne K, et al. D614G Mutation
1154 Alters SARS-CoV-2 Spike Conformation and Enhances Protease Cleavage at the S1/S2
1155 Junction. *Cell Rep*. 2020:108630.
1156 66. Daniloski Z, Jordan TX, Ilmain JK, Guo X, Bhabha G, tenOever BR, et al. The Spike D614G
1157 mutation increases SARS-CoV-2 infection of multiple human cell types. *Elife*. 2021;**10**.
1158 67. Walls AC, Park YJ, Tortorici MA, Wall A, McGuire AT, Veesler D. Structure, Function, and
1159 Antigenicity of the SARS-CoV-2 Spike Glycoprotein. *Cell*. 2020;**181**:281-92.e6.
1160 68. Hoffmann M, Mösbauer K, Hofmann-Winkler H, Kaul A, Kleine-Weber H, Krüger N, et al.
1161 Chloroquine does not inhibit infection of human lung cells with SARS-CoV-2. *Nature*.
1162 2020;**585**:588-90.

1163 69. Vincent MJ, Bergeron E, Benjannet S, Erickson BR, Rollin PE, Ksiazek TG, et al. Chloroquine
1164 is a potent inhibitor of SARS coronavirus infection and spread. *Virol J*. 2005;**2**:69.
1165 70. Bayati A, Kumar R, Francis V, McPherson PS. SARS-CoV-2 infects cells following viral entry
1166 via clathrin-mediated endocytosis. *J Biol Chem*. 2021;**296**:100306.
1167 71. Hoffmann M, Mösbauer K, Hofmann-Winkler H, Kaul A, Kleine-Weber H, Krüger N, et al.
1168 Chloroquine does not inhibit infection of human lung cells with SARS-CoV-2. *Nature*. 2020.
1169 72. Cheng YW, Chao TL, Li CL, Chiu MF, Kao HC, Wang SH, et al. Furin Inhibitors Block SARS-
1170 CoV-2 Spike Protein Cleavage to Suppress Virus Production and Cytopathic Effects. *Cell Rep*.
1171 2020;**33**:108254.
1172 73. Cai Y, Zhang J, Xiao T, Peng H, Sterling SM, Walsh RM, Jr., et al. Distinct conformational
1173 states of SARS-CoV-2 spike protein. *Science*. 2020;**369**:1586-92.
1174 74. Wrobel AG, Benton DJ, Xu P, Roustan C, Martin SR, Rosenthal PB, et al. SARS-CoV-2 and
1175 bat RaTG13 spike glycoprotein structures inform on virus evolution and furin-cleavage effects.
1176 *Nat Struct Mol Biol*. 2020;**27**:763-67.
1177 75. Mayer G, Boileau G, Bendayan M. Sorting of furin in polarized epithelial and endothelial cells:
1178 expression beyond the Golgi apparatus. *J Histochem Cytochem*. 2004;**52**:567-80.
1179 76. Antalis TM, Bugge TH, Wu Q. Membrane-anchored serine proteases in health and disease.
1180 *Prog Mol Biol Transl Sci*. 2011;**99**:1-50.
1181 77. Hao S, Ning K, Kuz CA, Vorhies K, Yan Z, Qiu J. Long-Term Modeling of SARS-CoV-2
1182 Infection of In Vitro Cultured Polarized Human Airway Epithelium. *mBio*. 2020;**11**.
1183 78. Padmanabhan P, Desikan R, Dixit NM. Targeting TMPRSS2 and Cathepsin B/L together may
1184 be synergistic against SARS-CoV-2 infection. *PLoS Comput Biol*. 2020;**16**:e1008461.
1185 79. Papa G, Mallery DL, Albecka A, Welch LG, Cattin-Ortolá J, Luptak J, et al. Furin cleavage of
1186 SARS-CoV-2 Spike promotes but is not essential for infection and cell-cell fusion. *PLoS*
1187 *Pathog*. 2021;**17**:e1009246.

1188 80. Burkard C, Verheije MH, Wicht O, van Kasteren SI, van Kuppeveld FJ, Haagmans BL, et al.
1189 Coronavirus cell entry occurs through the endo-/lysosomal pathway in a proteolysis-dependent
1190 manner. *PLoS Pathog*. 2014;**10**:e1004502.
1191 81. Ou T, Mou H, Zhang L, Ojha A, Choe H, Farzan M. Hydroxychloroquine-mediated inhibition
1192 of SARS-CoV-2 entry is attenuated by TMPRSS2. *PLoS Pathog*. 2021;**17**:e1009212.
1193 82. Matsuyama S, Nagata N, Shirato K, Kawase M, Takeda M, Taguchi F. Efficient activation of
1194 the severe acute respiratory syndrome coronavirus spike protein by the transmembrane
1195 protease TMPRSS2. *J Virol*. 2010;**84**:12658-64.
1196 83. Malik YA. Properties of Coronavirus and SARS-CoV-2. *Malays J Pathol*. 2020;**42**:3-11.
1197 84. Yamamoto M, Kiso M, Sakai-Tagawa Y, Iwatsuki-Horimoto K, Imai M, Takeda M, et al. The
1198 Anticoagulant Nafamostat Potently Inhibits SARS-CoV-2 S Protein-Mediated Fusion in a Cell
1199 Fusion Assay System and Viral Infection In Vitro in a Cell-Type-Dependent Manner. *Viruses*.
1200 2020;**12**.
1201 85. Wölfel R, Corman VM, Guggemos W, Seilmaier M, Zange S, Müller MA, et al. Virological
1202 assessment of hospitalized patients with COVID-2019. *Nature*. 2020;**581**:465-69.
1203 86. Zhou L, Niu Z, Jiang X, Zhang Z, Zheng Y, Wang Z, et al. The SARS-CoV-2 targets by the
1204 pscRNA profiling of ACE2, TMPRSS2 and Furin proteases. *iScience*. 2020:101744.
1205 87. Mokhtari T, Hassani F, Ghaffari N, Ebrahimi B, Yarahmadi A, Hassanzadeh G. COVID-19
1206 and multiorgan failure: A narrative review on potential mechanisms. *J Mol Histol*.
1207 2020;**51**:613-28.
1208 88. Wei J, Alfajaro MM, DeWeirdt PC, Hanna RE, Lu-Culligan WJ, Cai WL, et al. Genome-wide
1209 CRISPR Screens Reveal Host Factors Critical for SARS-CoV-2 Infection. *Cell*. 2020.
1210 89. Chu H, Chan JF, Yuen TT, Shuai H, Yuan S, Wang Y, et al. Comparative tropism, replication
1211 kinetics, and cell damage profiling of SARS-CoV-2 and SARS-CoV with implications for

1212 clinical manifestations, transmissibility, and laboratory studies of COVID-19: an observational
1213 study. *Lancet Microbe*. 2020;**1**:e14-e23.
1214 90. Peacock TP, Goldhill DH, Zhou J, Baillon L, Frise R, Swann OC, et al. The furin cleavage site
1215 of SARS-CoV-2 spike protein is a key determinant for transmission due to enhanced
1216 replication in airway cells. *bioRxiv*. 2020:2020.09.30.318311.
1217 91. Ozden S, Lucas-Hourani M, Ceccaldi PE, Basak A, Valentine M, Benjannet S, et al. Inhibition
1218 of Chikungunya Virus Infection in Cultured Human Muscle Cells by Furin Inhibitors:
1219 Impairment of the maturation of the E2 surface glycoprotein. *J Biol Chem*. 2008;**283**:21899-
1220 908.
1221 92. Altulea D, Maassen S, Baranov MV, van den Bogaart G. What makes (hydroxy)chloroquine
1222 ineffective against COVID-19: insights from cell biology. *J Mol Cell Biol*. 2021.
1223 93. Self WH, Semler MW, Leither LM, Casey JD, Angus DC, Brower RG, et al. Effect of
1224 Hydroxychloroquine on Clinical Status at 14 Days in Hospitalized Patients With COVID-19:
1225 A Randomized Clinical Trial. *JAMA*. 2020;**324**:2165-76.
1226 94. Rosenke K, Jarvis MA, Feldmann F, Schwarz B, Okumura A, Lovaglio J, et al.
1227 Hydroxychloroquine prophylaxis and treatment is ineffective in macaque and hamster SARS-
1228 CoV-2 disease models. *JCI Insight*. 2020;**5**.
1229 95. Morens DM, Fauci AS. Emerging Pandemic Diseases: How We Got to COVID-19. *Cell*.
1230 2020;**183**:837.
1231 96. Lodge R, Lalonde JP, Lemay G, Cohen EA. The membrane-proximal intracytoplasmic tyrosine
1232 residue of HIV-1 envelope glycoprotein is critical for basolateral targeting of viral budding in
1233 MDCK cells. *EMBO J*. 1997;**16**:695-705.
1234 97. Forget J, Yao XJ, Mercier J, Cohen EA. Human immunodeficiency virus type 1 vpr protein
1235 transactivation function: mechanism and identification of domains involved. *J Mol Biol*.
1236 1998;**284**:915-23.

1237 98. Schmidt F, Weisblum Y, Muecksch F, Hoffmann HH, Michailidis E, Lorenzi JCC, et al.
1238 Measuring SARS-CoV-2 neutralizing antibody activity using pseudotyped and chimeric
1239 viruses. *J Exp Med*. 2020;**217**.

1240

1241

1242 **Figure legends**

1243 Figure 1: **Processing of S-peptides by Furin and TMPRSS2. (A)** Schematic representation of the
1244 primary structure of preproS and its domains and the predicted Furin-like S1/S2 site generating the S1-
1245 and S2-subunits, as well as the S2' site preceding the fusion peptide (FP). The signal peptide (SP), N-
1246 terminal domain (NTD), receptor binding domain (RBD) to ACE2, the two heptad repeats HR1 and
1247 HR2, the transmembrane domain (TM), the cytosolic tail (CT) and the C-terminal V5-tag are indicated.
1248 **(B)** *In vitro* Furin activity against the peptides mimicking the S1/S2 and S2' cleavage site sequence of
1249 the spike protein from SARS-CoV-2 (and its mutants) and SARS-CoV-1, described in SI-Table 1.
1250 Each substrate was tested at a final protease concentration of 2 and 100 nM (left inset) and 0.2 nM
1251 (right inset) for the α- and δ-variants at the S1/S2 site. **(C)** *In vitro* TMPRSS2 activity against the
1252 peptides mimicking the S1/S2 and S2' cleavage site sequence of the spike protein from SARS-CoV-2
1253 (and its mutants) described in SI-Table 1.

1254 Figure 2: **Processing of Spike-glycoprotein in HeLa cells.** (**A**) Western blot analyses of the
1255 processing of WT proS into V5-tagged S2 and S2' by the proprotein convertases Furin, PC5A, PACE4
1256 and PC7 following co-transfection of their cDNAs in HeLa cells. The migration positions of immature
1257 $proS_{im}$, S2 and S2', as wells the actin loading control are emphasized. V = empty pIRES-EGFP-V5
1258 vector. (**B**) Western blot analyses of HeLa cells following co-transfection with cDNAs coding for either
1259 WT-S-protein or its double Ala-mutant [R685A + R682A] (μS1/S2) in the absence or presence of cDNAs
1260 coding for Furin or TMPRSS2 at a ratio S:protease = 1:2. *Inconsistently observed oligomeric forms of
1261 proS. (**C**) Identification of S2' cleavage site by MS/MS. WT-Spike glycoprotein was
1262 immunoprecipitated from HeLa cells using V5 agarose beads then resolved by SDS electrophoresis
1263 SDS/PAGE and subjected to silver staining (left panel); the positions of the slices are indicated (1 to
1264 10). The MS/MS analysis of peptides generated by a Lys-specific protease (K_{814}↓) are indicated; the
1265 data represent the ratio of SFIEDLLFNK825 to $\underline{R}_{815}$SFIEDLLFN$\underline{K}_{825}$ (right panel). (**D**) Western blot

1266 analyses of HeLa cells co-transfected with V5-tagged spike protein, WT (S) or its Furin-optimized S2'
1267 (K<u>RR</u>KR$_{815}$↓SF) mutant (μS2'), and empty vector (V) or Furin. (**A, B**) The estimated % cleavages into
1268 S1/S2, S2', S2a and S2b are shown and were calculated as the ratio of the V5-immunoreactivity of the
1269 cleaved form to the sum of all forms. The data are representative of at least three independent
1270 experiments.

1271 Figure 3: **Processing of spike glycoprotein at S2' is enhanced in presence of ACE2.** Western blot
1272 showing the impact of ACE2 on the processing of WT and μS1/S2 spike glycoprotein by Furin and
1273 TMPRSS2. HeLa cells expressing empty vector (V), WT proS (**A**) or its μS1/S2 mutant (**B**) with or
1274 without ACE2, Furin or TMPRSS2 were analysed by Western blotting using anti-V5 antibody. The ratio
1275 of cDNAs used was S:ACE2:Furin/TMPRSS2 = 1:1:2. The data are representative of at least three
1276 independent experiments.

1277 Figure 4: **TMPRSS2-generated S2a and S2b are ER-retained non-O-glycosylated forms of S2 and**
1278 **S2'.** (**A**) Hela+ACE2 stable cells were transiently co-transfected for 48h with cDNAs coding for HA-
1279 tagged WT-Spike glycoprotein and empty vector (V) or TMPRSS2, at a ratio S:TMPRSS2 = 1:0.4..
1280 The conditioned serum-free media collected were treated with Endo-H and Endo-F or mock treated
1281 (NT) and analyzed by Western blotting using HA-HRP antibody. (**B**) CHO-K1 and CHO-ldld cells were
1282 transiently co-transfected with cDNAs coding for double tagged WT-Spike glycoprotein (N-terminal
1283 HA-tag; C-terminal V5-tag) and ACE2 together with empty vector (V) or TMPRSS2, at a ratio
1284 S:ACE2:TMPRSS2 = 1:0.6:0.4.. Cell extracts were analyzed by Western blot for spike glycoprotein
1285 (mAb-V5) and ACE2 receptor. Media were concentrated and blotted for secreted forms of spike
1286 glycoprotein (HA-HRP) (S1, S1', S1'') before (**B**) or after treatment with Endo-H and Endo-F (**C**) and
1287 for TMPRSS2-shed forms of ACE2 (sACE2) (**B**). All data are representative of two independent
1288 experiments.

1289 Figure 5: **Inhibition of PCs by BOS compounds.** (**A**) Chemical motif of BOS-inhibitors. (**B**)
1290 Representative structure of BOS-318. (**C**) *In vitro* BOS-inhibition of the cleavage of the fluorogenic
1291 dibasic substrate FAM-QRVRRAVGIDK-TAMRA by each of the proprotein convertases Furin, PC5A
1292 (PCSK5), PACE4 (PCSK6) and PC7 (PCSK7). All experiments were performed in 10 different wells
1293 and the average pIC_{50} (in nM) was calculated. Shown for comparison is the inhibitory pIC_{50} of the
1294 Furin-like inhibitor RVKR-cmk performed >100 times. Golgi assay: Last column represents the effects
1295 of BOS-inhibitors on U2OS cells expressing each of Furin, PC5A, PACE4 and PC7 simultaneously
1296 transduced with a BacMam-delivered construct containing a Golgi-targeting sequence followed by a
1297 12-amino acid Furin/PCSK cleavage site from Bone Morphogenic Protein 10 (BMP10) and then GFP
1298 at the C terminus (GalNAc-T2-GGGGS-DSTARIRR↓NAKG-GGGGS-GFP). Dibasic cleavage
1299 releases NAKG-GGGGS-GFP thereby reducing the Golgi-associated fluorescence estimated by
1300 imaging. (**D**) *In vitro* inhibition of Furin by the BOS compounds. Furin (2 nM) was incubated with
1301 increasing concentration of BOS-inhibitors, and its enzymatic activity against the synthetic peptides
1302 DABSYL/Glu-TNSP**RR**A**R**↓SVAS-EDANS (5 μM) was measured at pH 7.5 (n=3). (**E**) Furin-
1303 inhibitors (BOS) abrogate endogenous processing of the spike glycoprotein. Hela cells were transiently
1304 transfected with a cDNA encoding an empty vector (V) or with one expressing the V5-tagged spike (S)
1305 glycoprotein (Spike-V5). At 5h pre-transfection, cells were treated with vehicle DMSO (NT, duplicate)
1306 or with the Furin-inhibitors at indicated concentrations, or RVKR-cmk at 50 μM. At 24h post-
1307 transfection media were replaced with fresh ones lacking (NT) or containing the inhibitors for an
1308 additional 24h. Cell extracts were analyzed by Western blotting using a mAb-V5. All data are
1309 representative of at least three independent experiments.

1310

1311 Figure 6: **Spike-induced cell-to-cell fusion relies on Furin cleavage at S1/S2.** (**A**) Cell-to-cell fusion
1312 between donor cells (HeLa) expressing the fusogenic SARS-CoV-2 Spike protein along with the HIV

1313 trans-activator Tat, and acceptor cells (TZM-bl) that express ACE2. Upon fusion, Tat is transferred
1314 from donor to acceptor cells, thereby inducing luciferase expression. (**B**) Donor cells were transfected
1315 with vectors expressing either no protein (empty vector, V), μS1/S2, or WT-Spike (S) in the absence
1316 (S) or presence of vehicle (S-DMSO) or with the Furin-inhibitors BOS-318, BOS-981, BOS-857 (300
1317 nM) or RVKR (10 μM). Acceptor cells were transfected with a vector expressing ACE2. After 48h,
1318 donor and acceptor cells were co-cultured for 18h. Relative luminescence units (RLU) were normalized
1319 to the V value arbitrarily set to 1. Data are presented as mean values ± SD (n=3), One-Way ANOVA,
1320 Dunn-Sidàk multiple comparison test. (**C**) Donor HeLa cells were co-transfected with vectors (1:1
1321 ratio) expressing WT-Spike, μS1/S2 with (empty vector, V) or TMPRSS2. Acceptor TZM-bl cells
1322 were transfected with ACE2. After 48h, HeLa and TZM-bl were co-cultured for 18h and luciferase
1323 activity measured. The fusion is represented as ratio between the RLU measured for each condition
1324 and the RLU measured in the co-culture between donor cells transfected with V and ACE2 acceptor
1325 cells. Data are presented as mean values ± SD (n=3), One-Way ANOVA, Bonferroni multiple
1326 comparison test. (**D**) Donor HeLa cells expressing WT-S or μS1/S2 or μS2' were co-cultured with
1327 acceptor TZM-bl cells expressing (ratio of Spike WT or mut 1:ACE2 0.5: TMPRSS2 0.4): (empty
1328 vector, V), ACE2 + V, ACE2 + TMPRSS2 or TMPRSS2 + V. The extent of fusion is represented as a
1329 ratio between the RLU measured for each condition and that of donor cells expressing V. The bar graph
1330 represents the average of 3 experiments performed in triplicates. Data are presented as mean values ±
1331 SD (n=3), One-way Anova Bonferroni multiple comparison test. Two-Way ANOVA, Dunn-Sidàk
1332 multiple comparison test.

1333 Figure 7: **Spike glycoprotein processing by Furin, TMPRSS2 in co-culture system and their role**
1334 **in cell-to-cell fusion.** Donor HeLa cells expressing WT-S-HA or μS1/S2-HA were co-cultured with
1335 acceptor TZM-bl cells expressing (empty vector, V), ACE2 + V, ACE2 + TMPRSS2 or TMPRSS2 +
1336 V. From the same experiment, cell-to-cell fusion (**A**) was assessed in parallel with Spike processing in
1337 cells and media by Western blotting (**B**). (**B**) Spike glycoproteins in the cell extracts were analyzed by

1338 Western blotting using an anti-V5 mAb. Secreted forms of spike protein (S1) in the media were
1339 detected with anti HA-HRP upon immunoprecipitation with anti-HA agarose. The bar graph shows
1340 one representative fusion assay done un duplicate. The corresponding Western-blot is representative
1341 of three independent experiments.

1342 Figure 8: **Exogenous TMPRSS2-generated shedding of ACE2 differentially regulates S-induced**
1343 **fusion at the plasma membrane of WT-S *versus* µAS1/S2.** Donor HeLa cells expressing double tagged
1344 (N-terminal HA-tag; C-terminal V5-tag) spike glycoprotein WT (S) or its S1/S2 mutant (µAS1/S2) were
1345 co-cultured with acceptor TZM-bl cells expressing (empty vector, V), ACE2 + V, ACE2 + TMPRSS2
1346 or TMPRSS2 + V and treated with DMSO (vehicle control) or Camostat (120µM). Within the same
1347 experiment, cell-to-cell fusion (**A**) was assessed in parallel with Spike processing in cells and media
1348 by Western-blot (**B, C**). (**A**) The extent of fusion is represented as a ratio between the RLU measured
1349 for each condition and that of donor cells expressing V. The bar graph represents the average of 2
1350 experiments performed in triplicates. (**B, C**). Western blot analyses of media and cell extracts of the co-
1351 cultured cells with donor cells overexpressing double tagged (N-terminal HA-tag; C-terminal V5-tag) spike
1352 glycoprotein, WT (S) (**B**) or µAS1/S2 (**C**). Media were subjected to immunoprecipitation with either anti-
1353 HA agarose for the secreted forms of spike protein (S1, S1L), or with anti-ACE2 for the exogenous
1354 TMPRSS2-generated shed ACE2 forms (sACE2) followed by Western blotting with anti HA-HRP or anti-
1355 ACE2, respectively. Spike glycoproteins in the cell extracts were immunoblotted with anti-V5 mAb. The
1356 data are representative of three independent experiments.

1357 Figure 9: **The C-terminal collectrin-like domain of ACE2 may be critical for the regulation of**
1358 **cell-to-cell fusion of spike-glycoprotein when exogenous TMPRSS2 is present.** (**A**) Schematic
1359 representation of the primary structure of human ACE2 with emphasis on the C-terminal collectrin-
1360 like domain (aa 612-716), TMPRSS2/TMPRSS11D cleavage region (aa 697-716) and the polybasic
1361 amino-acid segments in which K/R were mutated to A (C0 and C4). (**B**) HeLa cells were co-transfected

1362 with ACE2, WT (ACE2) or its mutants ACE2 (C0), ACE2 (C4), ACE2 (C0+C4) and TMPRSS2, WT
1363 (TMPRSS2) or its S441A active-site mutant (µTMPRSS2), or empty vector (V). Media and cell
1364 extracts were analyzed by western blotting for shed ACE2 (sACE2) and ACE2, respectively. (**C**)
1365 Donor HeLa cells expressing WT-S-HA or µAS1/S2-HA were co-cultured with acceptor TZM-bl cells
1366 expressing ACE2, WT (ACE2) or its mutant ACE2 (C0+C4) in presence or absence of TMPRSS2.
1367 From the same experiment, cell-to-cell fusion (**C**) was assessed in parallel with WB analyses of cells
1368 and media (**D**). The extent of fusion is represented as a ratio between the RLU measured for each
1369 condition and that of donor cells expressing an empty vector. The bar graph represents the average of
1370 3 experiments performed in triplicates. Data are presented as mean values ± SD (n=3), One-way Anova
1371 Turkey's multiple comparison test. (**D**) Co-culture media were subjected to immunoprecipitation with
1372 anti-HA agarose for the secreted forms of spike protein (S1) followed by western blot with anti HA-
1373 HRP. Spike glycoproteins in the cell extracts were immunoblotted with anti-V5 mAb. The Western
1374 blot data are representative of three independent experiments.

1375 Figure 10: **Processing of SARS-CoV-2 S by Furin-like convertases and TMPRSS2 is critical for**
1376 **viral entry in human lung epithelial cells but not in model HEK 293 cells stably expressing ACE2**.
1377 (**A**) Furin cleavage of proS at the S1/S2 site is required for SARS-CoV-2 pseudoviral entry in Calu-3
1378 cells but not HEK293T-ACE2 cells. Cells were inoculated with nanoluciferase-expressing HIV
1379 particles pseudotyped with SARS-CoV-2: wild-type Spike (WT), double Ala-mutant spike (µS1/S2)
1380 or Furin-optimized Spike (µS2'). (**B**) Western blot analyses show inhibition by BOS-318 of proS
1381 processing at S1/S2 site. Purified pseudovirions and cellular extracts of producing HEK293-T17 cells
1382 treated or not with BOS-318 inhibitor were separated on SDS-PAGE gel and analyzed for HIV-1 p24
1383 and V5-tagged S-protein (proSm or cleaved, S2) as indicated. (**C**) Inhibition of proS processing at
1384 S1/S2 by a novel Furin-like inhibitor (BOS-318) during pseudovirion packaging prevents viral entry
1385 in Calu-3 cells but not in HEK293T-ACE2 cells. (**D**) Pre-treatment of Calu-3 cells with BOS-318 (B),
1386 Camostat (C) or both (B+C) markedly reduces viral entry. Calu-3 cells were transduced with

1387 nanoluciferase-expressing HIV particles pseudotyped with SARS-CoV-2 S WT, μS1/S2 or μS2' for
1388 72h and subjected to nano-luciferase activity assay. Viral entry was expressed as fold increase over
1389 that given by ball particles (pseudovirions made in the absence of S). Each dot represents a different
1390 experiment with median luciferase activity calculated from three biological replicates. Two to four
1391 experiments were performed for each cell type. Error bars indicate standard deviation (SD) from the
1392 mean.

1393 Figure 11: **Furin-like inhibitors and Camostat treatment decrease SARS-CoV-2 infection in Calu-**
1394 **3 Cells.** (**A**) Replication kinetics was studied at 12, 24 and 48h post-infection by plaque assay to
1395 determine PFUs of SARS-CoV-2 virus in the supernatant of infected Calu-3 cells treated or not with
1396 1μM BOS-318, BOS-857 and BOS-981. A line graph represents results of the triplicate plaque assay
1397 results (mean ± SD). (**B**) The virus titers (PFU per milliliter) released in the supernatant (24h post-
1398 infection) of infected Calu-3 cells treated with indicated concentrations of BOS-318 were determined
1399 by plaque assay (mean ± SD of triplicates, *$p < 0.05$; **$p < 0.01$; ***$p < 0.001$) (left panel). The
1400 selectivity index (SI) of BOS-318 in Calu-3 cells as shown in top right panel was determined by
1401 CC_{50}/IC_{50}. The left y axis indicates the inhibition of virus titer (percent) relative to that of the untreated
1402 control group (red). The right y axis indicates the cell viability (percent) relative to that of the untreated
1403 control group (green). The CC_{50} (50% cytotoxic concentration), IC_{50} (half maximal inhibitory
1404 concentration), and SI (selectivity index) values for each inhibitor are as shown. Representative plaque
1405 images of infected Calu-3 cells treated with indicated doses of BOS-inhibitors are shown in the bottom
1406 right panel. (**C**) Immunoblots for the infected Calu-3 cells (right panel) and viral particles secreted in
1407 the supernatant (left panel) with and without treatment with BOS-inhibitors indicate reduced viral
1408 protein levels. Immunoblots were probed for the full-length (proSm) and cleaved (S2) fragments of
1409 viral S protein and nucleocapsid (N) protein as indicated; β-Actin was included as the loading control
1410 for the cells. (**D**) The virus titers (PFU per milliliter) released in the supernatant (24h post-infection)

1411 of infected Calu-3 cells treated with BOS-981 and/or Camostat (Camo) were determined by plaque
1412 assay (mean ± SD of duplicates, *, $p < 0.05$; **, $p < 0.01$; ***, $p < 0.001$) (top panel). Representative
1413 plaque images of infected Calu-3 cells are shown in the bottom panel.

1414 Figure 12: **Proposed model for the processing of S-protein and its blockade by Furin and**
1415 **TMPRSS2 inhibitors.** Boxed left panel: schematic representation of the S-glycoprotein domains of
1416 SARS-CoV-2, including the N-terminal (NTD) and C-terminal (CTD) domains of S1, the Furin-S1/S2
1417 and S2' and the TMPRSS2 S1' processing sites and the fusogenic α-helix that follows S2'. Binding of
1418 the RBD domain of S1 to the membrane associated ACE2 in target cells, and the cell surface expression
1419 of TMPRSS2 and Furin are also schematized. Right panels: (**1**) Viral infection is favored by the
1420 presence of a Furin-like sites at S1/S2 and S2'. Physiological limiting amounts of TMPRSS2 in
1421 acceptor cells enhance infection by cleavage at S2' and shedding of small amounts of ACE2 into
1422 soluble sACE2 that may help the separation of sACE2-S1 complex from S2 and expose the S2' site
1423 for cleavage and fusion. However, high concentrations of TMPRSS2 may result in increased levels of
1424 sACE2 that could now act as a decoy inhibitor resulting in decreased fusion. Optimal blockade of viral
1425 infection is achieved by a combination of Furin (BOS) and TMPRSS2 (Camostat) inhibitors. (**2**) In
1426 absence of a Furin-like site at S1/S2 (μS1/S2), the uncleaved S-protein can fuse with acceptor cells
1427 expressing ACE2 and enter certain cells (e.g., HEK293 or Vero E6) by an endosomal pH-dependent
1428 pathway, inhibitable by alkalinizing agents such as Chloroquine.

1429

1430

1431

1432

1433

1434 **Supporting Information (SI): Table 1; SI Figures 1-13**

1435

1436 Table 1: Sequences of the different peptides mimicking the Cov spike cleavage sites that have been
1437 tested in the enzymatic assay. The arrow indicates the expected cleavage site.

1438

1439 SI-Figure 1: **Endo-F and Endo-H sensitivity of V5-tagged proS and its cleavage products by Furin**
1440 **and TMPRSS2 in HeLa cells.** Western blotting (V5-mAb) of protein extracts from HeLa cells
1441 transiently expressing: (**A**) empty vector (V), V5-tagged wild type Spike protein (WT) or its S1/S2 site
1442 mutant (μS1/S2) were treated with Endo-F and Endo-H or mock treated (NT); (**B**) Spike-protein WT
1443 alone or in combination with Furin or TMPRSS2 in the absence (NT) or presence of the PC inhibitors
1444 RVKR (50 μM) or D6R (20 μM); (**C**) HeLa cells transfected with control non-targeting siRNA (siCTL)
1445 or siRNA Furin (siFur) at final concentrations of 20 nM, 24h later, the cells were transfected with
1446 empty vector (V) or with that coding for a V5-tagged Spike glycoprotein. At 48h post-transfection, the
1447 proteins were resolved on SDS-PAGE followed by Western with anti-V5 and anti-Furin antibodies.;
1448 (**D**) Spike protein, WT or S1/S2 single mutants alone or in combination with TMPRSS2. All blots are
1449 representative of at least three different experiments.

1450

1451 SI-Figure 2: **S2' sites mutations block the proS in the endoplasmic reticulum.** HeLa cells were
1452 transiently transfected with cDNAs encoding either empty vector (V), V5-tagged S-protein or its
1453 double (**A**) and simple (**B**) S2' site mutants alone or in combination with Furin or human TMPRSS2.
1454 The protein extract were analyzed by Western blotting using a V5-mAb. The R995A (*) mutant was
1455 used as a control.

1456

1457 SI-Figure 3: **When co-expressed with spike protein, active TMPRSS2 cleaves proS into ER-**
1458 **retained fragments which results in secretion of S1'.** (**A**) Protein extracts from HeLa cells transiently
1459 co-expressing V5-tagged spike protein and TMPRSS2 were treated with Endo-F and Endo-H or mock
1460 treated (NT) and analyzed by Western blotting using a V5-mAb. (**B**) HeLa cells were transiently co-
1461 expressed with double-tagged spike protein (N-terminal HA-tag; C-terminal V5-tag), WT (S) or its
1462 mutants, μS1/S2 or μAS1/S2, and ACE2 alone or in combination with TMPRSS2, WT (TMPRSS2)
1463 or its S441A active-mutant (μTMPRSS2), at a ratio S:ACE2:TMPRSS2 = 1:0.5:0.5. Immunoblot of the
1464 24h conditioned media was first probed for secreted S1, S1' and S1L (HA-HRP antibody), stripped
1465 and next probed for shed ACE2 (sACE2). Cell lysates were immunoblotted for spike protein (V5-
1466 mAb), ACE2, and β-Actin.

1467

1468 SI-Figure 4: **Identification of S2a and S2b cleavage sites by MS/MS.** WT-Spike glycoprotein was
1469 transiently co-expressed with human TMPRSS2 in HeLa cells. The proS and its cleavage products
1470 were immunoprecipitated using V5 agarose beads and resolved by SDS/PAGE. The silver staining
1471 (middle panel) shows the positions of the slices in the S2a (1 to 9) and S2b (10 to 17) regions that were
1472 analyzed. The MS/MS analyses of peptides generated by the chymotrypsin protease (R685↓, left panel)
1473 or Lys-specific protease (K814↓, right panel) are indicated. The data represent the intensity of
1474 SVAQSIIAY peptide (left panel) and the ratio of SFIEDLLFNK825 to R815SFIEDLLFNK825
1475 peptides (right panel) generated by the chymotrypsin and Lys-specific proteases digestion respectively.

1476

1477 SI-Figure 5: **In HeLa cells, TMPRSS2-dependent secretion of S1' from the ER primarily occurs**
1478 ***via* a COP-II-dependent unconventional pathway that bypasses the Golgi stacks. The S1' secretion**
1479 **and ACE2 shedding by TMPRSS2 are inhibited by Camostat.** (**A**) HeLa-ACE2 cells were transiently
1480 transfected with CDNAs encoding empty vector (V) or with increasing cDNA ratios of V5-tagged WT-
1481 Spike protein to TMPRSS2 (spike-V5:TMPRSS2) as indicated and 24h later incubated for an

1482 additional 24h in serum-free media containing 120 μM Camostat (+) or control DMSO (-). Immunoblot
1483 of the 24h conditioned media (concentrated 10-fold) was first probed for S1 and S1' using an antibody
1484 against S1-subunit (GTX135356), stripped and next probed for sACE2 (ab108252) and mature
1485 $TMPRSS2_m$ (14437-1-AP) (upper panel). Cell lysates were immunoblotted for spike protein (V5-
1486 mAb), ACE2 (ab108252) and β-Actin (lower panel). Note that 120 μM Camostat was not sufficient to
1487 fully inhibit the higher levels of TMPRSS2. (**B**) HeLa cells were transiently transfected for 48h with
1488 cDNAs encoding empty vector (V) or ACE2 alone or co-transfected with cDNAs encoding double-
1489 tagged spike protein (HA-S-V5) and TMPRSS2 or Sar1p-H79G (a dominant negative mutant that would
1490 disrupt the COP-II complex) alone or a combination of the two (TMPRSS2+Sar1p-H79G). The cDNA
1491 ratio was S:ACE2:TMPRSS2:Sar1p-H79G = 1:0.5:0.75:0.75. Immunoblot of the 24h conditioned
1492 serum-free media was first probed for secreted S1 and S1' (HA-HRP antibody), stripped and next
1493 probed for shed ACE2 (sACE2). Cell lysates were immunoblotted for spike protein (V5-mAb), ACE2,
1494 and β-Actin. Data are representative of three independent experiments.
1495
1496 SI-Figure 6: **BOS-inhibitors do not affect the generation of S2a and S2b by TMPRSS2.** HeLa cells
1497 were transiently transfected with cDNAs encoding either empty vector, V5-tagged S-protein alone or in
1498 combination with human TMPRSS2. At 5h pre-transfection, during transfection and for 48h post-
1499 transfection, cells were treated with vehicle DMSO (NT) or with the Furin inhibitors (BOS) at indicated
1500 concentrations. At 48h post-transfection the cells were collected, and their protein extracts were analyzed
1501 by Western blotting using a mAb-V5.
1502
1503 SI-Figure 7: **Immunocytochemistry of the co-localization of ACE2 and S-protein or μS1/S2 in**
1504 **HeLa cells.** (**A**) Immunofluorescence of S-protein (green), WT (S) (a,b) and μS1/S2 (c,d) were
1505 revealed using the spike S2-antibody GTX632604 in non-permeabilized (NP) conditions or with anti-
1506 V5 in permeabilized (P) conditions. (**B**) Immunofluorescence of S-protein (green), WT (S) (a,b) and

1507 μS1/S2 in HeLa cells pre-incubated for 5h before transfection and then for 24h with 1 μM BOS-981.
1508 The confocal localizations were revealed as in (**A**). Scale bar = 10 μm.
1509
1510 SI-Figure 8: **Cell-to-cell fusion assay: correlation between syncytia formation and luciferase**
1511 **activity.** (**A**) Cell-to-cell fusion between donor cells (HeLa) and acceptor cells (TZM-bl) was evaluated
1512 using confocal microscopy. Hela cells transfected with an empty vector (EV), or expressing HIV-
1513 gp160, SARS-CoV-2 Spike, or μS1/S2 were co-cultured with TZM-bl cells for 18h and the number of
1514 syncytia was examined using CellMask™ to probe for the plasma membrane and Dapi to stain the
1515 nuclei. (**B)** Donor cells were transfected with increasing amount of plasmid expressing WT-Spike and
1516 acceptor cells were transfected with a vector expressing ACE2. After 48h, cells were co-cultured for
1517 18h, and prepared for luminescence or microscopy. Correlation between the number of syncytia
1518 counted by microscopy (n=10 per condition) and the luciferase activity was determined, and the
1519 correlation coefficient was calculated as shown. R^2=0.87. (**C)** Donor cells were transfected with vectors
1520 expressing either no protein (EV), Tat, WT-Spike (S), Tat and WT-Spike (Tat + S) or Tat and HIV-
1521 gp160 (Tat + gp160). Acceptor cells were transfected with a vector expressing no protein (EV), with
1522 ACE2 or directly with Tat as appositive control. After 48h, cells were co-cultured for 18h.
1523 Luminescence was normalized to the EV value arbitrarily set to 1. Data are presented as mean values
1524 ± SD (n=3) and a representative experiment is shown.
1525
1526 SI-Figure 9: **Furin processing of SARS-CoV-2 variants and their cell-to-cell fusion activity.** (**A**)
1527 Western blot analyses of HeLa cells following co-transfection with cDNAs encoding ACE2 and V5-
1528 tagged spike protein, WT (S) or its indicated relevant single or combined mutants found in circulating
1529 variants, or empty vector (V). The cDNA ratio was S:ACE2 = 1:0.5.The estimated % cleavages into
1530 S2 and S2'are shown and were calculated based on the ratio of the V5-immunoreactivity of each form
1531 to the sum of the two. Immunoblot of the secreted S1 form (using an antibody against S1-subunit,

1532 GTX135356) in the media is also shown. The data are representative of two independent experiments.
1533 (**B**, **C**) Donor HeLa cells expressing WT-S or its indicated relevant single mutants (**B**) or combined
1534 mutants found in circulating variants (**C**) were co-cultured with acceptor TZM-bl cells expressing
1535 ACE2. The extent of fusion is represented as a ratio between the RLU measured for each condition
1536 and that of donor cells expressing empty vector. The bar graph represents the average of 3 experiments
1537 performed in triplicates. Data are presented as mean values ± SEM (n=3), One way Anova Dunnett's
1538 multiple comparison test.

1539

1540 SI-Figure 10: **SARS-CoV-2 viral entry in HEK293 cells is primarily mediated via a pH-dependent**
1541 **pathway.** HEK293T-ACE2 cells were pre-treated with chloroquine (CLQ; 100 μM) for 2h and
1542 subsequently inoculated with luciferase-expressing HIV particles pseudotyped with SARS-CoV-2
1543 spike protein (S), wild-type (WT-S) or its mutant (μS1/S2 S). HIV particles made in the absence of S
1544 (no S) served as a negative control. Efficiency of viral entry was determined by luciferase activity.
1545 Each dot represents an independent experiment (median luciferase of biological triplicates). Error bars
1546 show SD.

1547

1548 SI-Figure 11: **Furin-like inhibitors strongly reduce SARS-CoV-2 infection in Calu-3 cells.** Calu-3
1549 cells were treated with indicated concentrations of (**A**) BOS-857 and (**B**) BOS-981 and infected with
1550 SARS-CoV-2 for 24h. Virus titers in the supernatant were determined by plaque assay on VeroE6 cells
1551 (mean plaque forming units [PFU] per ml) ± SD of triplicates, $^{*}p < 0.05$; $^{**}p < 0.01$; $^{***}p < 0.001$). The
1552 selectivity index (SI) of (**A**) BOS-857, and (**B**) BOS-981 in Calu-3 cells as shown in top right panel
1553 was determined by CC_{50}/IC_{50}. The left y axis indicates the inhibition of virus titer (percent) relative to
1554 that of the untreated control group (red). The right y axis indicates the cell viability (percent) relative

1555 to that of the untreated control group (green). Representative plaque images of infected Calu-3 cells
1556 treated with indicated doses of BOS inhibitors are shown in the bottom right panel.
1557
1558 SI-Figure 12: **Combination of BOS-318 and Camostat reduces SARS-CoV-2 replication.** Calu-3
1559 cells were treated with BOS-318 and/or Camostat (Camo) and infected with SARS-CoV-2 for 24h.
1560 Virus titers in the supernatant were determined by plaque assay on VeroE6 (mean PFU/ml ± SD of
1561 duplicates, $^{*}p < 0.05$. Representative plaque images of infected Calu-3 cells are shown in the bottom
1562 panel.
1563
1564 SI-Figure 13: **Furin-like inhibitors modestly reduce virus production in SARS-CoV-2-infected**
1565 **Vero E6 cells in a concentration-dependent manner. (A)** Vero E6 cells treated or not with 1μM
1566 BOS-318, BOS-857 or BOS-981 were infected with SARS-CoV-2 for up to 45h. Virus titers in the
1567 supernatant obtained at 12, 24 and 48 h post infection were determined by plaque assay on Vero E6.
1568 A line graph represents results of the triplicate plaque assay (mean PFU/ml ± SD). **(B, C, and D)** Virus
1569 released in the supernatant (48 hr post infection) of infected Vero E6 cells treated with indicated
1570 concentrations of (B) BOS-318, (C) BOS-857, or (D) BOS-981 were determined by plaque assay
1571 (mean ± SD of triplicates, $*p < 0.05$; $**p < 0.01$; $***p < 0.001$).

Figure 1

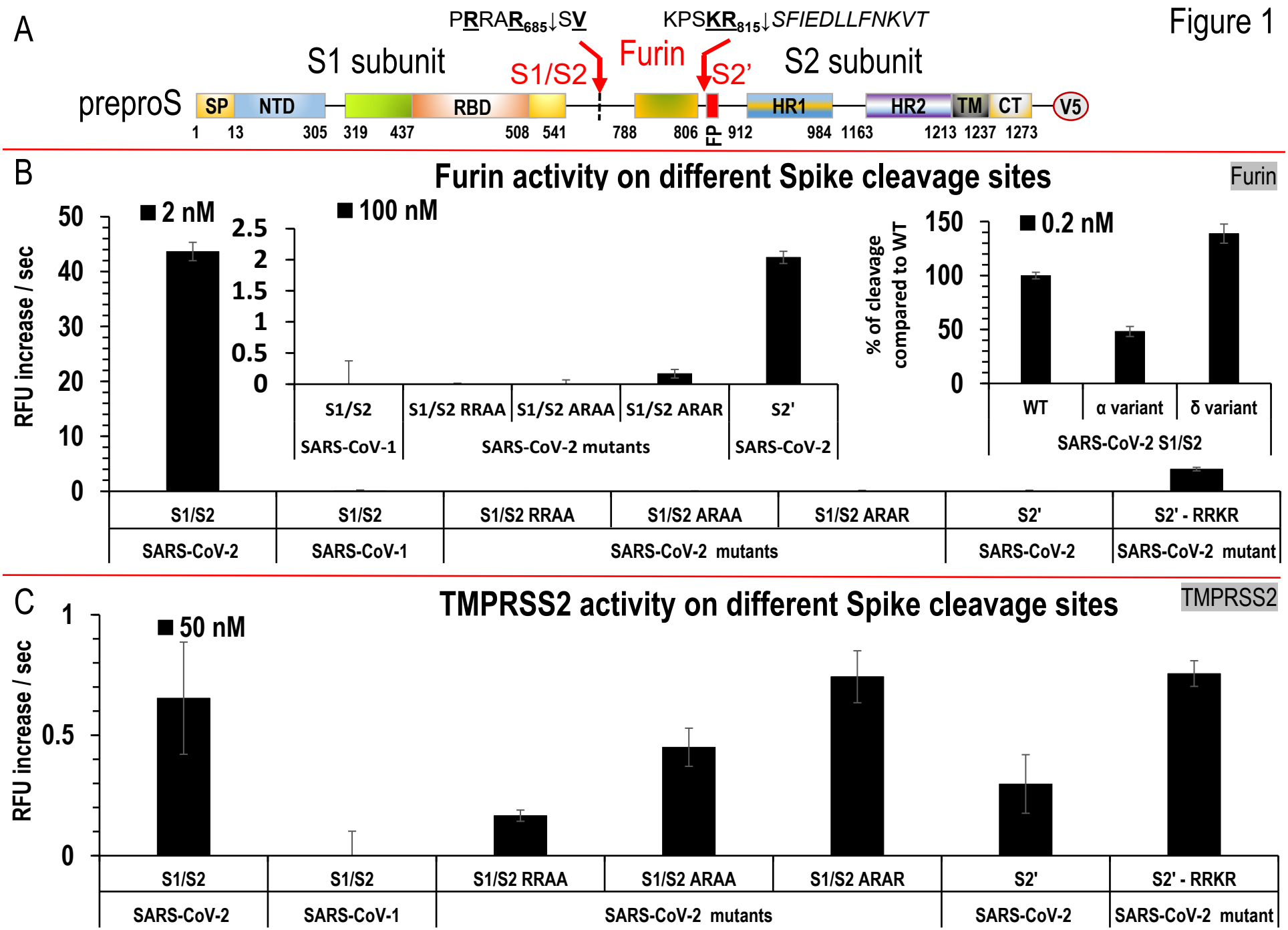
A
PRRAR685↓SV
KPSKR815↓SFIEDLLFNKVT
S1 subunit
S1/S2
Furin
S2'
S2 subunit
preproS
SP
NTD
RBD
HR1
HR2
TM
CT
V5
1
13
305
319
437
508
541
788
806
FP
912
984
1163
1213
1237
1273
B
Furin activity on different Spike cleavage sites
Furin
RFU increase / sec
2 nM
100 nM
0.2 nM
% of cleavage compared to WT
S1/S2
S1/S2 RRAA
S1/S2 ARAA
S1/S2 ARAR
S2'
S2' - RRKR
SARS-CoV-1
SARS-CoV-2 mutants
SARS-CoV-2
WT
α variant
δ variant
SARS-CoV-2 S1/S2
SARS-CoV-2 mutant
C
TMPRSS2 activity on different Spike cleavage sites
TMPRSS2
RFU increase / sec
50 nM

Figure 2

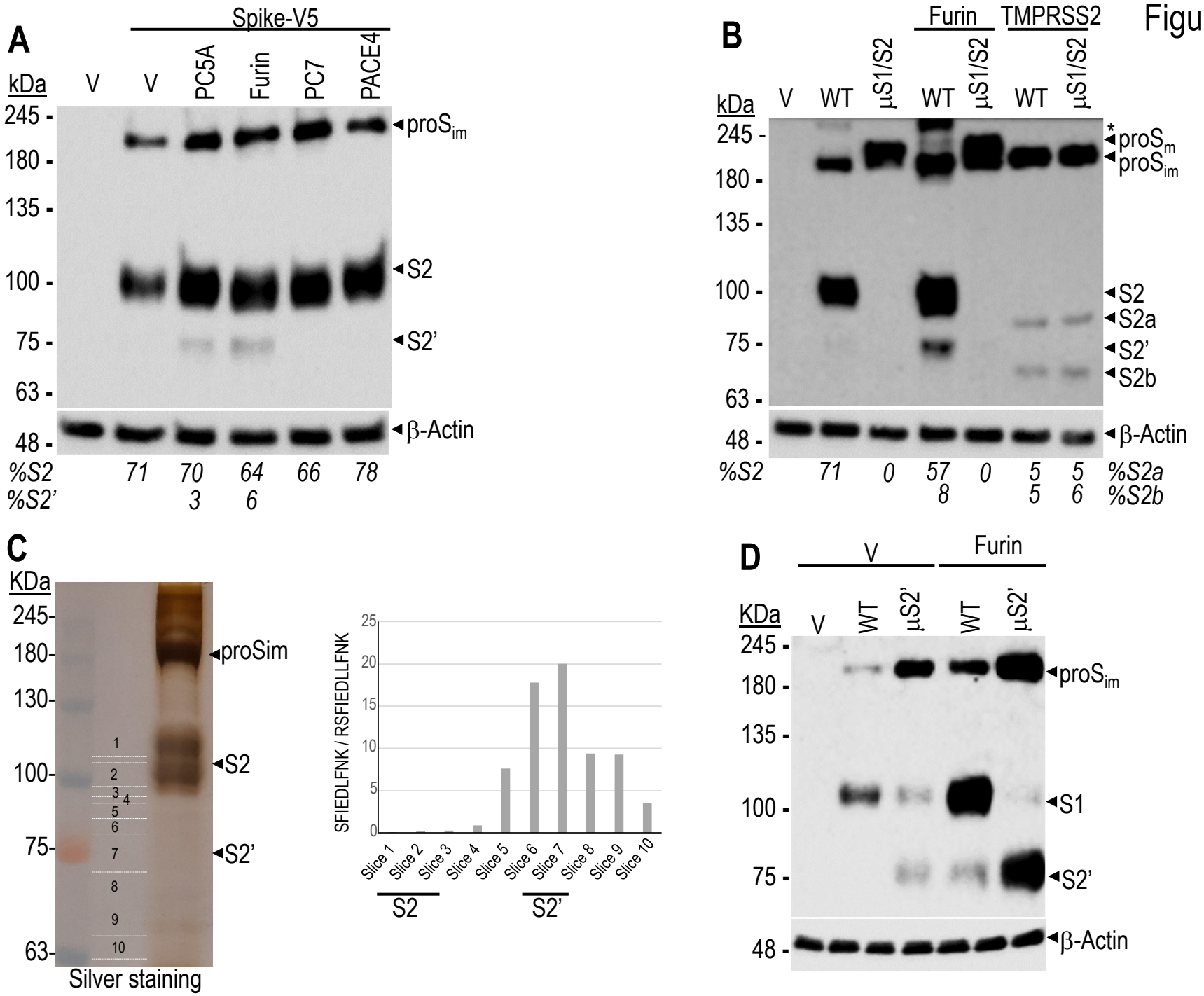
A
Spike-V5
kDa
V
V
PC5A
Furin
PC7
PACE4
245
180
135
100
75
63
48
proSim
S2
S2'
β-Actin
%S2
71
70
64
66
78
%S2'
3
6
B
Furin
TMPRSS2
kDa
V
WT
μS1/S2
WT
μS1/S2
WT
μS1/S2
245
180
135
100
75
63
48
*
proSm
proSim
S2
S2a
S2'
S2b
β-Actin
%S2
71
0
57
8
0
5
5
5
6
%S2a
%S2b
C
KDa
245
180
130
100
75
63
proSim
S2
S2'
1
2
3
4
5
6
7
8
9
10
Silver staining
SFIEDLFNK / RSFIEDLLFNK
25
20
15
10
5
0
Slice 1
Slice 2
Slice 3
Slice 4
Slice 5
Slice 6
Slice 7
Slice 8
Slice 9
Slice 10
S2
S2'
D
V
Furin
KDa
V
WT
μS2'
WT
μS2'
245
180
135
100
75
48
proSim
S1
S2'
β-Actin

Figure 3

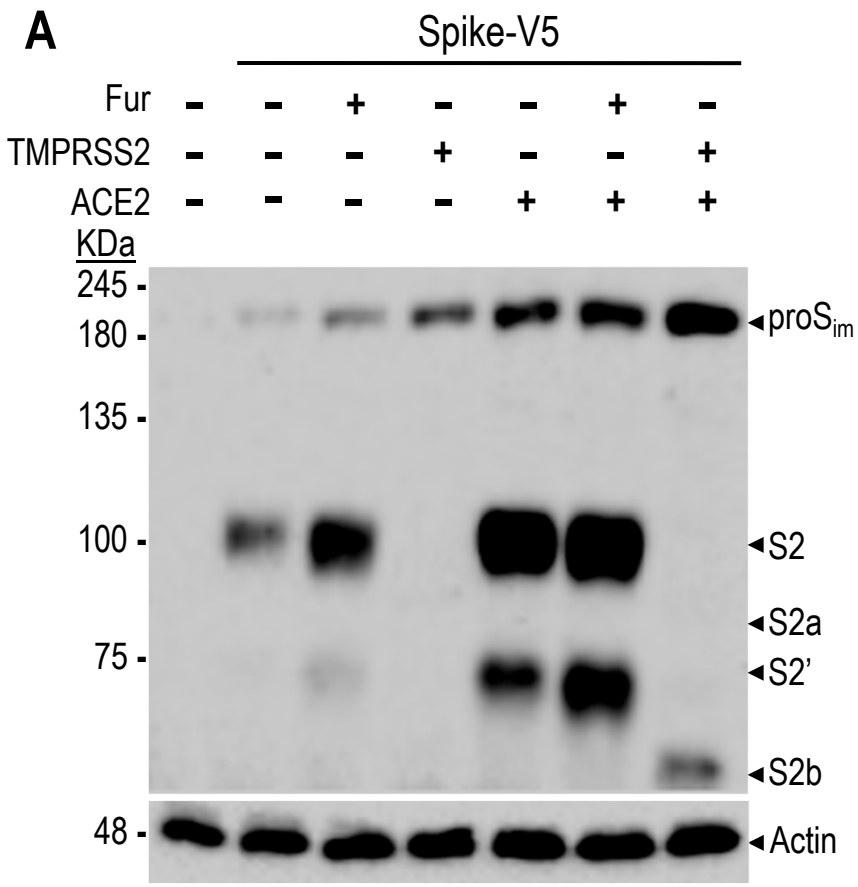
A
Spike-V5
Fur
TMPRSS2
ACE2
KDa
245
180
135
100
75
48
proS$_{im}$
S2
S2a
S2'
S2b
Actin

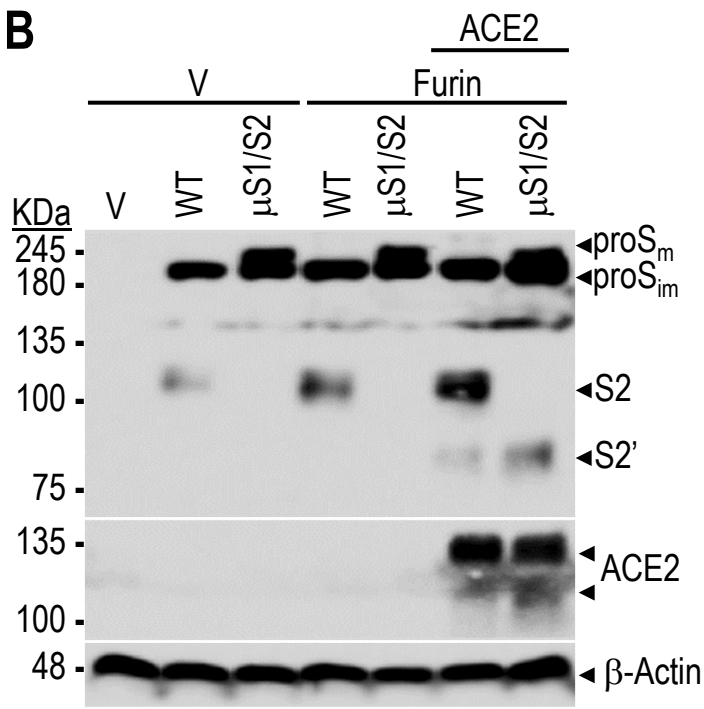
B
ACE2
V
Furin
KDa
V
WT
µS1/S2
WT
µS1/S2
WT
µS1/S2
245
180
135
100
75
135
100
48
proS$_m$
proS$_{im}$
S2
S2'
ACE2
β-Actin

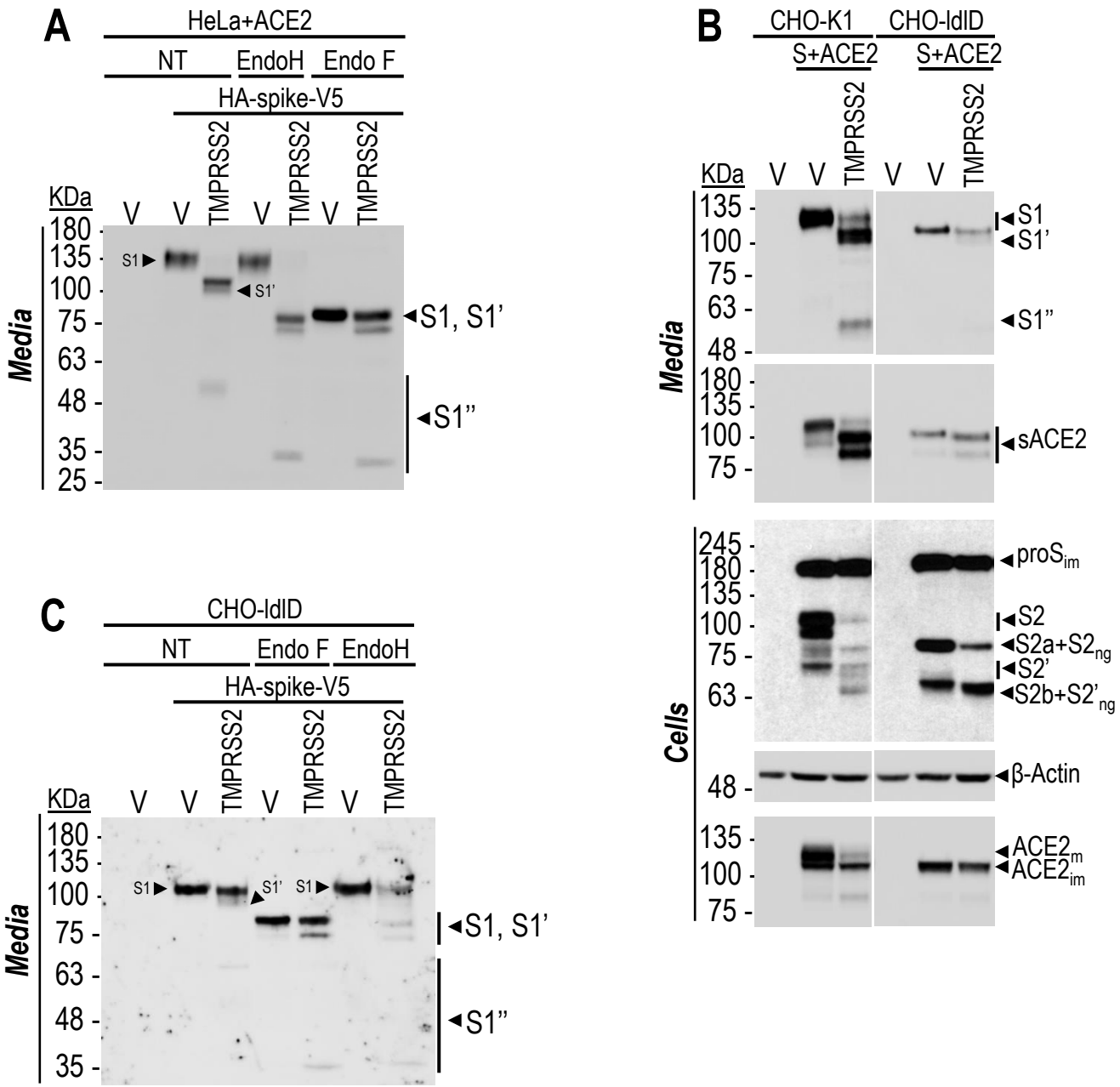
A
HeLa+ACE2
NT
EndoH
Endo F
HA-spike-V5
TMPRSS2
KDa
V
Media
180
135
100
75
63
48
35
25
S1
S1'
S1, S1'
S1"
B
CHO-K1
CHO-IdlD
S+ACE2
Media
S1
S1'
S1"
sACE2
Cells
245
proS$_{im}$
S2
S2a+S2$_{ng}$
S2'
S2b+S2'$_{ng}$
β-Actin
ACE2$_{m}$
ACE2$_{im}$
C
CHO-IdlD
NT
Endo F
EndoH

Figure 4

A

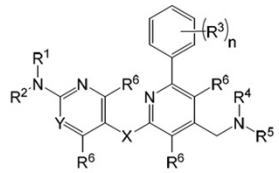

Structure of Furin inhibitors

B

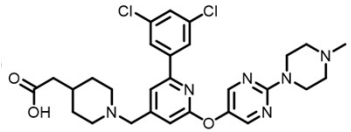

BOS-318

C

	Furin pIC50	PCSK5 pIC50	PCSK6 pIC50	PCSK7 pIC50	Golgi pIC50 (U2OS)
BOS-318	8.8 ± 0.4 (n = 10)	7.6 ± 0.09 (n = 8)	6.7 ± 0.15 (n = 6)	7.4 ± 0.22 (n = 8)	7.7 ± 0.24 (n = 22)
BOS-981	9.3 ± 0.5 (n = 10)	7.5 ± 0.22 (n = 10)	6.9 ± 0.1 (n = 4)	6.9 ± 0.2 (n = 8)	8.3 ± 0.25 (n = 12)
BOS-857	9.4 ± 0.3 (n = 10)	7.6 ± 0.1 (n = 10)	6.7 ± 0.24 (n = 5)	6.9 ± 0.3 (n = 8)	7.6 ± 0.2 (n = 12)
Decanoyl-RVKR-CMK "Furin Inhibitor I"	9.1 ± 0.43 (n = 447)	9.9 ± 0.38 (n = 162)	9.2 ± 0.24 (n = 214)	9.6 ± 0.63 (n = 198)	5.1 ± 0.33 (n = 8)

D

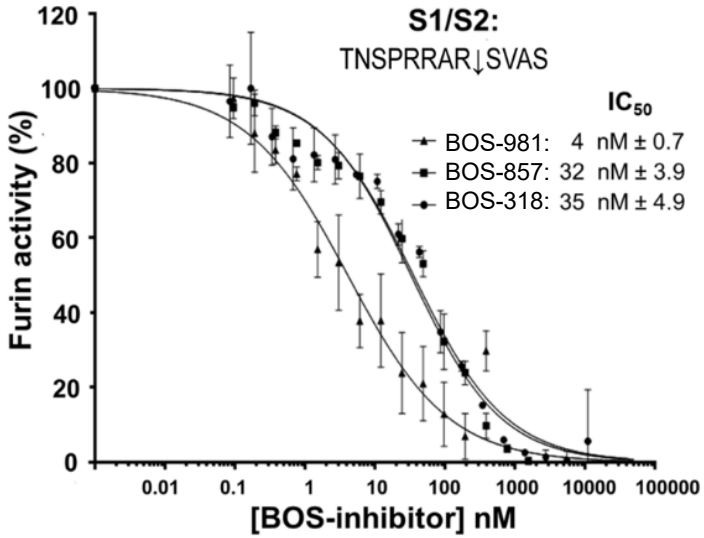

E

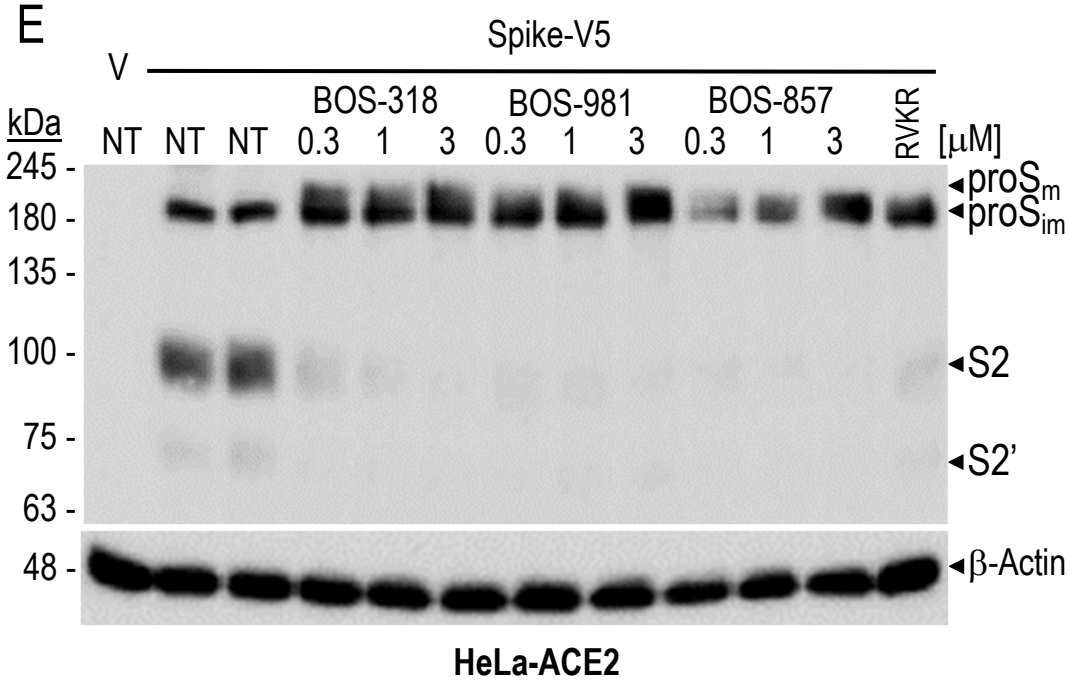

Figure 5

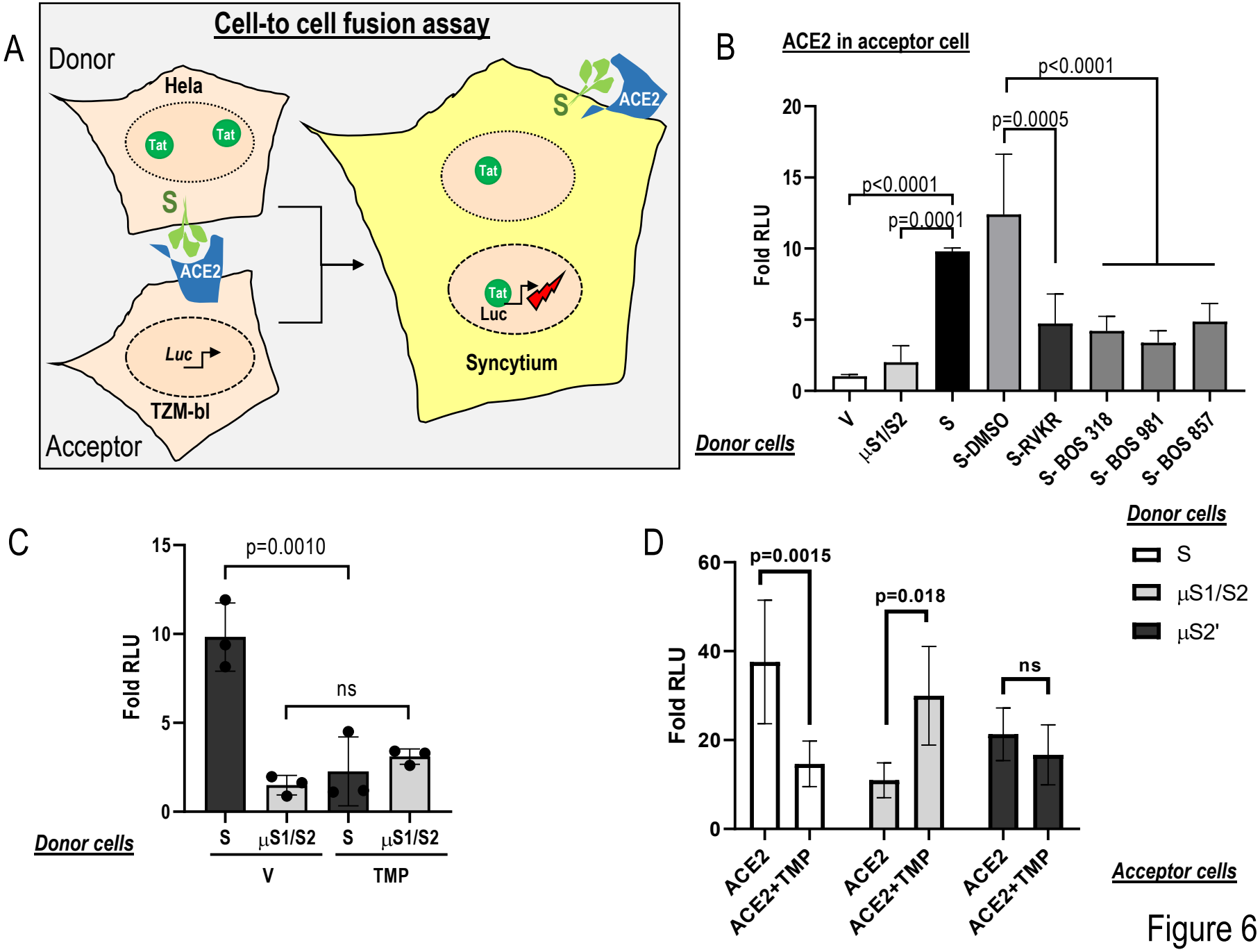
A
Cell-to cell fusion assay
Donor
Hela
Tat
Tat
S
ACE2
Luc
TZM-bl
Acceptor
S
ACE2
Tat
Tat
Luc
Syncytium
B
ACE2 in acceptor cell
Fold RLU
p<0.0001
p=0.0005
p<0.0001
p=0.0001
V
μS1/S2
S
S-DMSO
S-RVKR
S- BOS 318
S- BOS 981
S- BOS 857
Donor cells
C
Fold RLU
p=0.0010
ns
S
μS1/S2
S
μS1/S2
V
TMP
Donor cells
D
Fold RLU
p=0.0015
p=0.018
ns
ACE2
ACE2+TMP
ACE2
ACE2+TMP
ACE2
ACE2+TMP
Acceptor cells
Donor cells
S
μS1/S2
μS2'

Figure 6

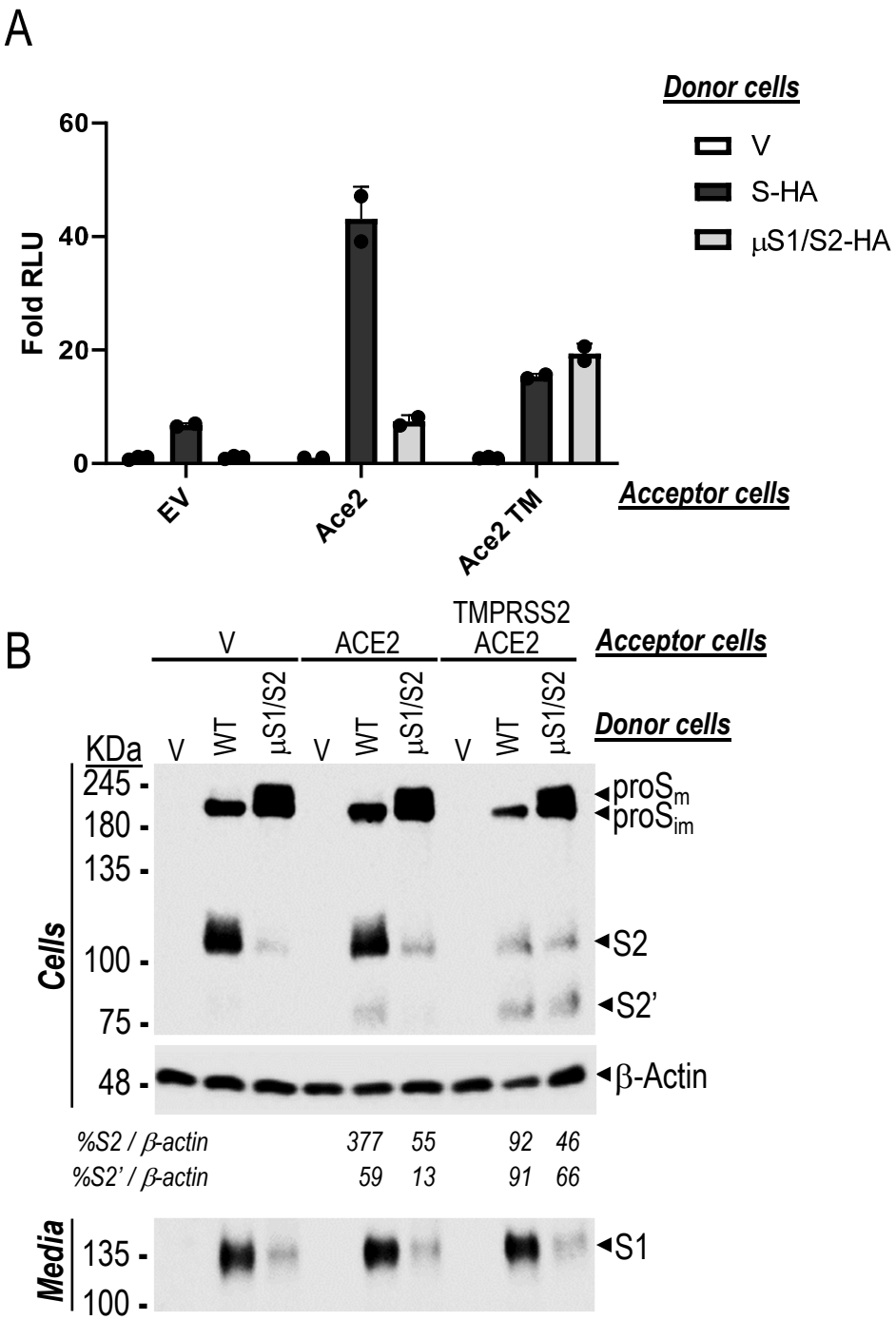
A
Donor cells
V
S-HA
μS1/S2-HA
Fold RLU
60
40
20
0
EV
Ace2
Ace2 TM
Acceptor cells
B
V
ACE2
TMPRSS2
ACE2
Acceptor cells
Donor cells
KDa
V
WT
μS1/S2
V
WT
μS1/S2
V
WT
μS1/S2
245
180
135
100
75
48
Cells
proSm
proSim
S2
S2'
β-Actin
%S2 / β-actin
377
55
92
46
%S2' / β-actin
59
13
91
66
Media
135
100
S1

Figure 7

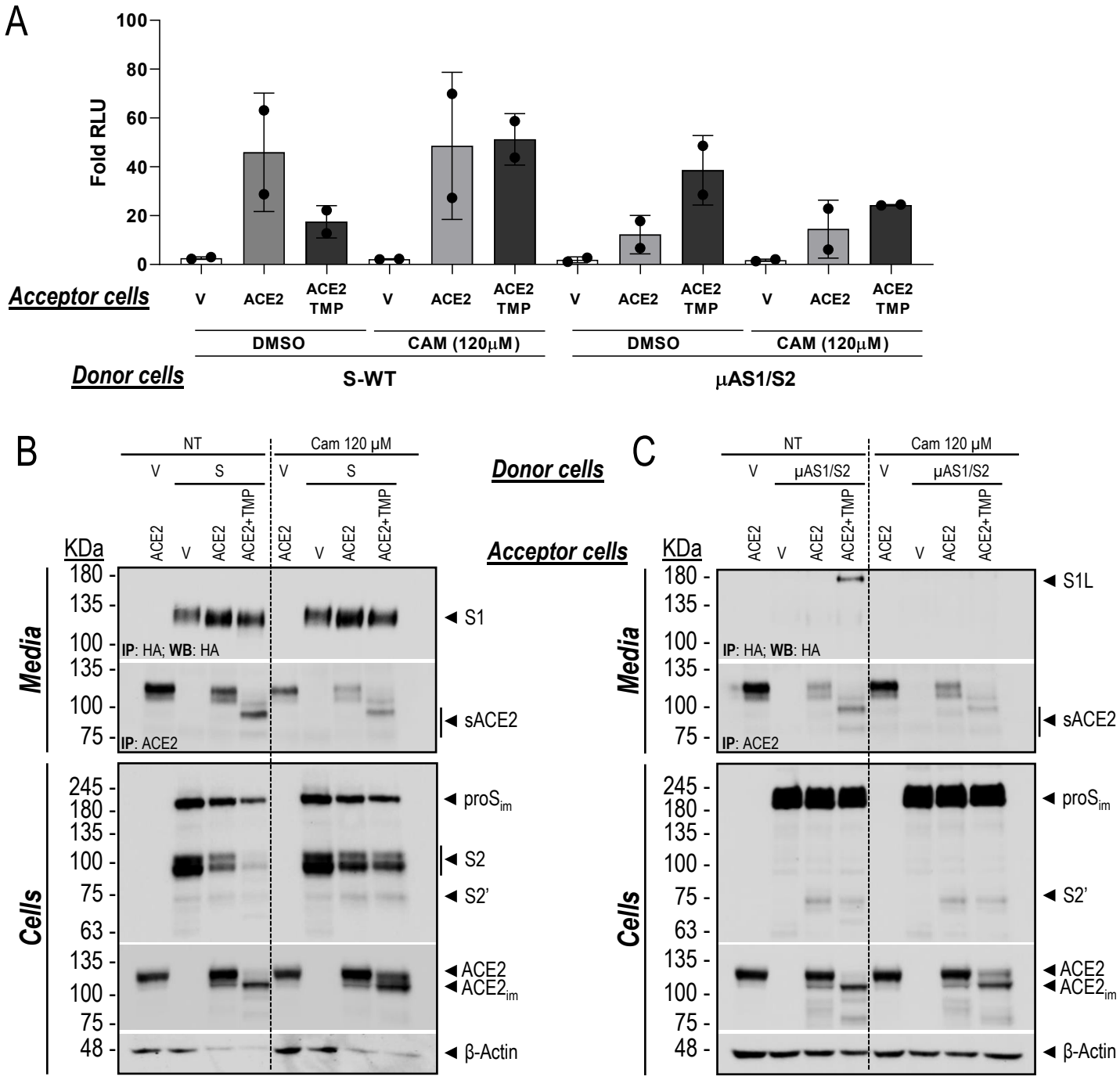
A
Fold RLU
100
80
60
40
20
0
Acceptor cells
V
ACE2
ACE2 TMP
DMSO
CAM (120μM)
Donor cells
S-WT
μAS1/S2
B
NT
Cam 120 μM
S
Donor cells
Acceptor cells
ACE2+TMP
KDa
Media
Cells
IP: HA; WB: HA
IP: ACE2
S1
sACE2
proS$_{im}$
S2
S2'
ACE2
ACE2$_{im}$
β-Actin
C
μAS1/S2
S1L

Figure 8

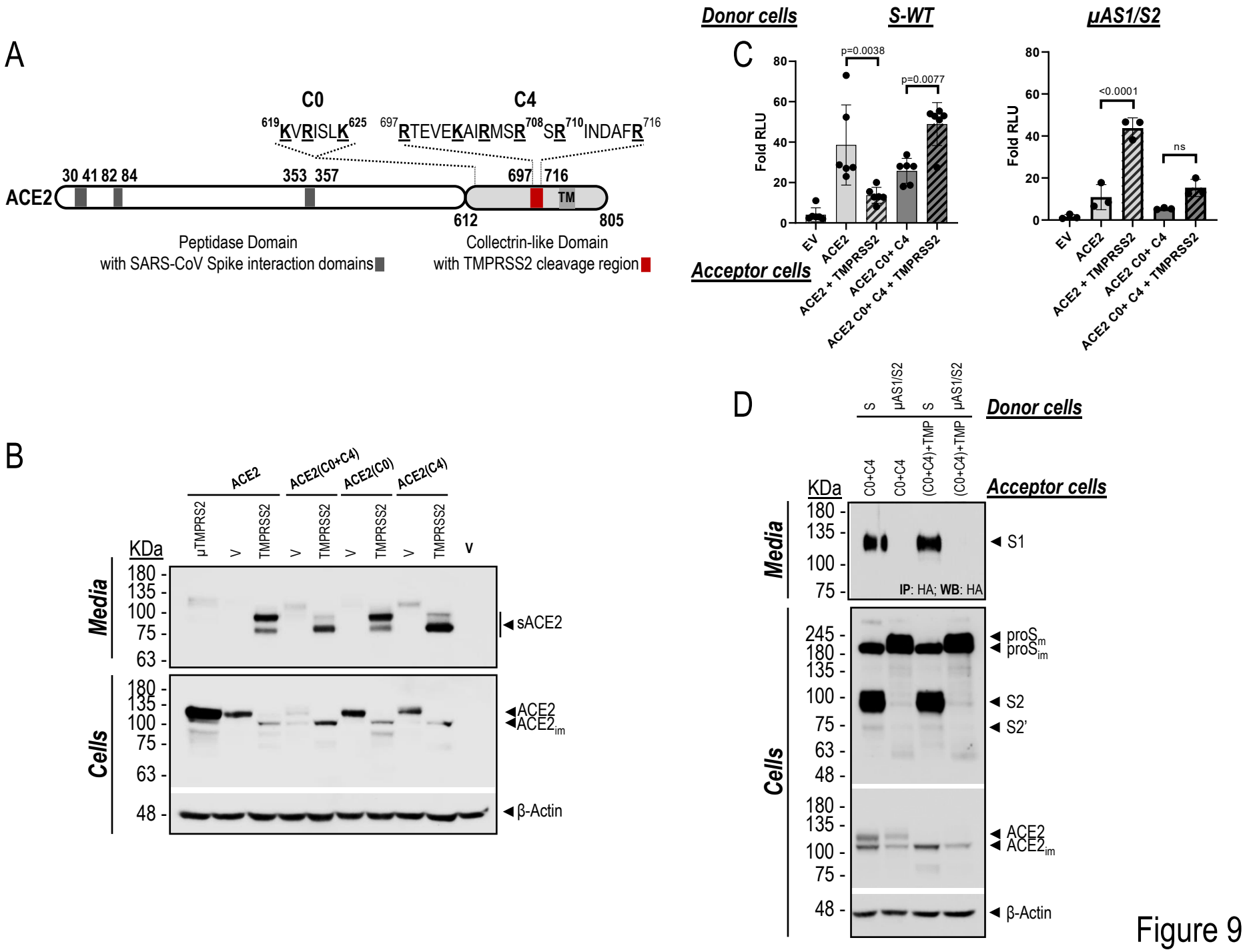
A
C0
C4
619KVRISLK625
697RTEVEKAIRMSR708SR710INDAFR716
ACE2
30 41 82 84
353 357
697 716
TM
612
805
Peptidase Domain
with SARS-CoV Spike interaction domains
Collectrin-like Domain
with TMPRSS2 cleavage region
B
ACE2
ACE2(C0+C4)
ACE2(C0)
ACE2(C4)
μTMPRS2
V
TMPRSS2
KDa
Media
Cells
180
135
100
75
63
48
sACE2
ACE2
ACE2im
β-Actin
C
Donor cells
S-WT
μAS1/S2
Acceptor cells
Fold RLU
p=0.0038
p=0.0077
<0.0001
ns
EV
ACE2
ACE2 + TMPRSS2
ACE2 C0+ C4
ACE2 C0+ C4 + TMPRSS2
D
S
μAS1/S2
C0+C4
(C0+C4)+TMP
Donor cells
Acceptor cells
KDa
Media
Cells
S1
IP: HA; WB: HA
245
proSm
proSim
S2
S2'
ACE2
ACE2im
β-Actin

Figure 9

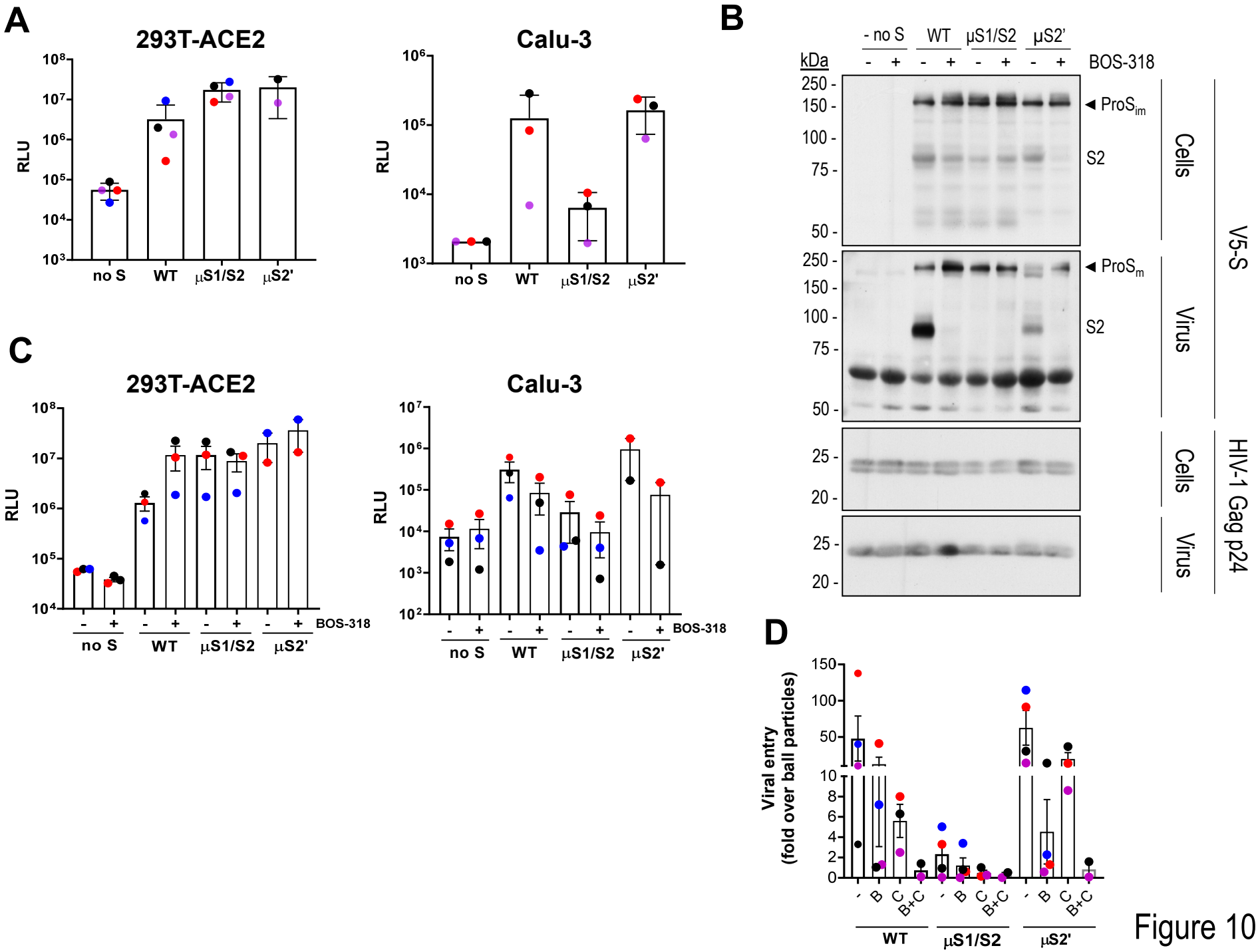
A
293T-ACE2
Calu-3
RLU
no S
WT
μS1/S2
μS2'
B
- no S
WT
μS1/S2
μS2'
kDa
BOS-318
ProSim
ProSm
S2
Cells
Virus
V5-S
HIV-1 Gag p24
C
BOS-318
D
Viral entry
(fold over ball particles)
B
C
B+C

Figure 10

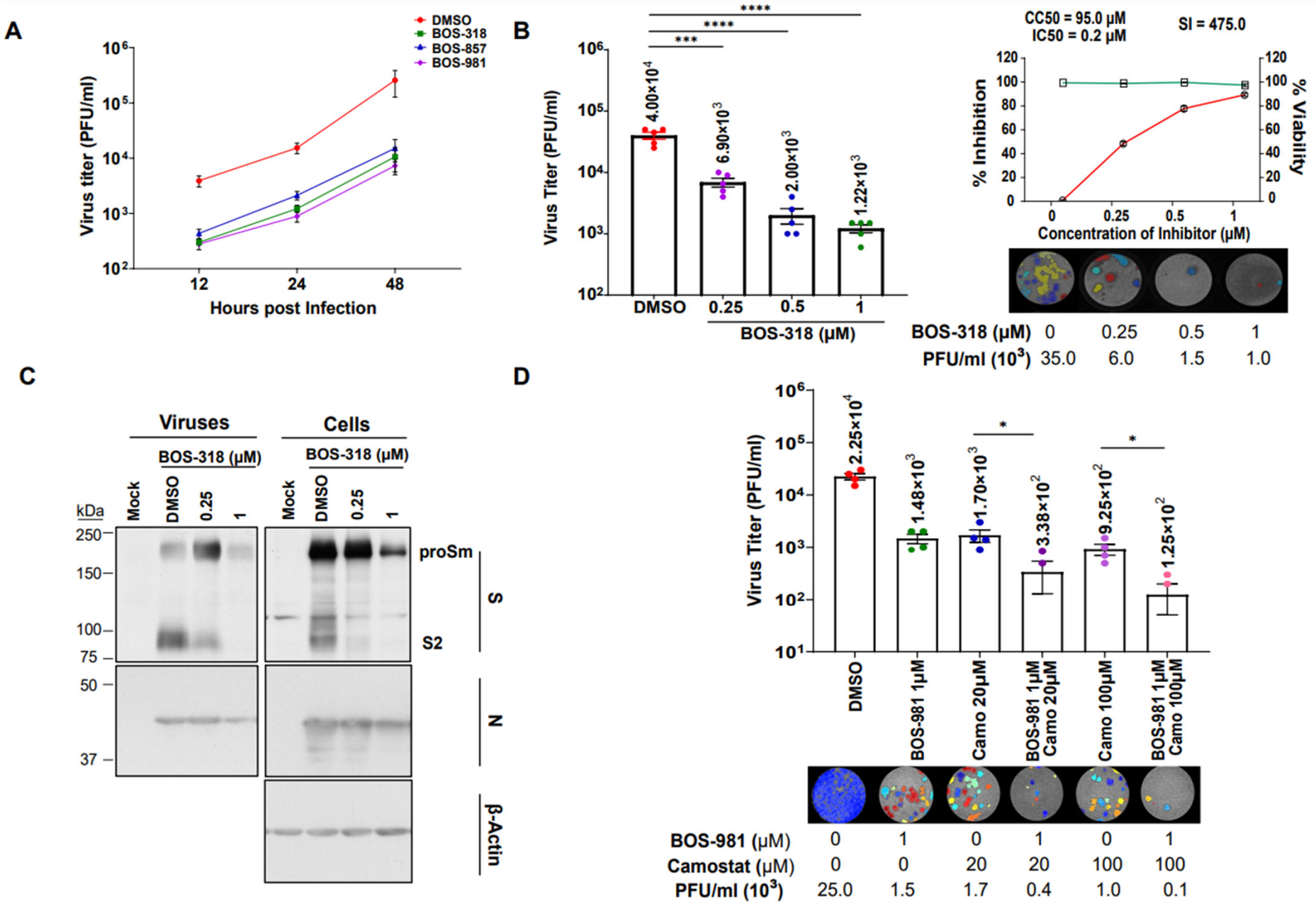
A
DMSO
BOS-318
BOS-857
BOS-981
Virus titer (PFU/ml)
Hours post Infection
B
Virus Titer (PFU/ml)
4.00×10^4
6.90×10^3
2.00×10^3
1.22×10^3
DMSO
0.25
0.5
1
BOS-318 (μM)
CC50 = 95.0 μM
IC50 = 0.2 μM
SI = 475.0
% Inhibition
% Viability
Concentration of Inhibitor (μM)
BOS-318 (μM) 0 0.25 0.5 1
PFU/ml (10^3) 35.0 6.0 1.5 1.0
C
Viruses
Cells
BOS-318 (μM)
Mock
DMSO
0.25
1
kDa
proSm
S2
S
N
β-Actin
D
Virus Titer (PFU/ml)
2.25×10^4
1.48×10^3
1.70×10^3
3.38×10^2
9.25×10^2
1.25×10^2
DMSO
BOS-981 1μM
Camo 20μM
BOS-981 1μM Camo 20μM
Camo 100μM
BOS-981 1μM Camo 100μM
BOS-981 (μM) 0 1 0 1 0 1
Camostat (μM) 0 0 20 20 100 100
PFU/ml (10^3) 25.0 1.5 1.7 0.4 1.0 0.1

Figure 11

Role of Furin & TMPRSS2 in SARS-CoV-2 infections and tropism

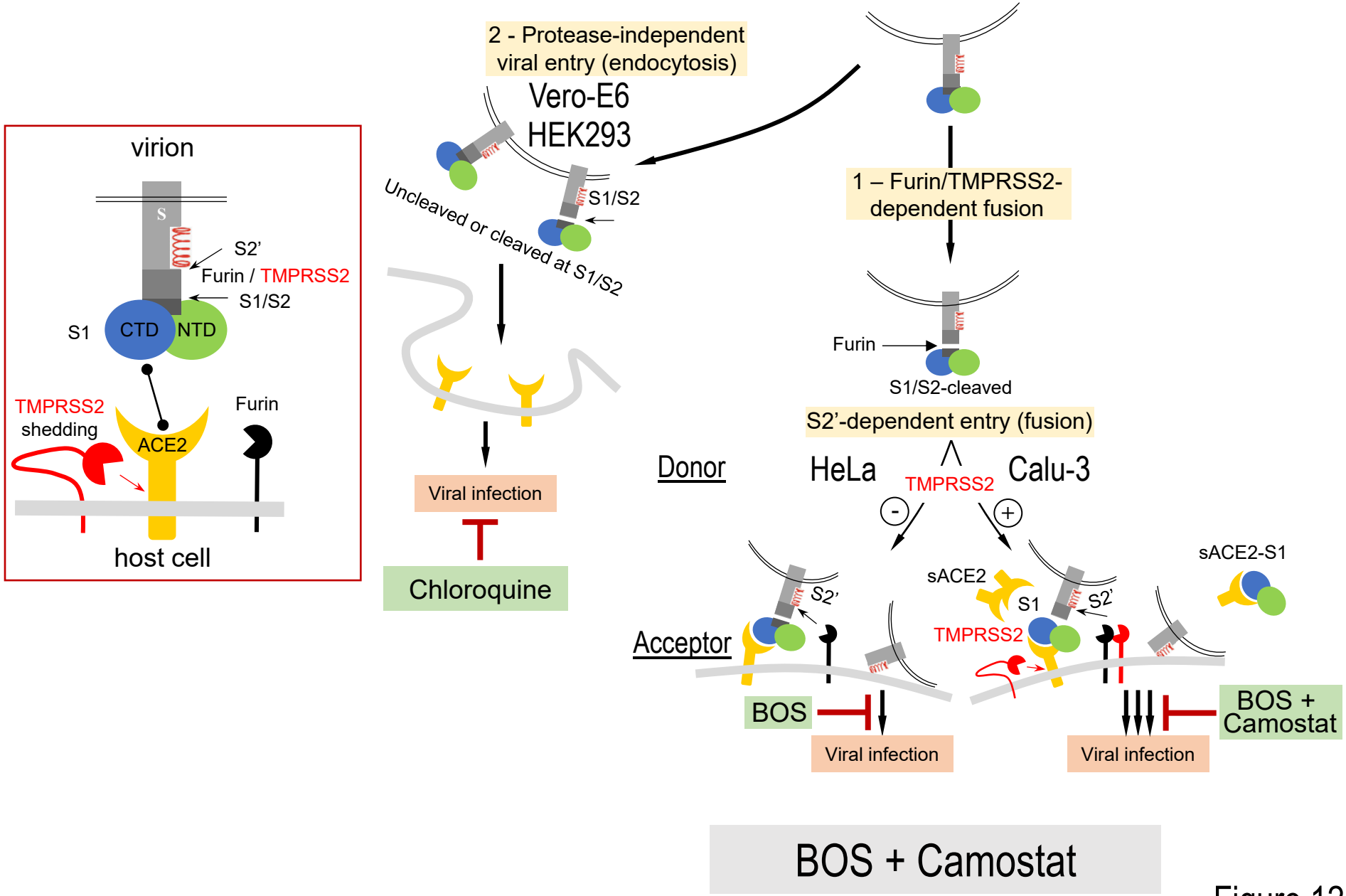

Figure 12